Acta Universitatis Sapientiae

Electrical and Mechanical Engineering
Volume 12, 2020

Contents

A New Model of Dynamic Logic Circuit with NMOS based Keeper

Riazul ISLAM[1] and Satyendra N. BISWAS[2]*

[1]Department of Electrical and Electronic Engineering, International Islamic University Chittagong, Chittagong, Bangladesh. e-mail: r.islam@iiuc.ac.bd/ iriazul74@gmail.com
[2]Department of Electrical and Electronic Engineering, Ahsanullah University of Science and Technology, Dhaka, Bangladesh, e-mail: sbiswas@linuxmail.org / sbiswas.eee@auct.edu
*corresponding author

Abstract: Dynamic logic circuits are widely popular due to a smaller number of transistors and consume less area. But the time to switch between logics is higher due to higher contention value. A new model of the logic using nMOS based keeper circuit is proposed and the performance is evaluated using Cadence tools. Comparative results demonstrate the suitability and competency of the proposed circuit.

Keywords: Keeper circuit, dynamic node, nMOS based keeper.

1. Introduction

High speed and low power logic circuit designs are more significant in VLSI design [1], [2]. Dynamic logic circuit needs to have almost half the number of transistors compared to traditional logic circuits. It saves better power than traditional logic circuits. Dynamic logic consists of a precharge device, a pull-down network, pMOS keeper and a footer device. A clock signal is used to control and operate domino logic.

Basically, dynamic logic circuits operate in two phases, these are precharge phase and evaluation phase. When clock is high it is called evaluation phase and when the clock is low it's called precharge phase. However, the main drawback of domino logic circuit is that it is not always connected to V_{DD}. A keeper device has been used to compensate that. When all inputs are high then the stored voltage at the dynamic node should be removed through the PDN (Pull Down Network). That produces some time delay between the conduction of keeper transistor and pull down network. Also, that causes increasing time delay, power consumption and noise sensitivity [3]. To minimize these

drawbacks, we need to design a new keeper architecture which gives better performance.

A new architecture is proposed in this research for better performance in terms of power consumption and noise margin of dynamic logic. The power consumption of logic circuits is calculated [3] by

$$P_{avg/gate} = P_{switching} + P_{short-circuit} + P_{leakage} \tag{1}$$

Here, the power consumption of the logic gates by charging/ discharging of circuit capacitances is denoted by $P_{switching}$. Short circuit current flowing from V_{DD} to ground is denoted by $P_{short-circuit}$ during output voltage alterations. Leakage power ($P_{leakage}$) is dramatically changed by scaling down the technology and enhanced by temperature, which is very significant for the reduction of leakage power of dynamic logic circuits.

The proposed nMOS based resistive keeper circuit is employed for simulating 4, 8, 16, 32-input OR gates, by using Cadence Virtuoso tool. The obtained results demonstrated the enhanced noise tolerance, reduced power dissipation and time delay as compared to conventional logic circuits.

Recently proposed [4]-[15] dynamic logic circuits are presented in *Section 2*. *Section 3* describes the proposed resistive keeper circuit. *Section 4* presents the proposed model with different combinations in the pull down network. *Section 5* depicts the analysis and simulation results of the proposed technique. Finally, the paper concludes in *Section 6*.

2. Existing Works

The easiest way to improve the noise tolerance of dynamic logic circuits is to provide a weak keeper device to maintain the required amount of charge in the dynamic node. The gate of a keeper transistor is connected to the ground as used in some [4] domino logic, where the keeper device is always ON. But this type of design consumes more power as DC power continuously follows through that keeper transistor. To compensate that problem, a feedback keeper transistor is designed [4]. This model controls the keeper device during the evaluation phase as shown in *Fig. 1*. The main purpose of the keeper device is to reduce the contention time in the evaluation phase, when the pull down network is ON. So, a keeper circuit should be designed to reduce the leakage current through pull down network for wide fan-in gates.

Several research groups [4] - [15] have proposed different versions of the strong keeper circuit model, which minimize the contention problem. Those models make the keeper device inactive during the switching time and are better for noise tolerance in the dynamic logic circuits. However, these models are

unable to reduce the leakage current to a tolerable level. For that reason, the dynamic node cannot protect itself during PDN switching.
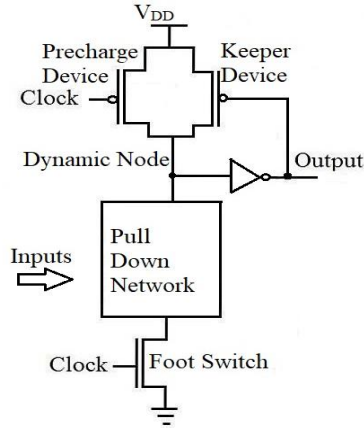
Figure 1: Traditional domino logic
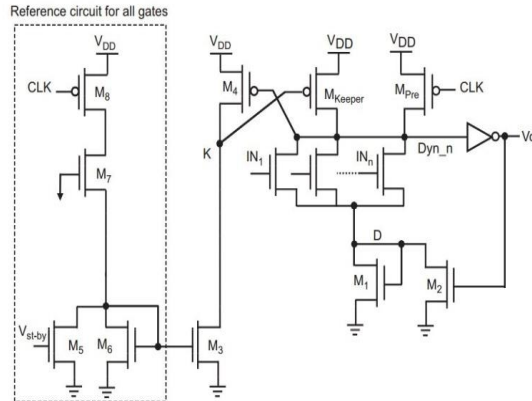
Figure 2: Controlled keeper by current comparison domino circuit (CKCCD) [5]

Ali et al. [5] designed a reference circuit to sense the PDN leakage current. Depending of the amount of leakage current of dynamic node, a mirror current is generated, which is responsible to control the gate of the keeper device. This design contains a large number of transistors as compared with other circuits as shown in *Fig.* 2.

Conditional keeper domino logic is one of the popular domino logic which is presented by A. Alvandpour et al. [6]. Two keeper transistors (weak and strong)

are employed in this technique. These extra transistors increase the cell area and can improve the noise immunity, although, the circuit consumes significant power.

In high speed domino circuits, several inverters are used to control the current flow through the pMOS and nMOS network at the beginning of the evaluation phase [7]. This technique has induced the need for a larger pMOS keeper transistor. In this model, current flow of the pMOS and nMOS keeper transistor network is controlled by two-time delay inverters. However, their circuit was unable to provide sufficient protection against the internal noise at the dynamic node.

Dadgour and Banerjee et. al. [8] presented a new keeper architecture where they reduced the contention current and power consumption to improve the performance of dynamic logic. There are several components in their model such as: two keeper devices, variation coupled keeper (VCK) etc. But their model shows lower noise margin because of leakage current affected the dynamic node.

Current Comparison Domino (CCD) is another technique to compensate the leakage current of domino logic [9]. This technique is used to control a pull-up network instead of a pull down network. A reference circuit is used to provide the proper output by comparing the current between reference circuit and pull up network. This technique is efficient but it needs more overhead area compared to conventional domino logic circuits.

Diode footed domino (DFD) circuits [10] produce better results in terms of noise immunity and leakage current. In this design, an nMOS is connected with the PDN and called as diode footer transistor. This footer transistor reduces the leakage current, which is generated due to stacking effect. However, more area overhead and power consumption are the significant drawbacks of this presented model.

Asyaei et al. [11] designed a sense amplifier to generate proper voltage on the output node. There are two stages of their model: one is pull down network designed with variable inputs of logic gate and the other is the sense amplifier which sensed the voltage difference between the point A and B as shown in *Fig. 3*. Basically, the dynamic node of this circuit is controlled by these two points. It reduces the leakage current due to the stacking effect whereas needs a larger number of transistors and consumes more power.

A new model with an external circuitry is proposed by Lih et al. [12]. The additional circuit controls the conductance of the keeper transistor by generating the replicate leakage current of the PDN (pull down network) as shown in *Fig. 4*. The keeper circuit is controlled by dynamic node leakage current, which is also generated by an external circuit. This model also used two keeper transistors and extra circuits which increased the overhead area.
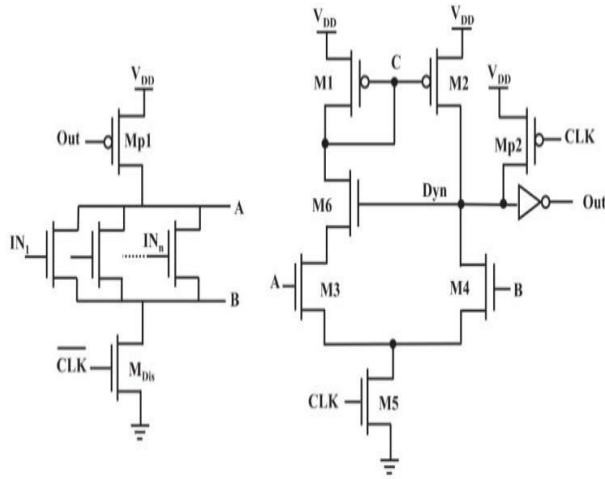
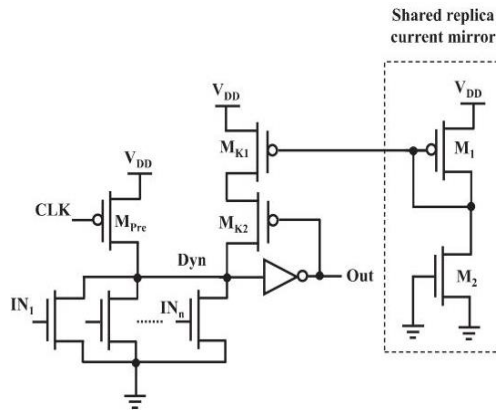*Figure 3*: VCD circuit [11]

Figure 4: LCR keeper Circuit [12]

However, in this research, two nMOS based resistive keeper models are presented. The circuits control the gate to source voltage of keeper device with differential waveforms to enhance the noise tolerance of the dynamic logic circuits and lower leakage power consumption.

3. Proposed Design

The proposed circuit controls the gate of the keeper device with differential waveforms. This gate is designed by using two nMOS transistors (T_{R1} and T_{R2}). These transistors are connected in parallel but are not operated at the same time. Both nMOS transistors are designed with different length and width. When any small amount of leakage current passes through PDN or any path, it tends to be grounded. At that time, T_{R1} operates and controls the gate of keeper device to maintain the proper state of the dynamic node. This happens according to $I_{TR1}= I_X-I_{leakage}$, $I_{Tp}= I_{DD}- I_{TR1}$, whereas I_X is dynamic node current and $I_{leakage}$ is the leakage current. The inverter is operated to supply the proper voltage on the gate of the keeper device. Any current flowing in the dynamic node while the pull down network is in logical OFF mode is considered as leakage current ($I_{leakage}$).

Transistor T_{R2} is connected in parallel with T_{R1}. When the pull-down network conducts T_{R2} operates and controls the gate of the keeper device. Besides, when all inputs of the pull down network become low, a small amount of leakage current is flowing. For that reason, a footer switch is added to reduce the leakage power.

This leakage current also decreases the noise tolerance and increases the robustness of the circuit. As we know, a parasitic capacitance is induced in the dynamic node at the beginning of the evaluation phase which provides more time delay in the dynamic logic. The feedback of the nMOS based resistive circuit can control the gate of the keeper device by applying different waveforms. Conventional dynamic logic circuits produce contention between pull down network and keeper device. That increases the leakage current, time delay and power consumption. But the proposed work decreases this problem between the PDN and keeper device contention evaluation phase.

Also, T_w can be keeping the contribution of sub threshold leakage reduction due to the stacking effect in the evaluation phase [13]. So, the leakage power of this circuit is reduced by applying these techniques. In the dynamic logic circuit, the size of the keeper device can be minimal because the leakage current of the pull-down network is very low. Also, more than 32 input OR gates give better noise immunity if the keeper sizes are increased. However, the proposed circuit reduces the ratio of W_k / W_p.
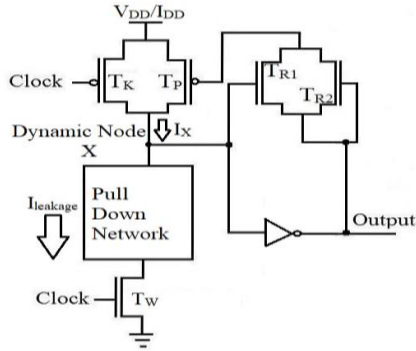
Figure 5: Proposed dynamic logic
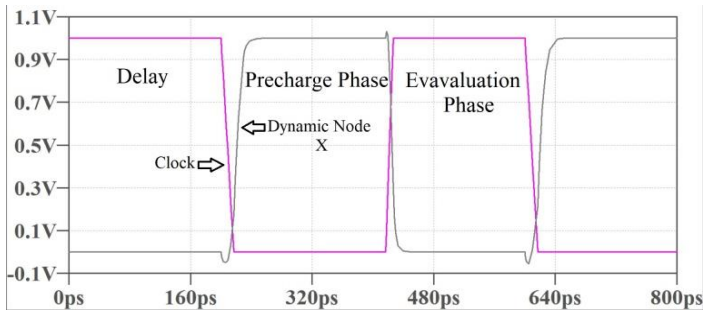
Figure 6: Waveshape of clock versus dynamic node voltage

3.1 Precharge Phase

As shown in *Fig. 5*, when the clock is low, precharge transistor T_k turns ON and footer transistor T_w turns OFF. At that time the dynamic node charges to V_{DD} and the output logic is '0'. At this time T_{R2} is OFF and T_{R1} is in ON state. The gate-source voltage of the keeper device is controlled by the feedback of resistive gate. In this phase, leakage current is reduced due to stacking effect.

3.2 Evaluation Phase

In this phase, the precharge device turns OFF and footer switch (T_W) turns ON.

A. Inequality:

If at least two inputs differ in case of the OR gate, one leg of the pull down network conducts to discharge the dynamic node via T_W. At this time, transistor T_{R1} turns OFF and T_{R2} is controlled by the inverter output voltage. Basically,

the keeper circuit works as a gate for the keeper transistor T_p. Operation of T_p is dependent on differential waveforms of the proposed keeper circuit. The feedback of nMOS based keeper circuit maintains sufficient voltage to control the logic value in the dynamic node, X. Keeper circuit is always controlled by the dynamic node voltage and at least one nMOS is ON in every logic combination. The dynamic node wave shape is shown in *Fig. 6.*

B. Equality:

When all inputs are high in the evaluation phase, foot switch (T_W) is ON which makes a discharging path for the dynamic node and T_{R2} produces the inverter voltage to control the keeper device as shown in *Fig. 7.* A contention time occurs between the nMOS network and keeper device because the keeper device is ON until the inverter voltage goes to minimum to turn off the keeper device in conventional dynamic logic. However, this problem is minimized with this work.

Table 1: Size of transistors for different inputs   of OR gates

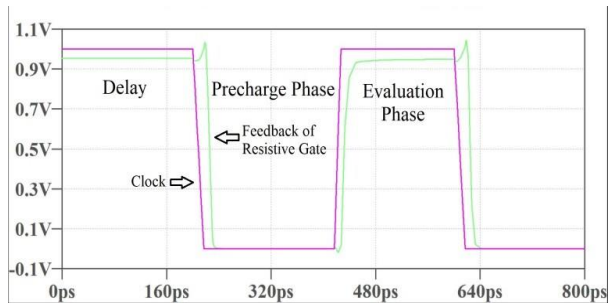| Wide Fan	4	8	16	32
$(W/L)_{TK}$	3Lmin/ 1Lmin	3Lmin/ 1Lmin	3Lmin/ 1Lmin	3Lmin/ 1Lmin
W_{TW}	8Lmin	8Lmin	8Lmin	11Lmin
$(W/L)_{TR1}$	3Lmin/ 5Lmin	3Lmin/ 5Lmin	3Lmin/ 6Lmin	3Lmin/ 6Lmin
$(W/L)_{TR2}$	3Lmin/ 6Lmin	3Lmin/ 6Lmin	3Lmin/ 6Lmin	3Lmin/ 6Lmin
$(Wp)_{Inverter}$	6Lmin	6Lmin	6Lmin	6Lmin
$(Wn)_{Inverter}$	6Lmin	6Lmin	8Lmin	8Lmin
$(W/L)_{TP}$	3Lmin/ 5Lmin	3Lmin/ 5Lmin	3Lmin/ 5Lmin	3Lmin/ 6Lmin

Figure 7: Clock versus feedback resistive gate

4. Sizing of Transistors

In this research, several works have been studied to be compared with the proposed circuit such as: high-speed domino circuit (HSD), the controlled keeper by current comparison technique (CKCCD) (*Fig. 2*), voltage comparison-based domino logic circuit (VCD) (*Fig. 3*) and the proposed dynamic logic circuit. In HSD circuit, different widths to length ratios are used to get the best performance. In conditional keeper domino logic (CKD), length is used as 2Lmin.

We used OR4, OR8, OR16, OR32 gates and time delay are taken as 170ps, 190ps, 200ps and 210ps. It is to be noted that the size of the transistors are adjusted to obtain the best result as shown in *Table 1*. Weak and strong keepers are used and varied to get the desired result. An inverter is used, which has the width to length ratio of 2.

In the proposed technique, T_P is the keeper transistor which compensates the leakage current and increases the robustness of the circuit. As we know, upsizing the keeper transistor increases the noise immunity but also increases the power consumption. So, a minimum size is required to increase the noise tolerance and size of keeper transistor should be lowered to avoid the flow of leakage current. Transistor T_w is inserted to avoid the unwanted discharging path in the dynamic node due to leakage current. Also, the length of this transistor is increased to reduce the leakage current flowing and power consumption. In the proposed resistive gate circuit, the size of two transistors must be asymmetric to generate the proper voltage to control the gate of keeper device. The length of the transistor is upsized followed by different OR gates. *Table 1*. shows the size of transistors with different inputs of OR gate. In the pull down network, all nMOS transistors are of the same width where, 22 nm transistors are used and the width is set to minimum W= 3Lmin.
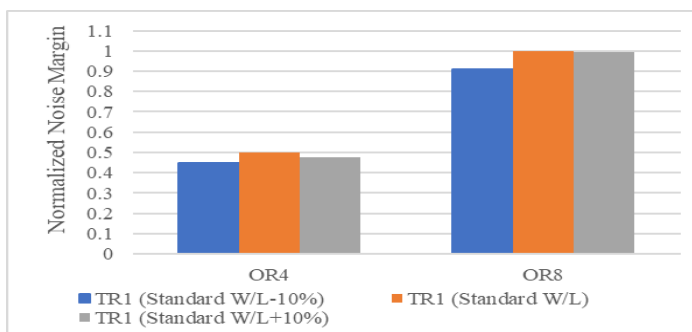

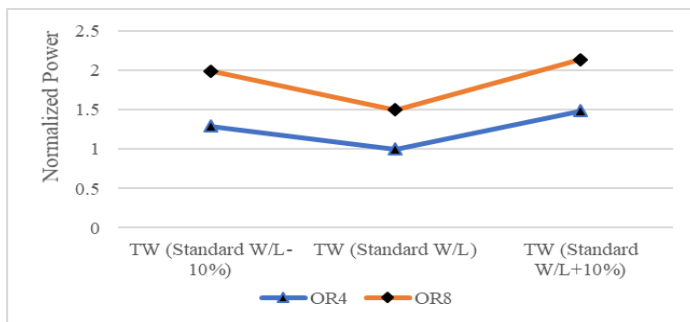*Figure 8*: Noise tolerances for various W/L ratios of transistor TR1

Figure 9: Power consumption for various W/L ratios of transistor Tw

The W/L ratio of T_{R1} is set from 3L/5L to 3L/6L for wide fan-in OR gate in order to get better noise immunity. By changing that ratio from "standard W/L-10%" to "standard W/L+10%", obtained noise tolerances are shown in *Fig. 8*. So, these standard ratios are chosen to operate the resistive gate. Selected standard W/L ratio of T_w for low power consumption is shown in *Fig. 9*. Basically, T_w can contribute to decrease the leakage current flowing at evaluation phase. So that, proper sizing of this type of transistor provides better noise tolerance and low power consumption.

5. Simulation Results

Simulation experiments were carried out using the LTspice simulation tool with 22nm PTM technology model [14]. Generated wave shape and data are taken from wide fan-in (4, 8, 16, 32 input) OR gates and the results are compared with several previous works. It is clearly noticed that the proposed model provides better noise tolerance. These data are obtained by setting (W/L) T_K = (3L/ 1L) min, (W/ L) T_p= (3L/ 5L) min and W_p= 6L min, W_n= 6L min for output inverter.

5.1   Noise Margin Analysis

Noise margin is defined as the rate of stability of a circuit and noise tolerance of stored data at the dynamic node. Leakage measurement method can explain the Unity Noise Gain (UNG). Where different types of identical noise pulses are applied on inputs and amplitudes of output noise are analyzed. Basically, UNG is used for making the comparison between leakage and noise robustness of domino logic circuit and it can be estimated [15] by using the following equation:

$$UNG = \{V_{in}; V_{noise} = V_{out}\} \tag{2}$$

In the proposed dynamic logic circuit, when the circuit is affected by noise, the keeper device will not work perfectly because the generated noise could modify the gate voltage of the keeper device. For that reason, two-external voltages are applied on the keeper device with opposite polarities. The gate of the keeper device is connected with an external noise source and the drain or dynamic node is connected with another external noise source. A dynamic circuit is considered to be good when the designed circuit can tolerate more noises without data distortion.

It is noticeable that the noise margin (NM) is decreased with the number of inputs as shown in *Table 2*. So, the fact is that the number of inputs is a significant factor. The noise tolerance values of the proposed model give better normalized data.

Table 2: Normalized noise margin (NM) and power (NP) of different OR gates

Different	Fan-in 4		Fan-in 8		Fan-in 16		Fan-in 32	
Models	NM	NP	NM	NP	NM	NP	NM	NP
HSD [7]	0.37	2.03	0.33	1.94	0.3	1.68	0.27	1.81
VCD [8]	0.36	2.4	0.32	2.2	0.28	1.9	0.26	1.8
CCD [9]	0.36	1.32	0.34	1.3	0.32	1.31	0.29	1.24
Proposed	**0.395**	**1**	**0.379**	**1**	**0.361**	**1**	**0.340**	**1**

5.2 Power Analysis

Table 2 shows the comparison of power consumption. This data is normalized with respect to the proposed circuit. All data was taken using 22nm Predictive technology model. The proposed circuit shows a significantly lower amount of power consumption as compared with the high-speed domino (HSD) logic and Voltage control domino circuit (VCD). In the collection of high speed domino (HSD) logic data, a change of the size of the keeper device is required.

In the current comparison domino circuit, several models are used to control the gate of the pMOS keeper device which increases the time delay. However, the proposed circuit reduces the time delay using nMOS based resistive gate.

The normalized power (NP), delay (ND) and noise margin (NNM) are shown in *Fig. 10*. The figure shows, that a better decrement of power and delay is achieved in the 22nm model while the noise margin gets better value in the 45nm model. *Table 3* presents the standby power of the proposed circuit showing lower power consumption in OR32 and OR16 and also shows higher power consumption rate than the model proposed in [21] for 8 inputs OR gates.

Table 3: Comparison of standby power consumption in μW

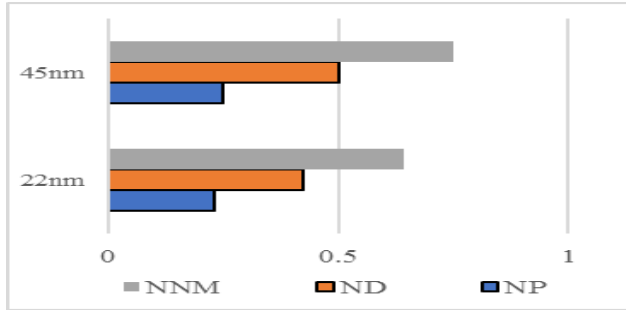| Models	CCD [9]	CKCCD [10]	Proposed
OR8	1.5	1.6	*1.7*
OR16	1.8	1.6	*1.5*
OR32	1.7	1.6	*1.4*

Figure 10: Normalized data for several aspects of measurement

5.3 Area Calculation

The layout of the proposed model is designed using Cadence Virtuoso tool and checked by DRC)Design Rule Checker(and LVS)Layout versus Schematic). The proposed techniques have been compared with several conventional methods. The proposed model required only 39 transistors for designing the 32 inputs OR gate while the other techniques need more transistors as shown in *Table 4*. Also, area overhead data obtained by using 90 nm technology is shown. The proposed circuit designed at 90nm technology requires an area of 8.1055 μm^2, whereas the same circuit designed at 45nm technology (*Fig. 11.*) requires only 2.2385 μm^2.

Table 4: Comparison of the number of transistors with other works for 32 inputs of OR gate and area overhead using Cadence Virtuoso tool for 2 inputs of OR gate using 90 nm model.

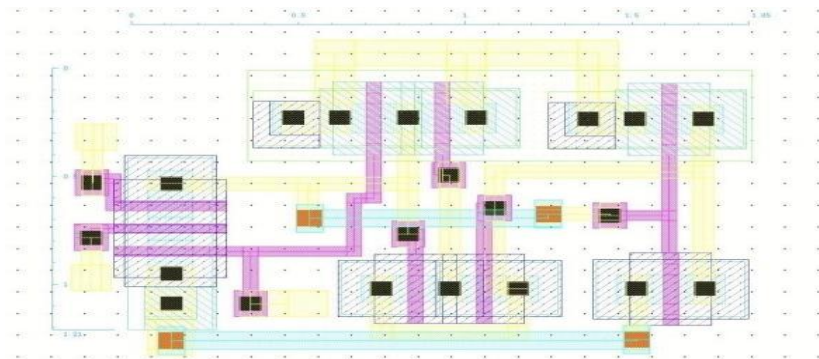| Several Works	Number of Transistor	Area
CKCCD [10]	42	18.250 μm^2
LCR [12]	37	10.1875 μm^2
CCD [9]	41	14.9062 μm^2
Proposed	*39*	*8.1055 μm^2*

Figure 11: Layout of the proposed circuit using 45nm model

6. Conclusion

A keeper circuit consisting of only two nMOS transistors has been designed for a dynamic logic circuit. The proposed circuit acts like a resistive gate for the keeper transistor. As this circuit is connected in series with the gate of the keeper transistor, so the current through the resistive circuit is less and makes the keeper weaker at the start of the operation. The contention time is reduced as needed. Extensive simulation results demonstrate that the proposed circuit consumes less power and provides better noise margin as compared with several conventional models.

References

[1]   Anders, M., Mathew, S., Bloechel, B., Thomson, S., Krishnamurthy, R., Soumyanath, K., and Borkar, S. Y., "A 6.5 GHz 130 nm single-ended dynamic ALU and instruction scheduler loop", *in Proc. ISSCC Dig. Tech..*, pp. 410–411, 2002.

[2]   Kuroda, T., Fujita, T., Mita, S., and Nagamatsu, T., "A 0.9 V 150 MHz 10 mW 4 mm/sup 2/2-D discrete cosine transform core processor with variable-threshold-voltage scheme", *IEEE Solid-State Circuits Conference. Digest of Technical. 42nd ISSCC*, 1996, pp. 166-167.

[3]   Rabaey, J. M., Chandrakasan, A. P., and Nikolic, B., "Digital integrated circuits. Vol. 2." Englewood Cliffs: Prentice Hall, 2002.

[4]   Alvandpour, A., Krishnamurthy, R., K. Soumyanath, and Borkar, S. Y., "A conditional keeper technique for sub-0.13/spl mu/ wide dynamic gates", in *Proc. Int. Symp on VLSI Circuits. Digest of Technical*, 2001, pp. 29–30.

[5]   Peiravi, A., and Asyaei, M., "Robust low leakage-controlled keeper by current-comparison domino for wide fan-in gates", *Integration, the VLSI journal*, vol. 45, no. 1, pp. 22-32, Jan. 2012.

[6]   Alvandpour, A., Krishnamurthy, R. K., Soumyanath, K., Borkar, S. Y., "A sub-130-nm conditional-keeper technique", *IEEE Journal of Solid-State Circuits*, vol. 37, no. 5, pp. 633–638, May. 2002.

[7]   Anis, M. H., Allam, M. W., Elmasry, M. I., "Energy-efficient noise-tolerant dynamic styles for scaled-down CMOS and MTCMOS technologies", *IEEE Transactions on Very Large Scale Integration (VLSI) Systems*, vol.10, no. 2, pp. 71–78, Aug 2002.

[8]   Dadgour, H. F., and Banerjee, K., "A novel variation-tolerant keeper architecture for high-performance low-power wide fan-in dynamic OR gates", *IEEE Transactions on Very Large Scale Integration (VLSI) Systems*, vol. 18, no.11, pp. 1567-1577, Oct. 2009.

[9]   Peiravi, A., and Asyaei, M., "Current-comparison-based domino: New low-leakage high-speed domino circuit for wide fan-in gates", *IEEE transactions on Very Large-Scale Integration (VLSI) Systems*, vol. 21, no. 5, pp. 934-943, May. 2013.

[10] Mahmoodi-Meimand, H., and Roy, K., "A leakage-tolerant high fan-in dynamic circuit design style", in *Proc. of the IEEE International Systems-on-Chip (SOC) Conference*, 2003, pp. 117–120.

[11] Asyaei, M., "A new leakage-tolerant domino circuit using voltage-comparison for wide fan-in gates in deep sub-micron technology", *I*ntegration*, the VLSI journal*, vol. 51, pp. 61-71, Sept. 2015.

[12] Lih, Y., Tzartzanis, N., and Walker, W. W., "A leakage current replica keeper for dynamic circuits", *IEEE Journal of Solid-State Circuits*, vol. 42, no. 1, pp. 48-55, Jan. 2007.

[13] Kim, C. H., Roy, K., Hsu, S., Krishnamurthy, R., and Borkar, S. Y., "A process variation compensating technique with an on-die leakage current sensor for nanometer scale dynamic circuits", *IEEE Transactions on Very Large-Scale Integration (VLSI) Systems*, vol. 14, no. 6, pp. 646–649, July. 2006.

[14] Predictive Technology Model (PTM), The 22-nm High Performance V2.1 Technology of PTM Model. Available online: /http://ptm.asu.edu/model card/HP/22 nm_HP.pm.> 2008.

[15] Ding, Li., and Mazumder, P., "On circuit techniques to improve noise immunity of CMOS dynamic logic", *IEEE Transactions on Very Large-Scale Integration (VLSI) Systems*, vol. 12, no. 9, pp. 910-925, Sept. 2004.

[16] Islam, R., and Biswas, S. N., "A low power dynamic logic with nMOS based resistive keeper circuit", IEEE *International Conference on Innovative Mechanisms for Industry Applications (ICIMIA)*, 2017, pp. 181-185.

Generation of PWM Based on Simple Relay Feedback Systems

Abdelouahab ZAATRI[1], Ridha KELAIAIA[2]

[1] Laboratory of Applications of Advanced Technology (LATA), University of Constantine1, Constantine, Algeria, e-mail: azaatri@yahoo.com
[2] LGMM Laboratory, College of Technology, Université 20 Août 1955-Skikda, Algeria, e-mail: r.kelaiaia@univ-skikda.dz

Abstract: This paper is concerned with the analysis of the tracking capability of Relay Feedback Control Systems (RFCS). The envisioned application is the generation of Pulse-Width-Modulation (PWM) with variable duty-cycle and frequency known also as Duty-Cycle Modulation. In general, two main issues have to be solved with RFCS when used for regulation and tracking. The first issue concerns the determination of autonomous self-oscillations which are generated by the closed loop. The second issue concerns the determination of the relationship between the reference and the output signals. However, if the first issue has beneficiated from different approaches and has been solved particularly in case of zero reference signal, the second issue has got insufficient theoretical results because of mathematical difficulties for obtaining analytical expressions. Considering these reasons, a deep analysis of RFCS constituted of a hysteretic relay and linear systems of first order is presented. Analytical expressions relating self-oscillations and output mean values with respect to the reference signals are obtained. The analysis of these relationships led to infer some conditions under which the relay feedback control can generate commands for regulating and tracking reference signals. It highlights also the key role played by the hysteresis band width for applications based on RFCS. Our analysis, exploiting the analytical expressions, can be used to achieve a complete design for power converters. Moreover, simulation and experiments have confirmed our results.

Keywords: Relay feedback, On/Off control, PWM, tracking.

1. General information

RFCS have found place in many applications such as servomechanisms, trackers, power converters, sliding mode control systems, relay auto-tuners, sigma-delta modulators, etc. [1], [2]. In fact, by design, as other type of negative

feedback control systems, RFCS can be essentially considered as regulators or trackers since their outputs should follow their reference inputs as close as possible. In case of a constant reference signal set-point or desired signal, the problem corresponds to regulators. In case where the reference is a time variable signal or trajectory, the problem corresponds to a tracking one which is known as a servo problem.

It is well known that the most important characteristic of RFCS is their capability to autonomously generate stable self-oscillations (limit cycles) even without input excitations. Many systems are close to RFCS as they use switching mode called also "Bang-Bang" and "on-off" mode such as pulse-width modulators, sliding mode controllers, time optimal control systems, etc. Some theories based on state-space temporal approaches as well as harmonic approaches were developed to analyze RFCS. In effect, there are many approaches that enable to determine or approximate the self-oscillations that rise in these systems and their stability [1-4]. However, as noticed in [5], the vast majority of publications devoted to RFCS have focused on the analysis of the parameters of the oscillations and their stability. Conversely, the input-output problems did not produce enough results certainly because of mathematical difficulties in expliciting input-output relationships. For this reason, the simulation and the realization of real systems constitute alternatives to analyze input-output problems.

In a previous paper [6], [7], we have designed and realized some experimental prototypes of RFCS for designing and implementing power converters. We have studied and performed both simulations and experiments which have shown a tracking capability of the output with respect to the desired input. These systems revealed to be able to generate autonomously a pulse width modulation (PWM) with variable frequency.

In this paper, we present a deep analysis of these systems especially with a first order linear system. Based on the obtained analytical results, we infer the conditions under which these systems can be used as regulators and trackers.

2. Model of RFCS

A. *The proposed model*

There are many basic configurations of RFCS. We consider one type of model which is schematically presented in *Fig.1*. It has been already described in [6] and [7]. This system is constituted by a closed loop including in the forward path a symmetrical relay with a hysteresis band width noted $2 \cdot h$ and an output signal amplitude noted E. In the feedback path, it includes a linear first order system

with transfer function $H(s)$. The closed loop is followed by a linear system of second order or higher noted $G(s)$.

$G(s)$ is designed to filter the high frequencies contained in the on-off signals, and to extract the mean value which represents the tracking value. The involved variables are: the reference signal which is the input of the closed loop $r(t)$ to be tracked, the control signal $x(t)$ which represents the error $(x(t) = r(t) - z(t))$, the controlled signal $u(t)$, the feedback signal $z(t)$, and the output signal $v(t)$.
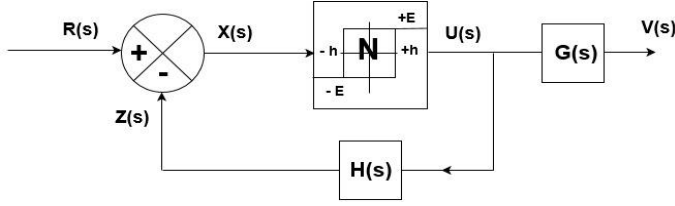

Figure 1: Model of an RFCS.

B. The behavior of the relay "N"

For the sake of simplicity, we assume that $x(t)$ the input signal of the relay has a triangular shape and can cross the threshold values ($\pm h$) at some specific instants t_k. Then, the relay output $u(t)$ will be a succession of alternating pulses of sign ($\pm E$). The instants during which the jumps occur are called the switching instants t_k. These instants are determined by the following conditions:

$$\begin{cases} \text{if} \quad (x(t) > +h \quad \text{and} \quad \dfrac{dx(t)}{dt} > 0) \quad \Rightarrow u(t) = +E \\ \text{if} \quad (x(t) < -h \quad \text{and} \quad \dfrac{dx(t)}{dt} < 0) \quad \Rightarrow u(t) = -E \end{cases} \quad (1)$$

with $x(t) = r(t) - z(t)$.

3. Tracking signals with RFCS

To illustrate the tracking capability of the RCFS, we will develop and analyze the relationship between the mean value of the output of the linear system (the tracker) and the reference input (the tracked signal). The elaboration of commands is automatically generated through the closed loop according to the conditions specified in (1). The commands are expected to be a sequel of On-Off state intervals generated by the relay output. It is well known that this

configuration of RFCS acts as a pulse with modulator (PWM), where the tracked information is contained in the On and Off durations of the relay impulses. Therefore, determination of these durations is a fundamental problem for designing applications based on this technique.

A. *Determination of switching times*

Consider the electrical circuit containing a resistor R and a capacitor C as presented in *Fig. 2*. It is a linear system of first order which corresponds to the system with transfer function $H(s)$ in *Fig. 1*. The input and the output of this system are respectively noted $u(t)$ and $z(t)$ according to *Fig. 2*.
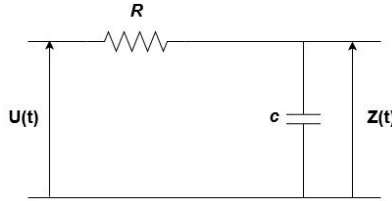

Figure 2: Linear filter of first order.

If the input signal of the relay feedback control is null, then, the closed loop generates a stable symmetrical self-oscillation of a square shape with a null mean value of the output $u(t)$ and $z(t)$. Thus, the only relevant problem is the determination of the frequency of the generated stable self-oscillations. For this purpose, many approaches have been proposed [3], [4], [5]. However, if the input signal to be tracked $r(t)$ is not null, the used approaches assume its slow variation compared to the on-off durations generated by the output relay. In this case, the analysis will be simplified by assuming that the input signal is constant: $r(t) \approx r_0$.

For the first order filter of *Fig. 2*, the output is a solution of the following differential equation:

$$\tau \cdot \frac{\mathrm{d}z_k}{\mathrm{d}t} + z_k = u(t) = (-1)^{k\cdot} \cdot E . \tag{2}$$

The subscript k denotes the intervals of commutation or pulse durations.

In case of a constant reference signal $r(t) = r_0$, the signal $u(t)$ is a sequence of unsymmetrical pulses taking alternately the values $u(t) = \pm E$ in a rectangular shape. To determine the switching instants and the durations of the control impulses, we proceed by integrating equation (2) under conditions (1).

B. Determination of pulse durations for a constant reference signal

By admitting the piecewise continuity over any time interval limited by two successive switching instants t_k and $t_{k+1} (k = 0, 1, 2, ...n)$, the integration of (2) under conditions (1) permits to determine the analytical results concerning the On and Off durations and consequently the period of the self-oscillation which are presented in [6].

To determine the pulse durations for a constant reference signal, let's consider *Fig. 3*, which represents the temporal evolution of the input $u(t)$ and output $z(t)$ of the linear filter described by equation (2).

If we consider intervals k which are even, the solution of (2) can be written in the form: $z(t) = z_0 \cdot e^{-t/\tau} + E$.

The instants of commutation during these intervals happen according to (1):

$$z(0) = z_0 + E = r_0 - h , \tag{3a}$$

$$z(T_1) = z_0 \cdot e^{-T_1/\tau} + E = r_0 + h , \tag{3b}$$

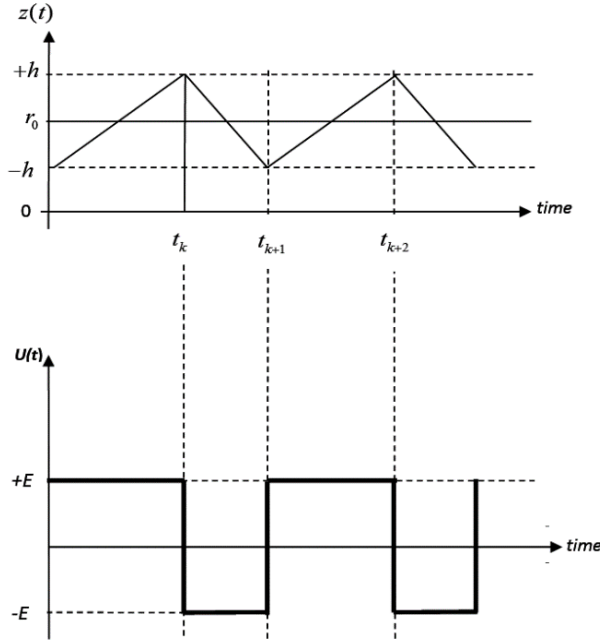where T_1 is the duration of positive impulses.

Figure 3: The input and output signals $z(t)$, $u(t)$

By combining (3a) and (3b), we get:

$$\frac{T_1}{\tau} = \ln\left(\frac{E - r_0 + h}{E - r_0 - h}\right) = \ln\left(\frac{1 + \dfrac{h}{E - r_0}}{1 - \dfrac{h}{E - r_0}}\right) = 2\cdot\arg\mathrm{th}\left(\frac{h}{E - r_0}\right). \quad (4)$$

If we consider intervals k which are odd, the solution of (2) can be written in the form: $z(t) = z_0 \cdot e^{-t/\tau} - E$. The instants of commutation during this interval happen according to (1).

$$z(0) = z_0 - E = r_0 + h, \qquad\qquad (5a)$$

$$z(T_2) = z_0 \cdot e^{-T_2/\tau} - E = r_0 - h. \qquad\qquad (5b)$$

T_2 is the duration of negative impulses. By combining (5a) and (5b), we get:

$$\frac{T_2}{\tau} = \ln\left(\frac{E + r_0 + h}{E + r_0 - h}\right) = \ln\left(\frac{1 + \dfrac{h}{E + r_0}}{1 - \dfrac{h}{E + r_0}}\right) = 2\cdot\arg\mathrm{th}\left(\frac{h}{E + r_0}\right). \quad (6)$$

The pulse duration (ON), T_1 can be expressed as:

$$T_1 = t_{k+1} - t_k = 2\cdot\tau\cdot\arg\mathrm{th}\left(\frac{h}{E - r_0}\right) \text{ under the condition } h < |E - r_0|. \quad (7)$$

The pulse duration (OFF), noted T_2 can be expressed as (4):

$$T_2 = t_{k+2} - t_{k+1} = 2\cdot\tau\cdot\arg\mathrm{th}\left(\frac{h}{E + r_0}\right) \text{ under the condition } h < |E + r_0|. \quad (8)$$

By manipulating the relations (7) and (8), it follows that for a constant reference input value r_0, the generated command $u(t)$ is a periodic signal of rectangular shape, with period $T = T_1 + T_2$, which can be expressed as follows:

$$T = 2\cdot\tau\cdot\arg\mathrm{th}\left(\frac{2\cdot h\cdot E}{E^2 - r_0^2 + h^2}\right). \qquad\qquad (9)$$

Comments:

- The obtained expressions (7), (8) and (9) are functions of the constitutive parameters of the system (h, E, τ), and of the reference signal r_0. We can observe that T_1, T_2 and T are biased by the value of the input signal r_0, which causes the dissymmetry of the commands. This fact reveals that the obtained PWM is of variable frequency.

We can notice that similar results have been obtained by applying the theory of Locus of a Perturbed Relay System (LPRS) [5]. Under the approximation of slow variation of the reference signal with respect to the period of self-oscillation, comparable results have been also obtained by [8].

- If we consider $r_0 = 0$ and $h \ll E$ in (9), then we can notice that the period T reduces to T_0.

$$T_0 = 4 \cdot \tau \cdot \arg\text{th}\left(\frac{h}{E}\right). \tag{10}$$

This means that if $r(t) = r_0 = 0$, the RFCS generates a self-oscillation which corresponds to a square-shaped signal of period T_0. Furthermore, this period T_0 is the smallest period the system generates and therefore corresponds to the maximum frequency the relay feedback can generate under the given configuration.

- *Fig. 4a* and *Fig. 4b* present the variation of the period and of the frequency of the self-oscillation w.r.t the reference input according to relation (7) and its reciprocal. These figures have been obtained for the parameters: $E = 12$ volts, $h = 1$, $\tau = 10$ s. We can observe from these figures that the period of self-oscillation increases in a quasi-quadratic manner with the increase of the reference input r_0 (see *Fig. 4a*). Inversely, the frequency of this self-oscillation decreases (*Fig. 4b*). However, we notice the presence of a singularity which is reflected by a discontinuity in *Fig. 4a* and *Fig. 4b*. This singularity occurs when the argument of the inverse of tangent hyperbolic function argth in (9) tends to unity, leading the period T to infinity. This corresponds to $\left(\dfrac{2 \cdot h \cdot E}{E^2 - r \cdot o^2 + h^2}\right) = 1$.

This leads to a condition that limits the maximal value of the reference signal which corresponds to the inequality:

$$\left|r_0^{\max}\right| < E - h. \tag{11}$$

Near this point of singularity $\left(r_0^{\max} = E - h\right)$, the RFCS can generate only very low frequencies. Therefore, the system cannot follow the reference signal and is useless in this region.

• There are also technical limitations for high frequencies imposed by the finite switching time (τ_{on} and τ_{off}) of the used switching elements such as electro-mechanic or electronic devices [7]. This fact leads to additional constraints like the following one which imposes that the pulse duration should be larger than the switching time of the used relays and switches. It can be expressed by the following expression:

$$T_1 = 2 \cdot \tau \cdot \arg \th \left(\frac{h}{E - |r_0|} \right) >> \max(\tau_{on}, \tau_{of}) .$$

(12)

Thus, the general condition to obtain a PWM is to impose that the minimal intervals of commutation should be much larger than the switching times of the relays and the used switches: $\min(T_1, T_2) \square \max(t_{on}, t_{off})$.

By observing *Fig. 4a* and *Fig. 4b* for different values of *h*, we conclude that the smaller the width of the hysteresis the more we avoid the singularity and the more the generated PWM satisfies the application requirements.
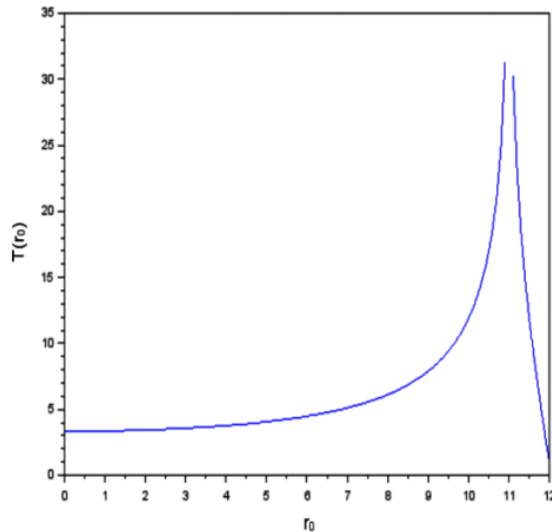
4a: Period
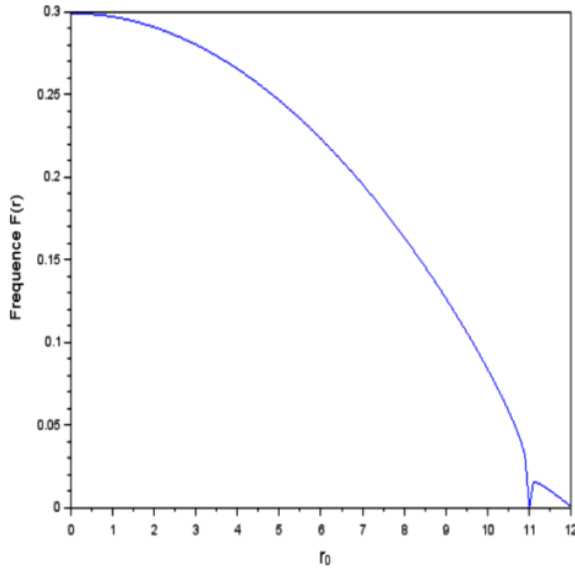
4b: Frequency of self-oscillation

Figure. 4: Curves of the period and the frequency of self-oscillation w.r.t. reference signal

4. Determination of the output mean value $u_m(r_0)$

To consider the tracking capability of our control system, we determine the mean value u_m of output $u(t)$, which is the measure of the dissymmetry of the periodic signal. It is determined by the following expression:

$$u_m = E \cdot \frac{(T_1 - T_2)}{(T_1 + T_2)}. \tag{13}$$

By replacing T_1 and T_2 from (3) and (4) in (9), the mean value is obtained in the form:

$$u_m(r_0) = \frac{\arg \operatorname{th}\left(\dfrac{2 \cdot h \cdot E}{E^2 - r_0^2 - h^2}\right)}{\arg \operatorname{th}\left(\dfrac{2 \cdot h \cdot E}{E^2 - r_0^2 + h^2}\right)} \cdot r_0. \tag{14}$$

- This expression highlights the relationship between the average value u_m of $u(t)$ and the target r_0 as well as the relay parameters of the RFCS (h, E). It is noteworthy to notice that it is independent from the time constant (τ) of the linear system. We notice also that this relationship is almost linear or quasi-linear if condition (11) is fulfilled. This means that the tracking of r_0 by $u(t)$ is effective as long as this condition holds. (see *Fig. 4*).
- Nevertheless, the analysis of expression (14) reveals the presence of two points of singularity that lead to discontinuities, one in the argument of the numerator and the second in the denominator. The first discontinuity occurs when the argument in the numerator $\left(\dfrac{2 \cdot h \cdot E}{E_0^2 - r_0^2 - h^2} \right)$ tends to unity. It imposes a discontinuity in the period of self-oscillation that corresponds to a value of the reference variable:

$$\left| r_{01} \right| = \sqrt{E^2 - 2 \cdot h \cdot E - h^2} = \sqrt{(E-h)^2 - 2 \cdot h^2} \ . \tag{15}$$

Similarly, the term in the denominator leads also to a discontinuity at the value of the reference such as:

$$\left| r_{02} \right| = E - h \ . \tag{16}$$

By comparing r_{01} and r_{02}, we have: $r_{01} < r_{02}$. Moreover, the value corresponds to (13), so that: $r_{01} = r_0^{\max}$.

Fig. 5 shows the evolution of $u_m(r_0)$ obtained for the parameters: $E = 12$ volts and $\tau = 10\,\text{s}$. To highlight the discontinuities, two curves are superimposed, each parameterized by a value of h. The left side curve corresponds to $h = 1$ volt while the right side one corresponds to $h = 3$ volts.

According to *Fig. 5*, the RFCS can only track reference signals in the range between $r_0 = 0$ and the vicinity from the left side of the first discontinuity $\left| r_{01} \right|$.

These last results limit seriously the regulating or tracking capability of RFCS. *Fig. 5* shows the two discontinuities. Near the vicinity of the discontinuity and beyond, the theoretical model is not applicable.

Again, by observing for different values of h, we conclude that the smaller the width of the hysteresis the more the relationship becomes linear and generates PWM that satisfies the application.
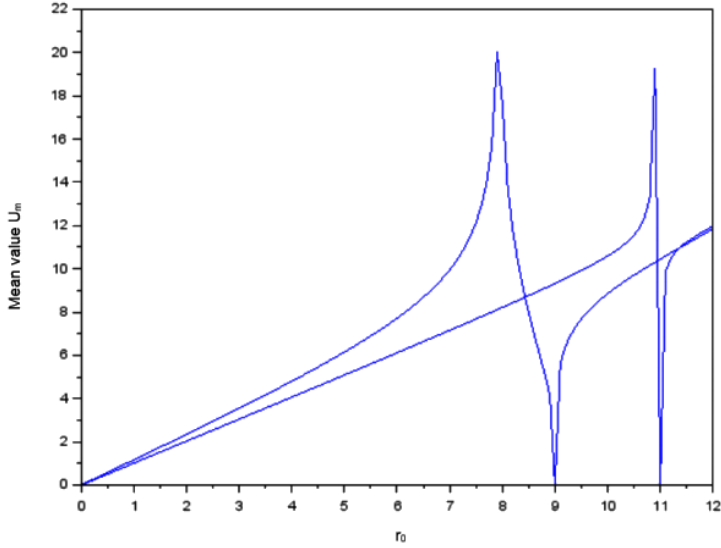
Figure 5: The mean value w.r.t the reference signal $u_m(r_0)$.

- On the other hand, if we consider the approximation $\arg\mathrm{th}(x) \cong x$, we can write u_m as:

$$u_m(r_0) = \left(\frac{E_0^2 - r_0^2 + h^2}{E_0^2 - r_0^2 - h^2} \right) \cdot r_0. \tag{17}$$

If we consider $\left(\dfrac{h}{E - |r_0|} \right) << 1$, the regulation effect of the RFCS appears in the derived expression: $u_m(r_0) \cong r_0$, which means that the mean value approximately follows the reference signal.

Determination of the Duty Cycle

We can estimate and highlight the dependency between the duty cycle and the reference signal r_0. The duty cycle can be defined as: $D(f_0) = \dfrac{T_1}{T}$. By replacing T_1 and T by their expressions in (7) and (9), we get the duty cycle:

$$D(r_0) = \frac{\text{arg th}\left(\dfrac{h}{E - r_0}\right)}{\text{arg th}\left(\dfrac{2 \cdot h \cdot E}{E^2 - r_0^2 + h^2}\right)}. \tag{18}$$

As the mean value of the relay output, the duty cycle depends on the reference signal and on the relay parameters $(h,\ E)$. The obtained PWM is thus performed at a variable frequency. If $r_0 = 0$, the duty cycle equals 1/2 which means that T_1 is half of the period T. This corresponds to a relay output of a square shape. The duty cycle w.r.t the reference signal is also subject to two singularities, one in the numerator and the second in the denominator. However, the two singularities are similar and occur if $|r_{02}| = E - h$, which corresponds to the relation already obtained in (16).

Fig. 6 is obtained for the parameters: $E = 12$ volts, $h = 1$ volt and $\tau = 10\,\text{s}$. It presents the evolution of the duty cycle with respect to the reference signal. We can notice the presence of a singularity that has to be avoided in order to have a useful generation of PWM. By observing *Fig. 6*, we conclude that the smaller the width of the hysteresis band the more the relationship becomes linear and the generated PWM is capable to regulate the output. This duty cycle is almost linear in a range from r_0 to r_{01}, but near the singularities, the behavior diverges in an exponential way. If $\dfrac{h}{E - |r_0|} \ll 1$, the duty cycle can be approximated by the following expression:

$$D(r_0) = \frac{T_1}{T} \cong \frac{1}{2 \cdot E} \cdot (E + r_0). \tag{19}$$

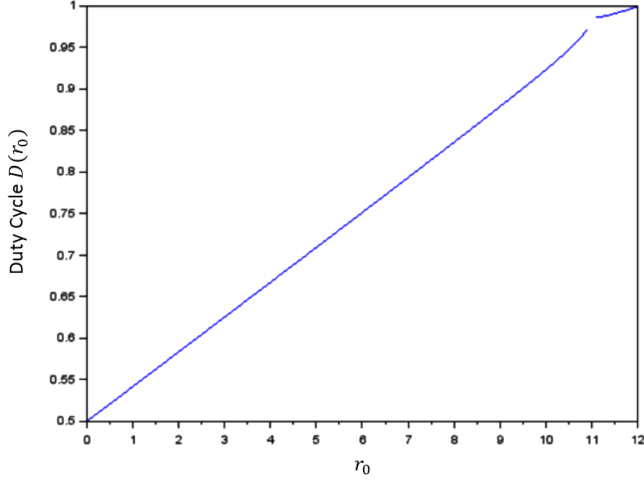Expression (19) shows a linear relationship between the duty cycle and the reference signal.

Figure 6: Duty cycle w.r.t reference signal

5. Special case: reference signal *r(t)* is variable

The case when reference signal is time variable corresponds to a tracking case. Analytical results are not easy to obtain. However, the obtained results for pulse durations in case of a constant value of the reference signal can be generalized under the assumption of a slow variation of the reference signal with respect to pulse durations. This way, we can consider *r(t)* as constant compared to pulse durations and then the obtained results can be locally generalized. Thus, if we approximate the pulse durations $T_1(r(t))$ and $T_2(r(t))$, then we can infer approximations for the period $T(r(t))$ and the frequency $F(r(t))$ of self oscillations, the mean value $u_m(r(t))$ and the duty cycle $D(r(t))$ which can be expressed as follows:

$$T_1(r(t)) = 2 \cdot \tau \cdot \arg \mathrm{th}\left(\frac{h}{E - r(t)}\right), \tag{20}$$

$$T_2(r(t)) = 2 \cdot \tau \cdot \arg \mathrm{th}\left(\frac{h}{E + r(t)}\right), \tag{21}$$

$$T(r(t)) = 2 \cdot \tau \cdot \arg \mathrm{th}\left(\frac{2 \cdot h \cdot E}{E^2 + h^2 - r^2(t)}\right), \tag{22}$$

$$F(r(t)) = \frac{1}{T((r(t)))} = \frac{1}{2 \cdot \tau} \cdot \frac{1}{\operatorname{arg th}\left(\dfrac{2 \cdot h \cdot E}{E^2 + h^2 - r^2(t)}\right)} \, . \tag{23}$$

With a similar configuration of an RFCS used as a DC/AC PWM with variable frequency inverter, under the assumption of slow variation of the reference signal compared to pulse durations, similar results to our approach have been obtained by [8]. As known in PWM systems, the tracking capability of our control system is expressed in the relationship of the mean value of the output signal $u(t)$ relatively to the reference signal. So, let's consider the $u_m(r(t))$.

$$u_m(r(t)) = \frac{\operatorname{arg th}\left(\dfrac{2 \cdot h \cdot E}{E^2 - h^2 - r^2(t)}\right)}{\operatorname{arg th}\left(\dfrac{2 \cdot h \cdot E}{E^2 + h^2 - r^2(t)}\right)} \cdot r(t) \, . \tag{24}$$

This can be written in the following form:

$$u_m(r(t)) = K(r(t)) \cdot r(t) \, . \tag{25}$$

From (24) or (25), we can observe that the tracking of the reference signal is automatically performed independently from its form. The factor $K(r(t))$ represents the distortion that affects the tracking process. With (9) fulfilled, the tracking error decreases if the following condition is satisfied:

$$\left(\frac{h}{E - \max|r(t)|}\right) << 1 \quad \text{or} \quad h << E - \max|r(t)| \, . \tag{26}$$

This condition enables to approximate (22) by the following expression, which expresses the tracking behavior of the considered RFCS:

$$u_m(r(t)) \cong r(t) \, . \tag{27}$$

The same reasoning can be made also in case of the duty cycle.

$$D(r(t)) = \frac{\operatorname{arg th}\left(\dfrac{h}{E - r(t)}\right)}{\operatorname{arg th}\left(\dfrac{2 \cdot h \cdot E}{E^2 + h^2 - r^2(t)}\right)} \, . \tag{28}$$

If we consider the condition in (26), the duty cycle can be approximated in a

linear form as

$$D(r(t)) \equiv \frac{1}{2 \cdot E}(E + r(t)). \tag{29}$$

We can see that the tracked information $r(t)$ can be extracted from the duty cycle according to (29) since $r(t) = E \cdot (2 \cdot D(r(t)) - 1)$.

The relationship between the duty cycle and the reference signal is almost linear.

6. Results and discussion

The simulation of the relay feedback control has been performed for various parameters. A model of the studied RFCS with a Simulink implementation using a first order linear system in the feedback and a relay with symmetrical hysteresis is presented in *Fig. 6.*
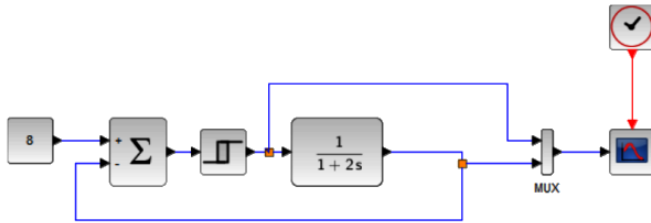

Figure 7: Scheme for simulation

We illustrate this simulation with some results. *Fig. 7* shows the adopted model used for generating the PWM related to the application in DC-DC converter control. Some simulation results are presented below. *Fig. 8a*, *Fig. 8b* and *Fig. 8c* present the output of the relay $u(t)$ in black color and the output of the linear system $z(t)$ with green color. The relay parameters are: $h = 1$ volt and $E = 10$ volts. The time constant of the linear system is 2 seconds, and the amplification factor equals the unity.

The first group of results concerns the use of the RFCS as a regulator. The results are presented in *Fig. 8a*, *Fig. 8b* and *Fig. 8c,* for the values of the reference r_0 : 0, 4 and 8 Volts, respectively. We can observe that the command is piecewise continuous and switches alternatively between the two extreme values. $u(t)$ belongs to the set $E = 10$ volts and $E = -10$ volts. The output is also piecewise continuous and is bounded by the hysteresis limits $(\pm h)$. In the following figures, the output signal $z(t)$ is represented in green color. $z(t)$ tracks the reference

signal r_0. We notice the correspondence with the theoretical results. The second group of simulation concerns the use of our RFCS as a tracker of input signals having a sine wave shape.
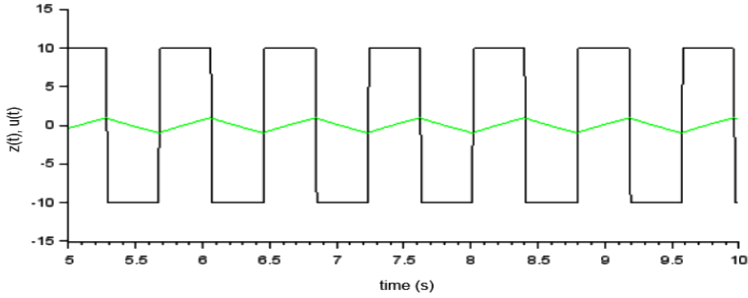
8a: $r_0 = 0$ volts
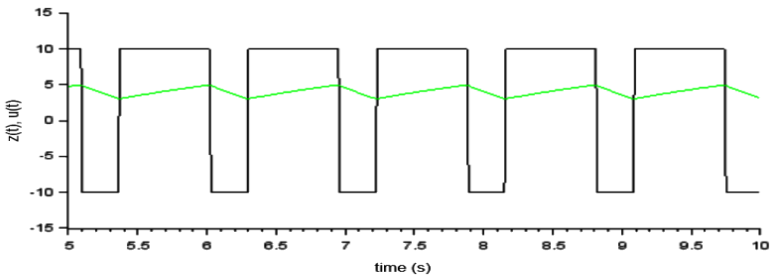
8b: $r_0 = 4$ volts
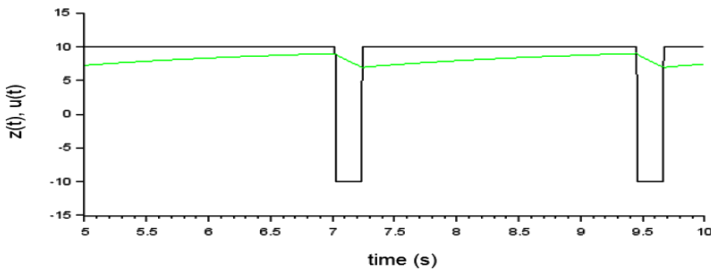
8c: $r_0 = 8$ Volts

Figure 8: $z(t)$ and $u(t)$ for different values of r_0

This application corresponds to power inverters DC/AC. The relay parameters are: $h = 1$ volt and $E = 12$ volts. The time constant of the linear system is 1 second, and the amplification factor equals the unity. Some simulation results are

presented in *Fig. 9a*, *Fig. 9b* and *Fig. 9c*. They show the relay output $u(t)$ in black color and the linear system output $z(t)$ with green color. The reference signal is a sinewave with an angular frequency $\omega = 2$ rad/s. The results are obtained for amplitudes which are: 2, 4 and 6 Volts, respectively. The output is also piecewise continuous and is bounded by the hysteresis limits $(\pm h)$. The input $r(t) = r_0 \cdot \sin(w \cdot t)$ is tracked by the output $z(t)$ which is represented by the green colors in the concerned figures. We notice the correspondence with the theoretical results.

The third group of simulation concerns the use of our RFCS as a tracker of sine signals for different values of the frequency of the reference signal. The relay parameters are: $h = 1$ volt and $E = 12$ volts. The reference signal is a sine wave with a constant amplitude of 4 Volts and angular frequencies of: 1, 2 and 3 rad/s, respectively. The results are presented in *Fig. 10a*, *Fig. 10b* and *Fig. 10c*. We can observe that the command is piecewise continuous and switches alternatively between the two extreme values $u(t)$ ($+E = 12$ volts and $E = -12$ volts). The output is also piecewise continuous and is bounded by the hysteresis limits $(\pm h)$. We can observe that the input $r(t)$ is tracked by the output $z(t)$ which is represented by the green color in the concerned figures.

Note:

An experimental system has been built up. It has been successfully used to test some theoretical results. It has been exploited to generate Pulse Width Modulation (PWM) in a chopper application with feedback through a first order filter. It has also been adapted to the case of a feedback through a second order filter and for tracking various reference signals. For more information and details about these experiments, the interested reader can refer to [6].
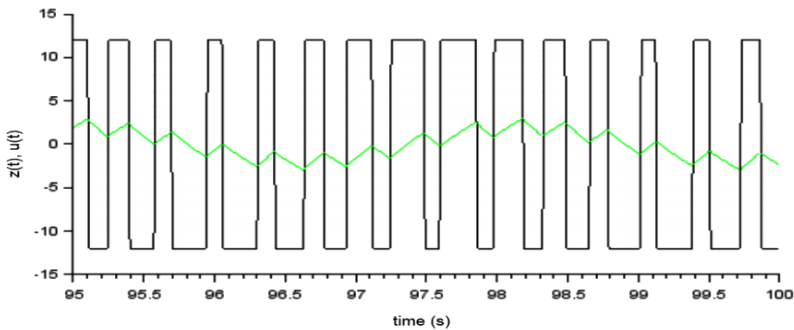
9a: $r_0 = 0$ volts
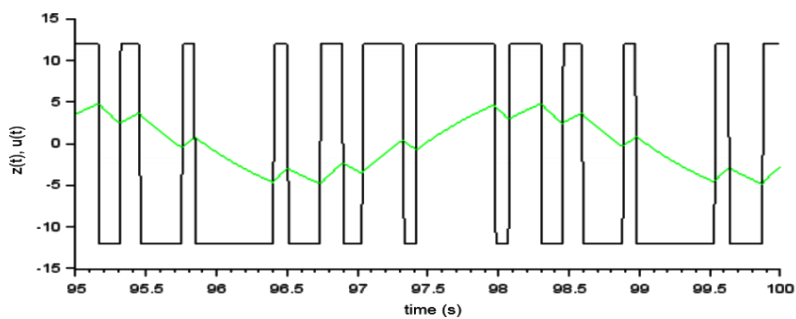
9b: $r_0 = 4$ volts
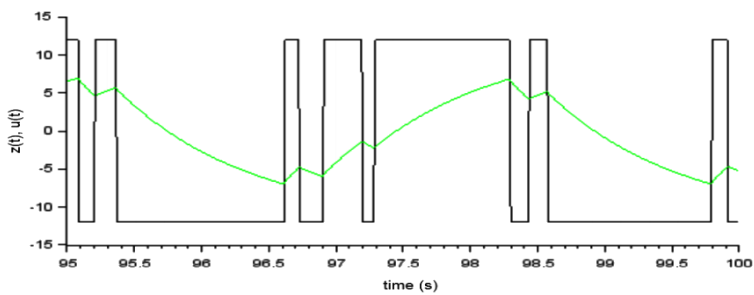
9c: $r_0 = 8$ volts

Figure 9: $z(t)$ and $u(t)$ for $r(t) = r_0 \cdot \sin(\omega \cdot t)$ with different values of r_0
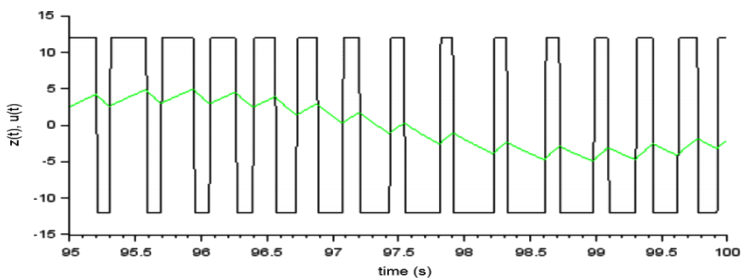
10a: $\omega = 1\,\text{rad/s}$
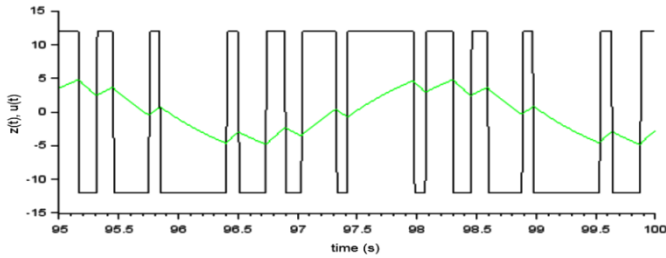
10b: $\omega = 2$ rad/s
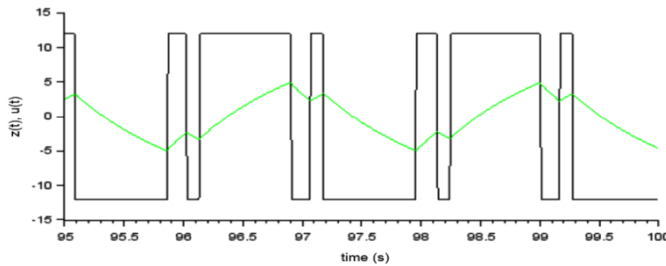
10c: $\omega = 3$ rad/s

Figure 10: $z(t)$ and $u(t)$ for different values of the frequency

8. Conclusion

A study of an RFCS constituted of a relay with symmetrical hysteresis and a linear first order filter feedback circuit has been presented. The pulse durations and the period of self-oscillations in case of constant reference signals have been established. The RFCS generates a PWM with variable frequency and variable duty-cycle. The conditions under which the regulation and the tracking are possible have been analyzed. The conditions for tracking under the assumption that the signal varies slowly in comparison to the pulse durations of the self-oscillations have been extended. Our analysis has led to the conclusion that the width of hysteresis band plays a key role in the design of trackers based on PWM techniques. For applications such as choppers, a complete design can be achieved based on the mathematical expressions obtained in the paper. For DC-AC inverters, the design based on our results is useful but imposes more constraints, since it depends on both the amplitude and the frequency of the sine wave reference signal. For arbitrary signals, the possibility and quality of the tracking depends on the amplitude and on frequencies contained in the reference signals.

However, for such complex reference signals, the simulation and the realization of experimental prototypes are essential tools for testing the possibilities and the performances of our RFCS in order to confirm their usefulness according to the requirements of the application at hand.

References

[1]   Atherton, D. P., "Early developments in nonlinear control", in *IEEE Control Systems Magazine*, vol. 16, no. 3, pp. 34-43, June 1996, doi: 10.1109/37.506396.

[2]   Holmberg, U., "Relay feedback of simple systems", Ph.D. thesis TFRT-1034, Department of Automatic Control, Lund Institute of Technology, Lund, Sweden, 1991.

[3]   Tsypkin, Ya.Z., "Relay Control Systems", Cambridge University Press, Cambridge, UK, ISBN: 0521243904 9780521243902, 1984.

[4]   Hamel, B., "A mathematical study of on-off controlled higher order systems", in *Proceedings of the Symposium on Nonlinear Circuit Analysis*, Polytechnic Institute of Brooklyn, New York, vol. 6, pp. 225–232, 1956.

[5]   Boiko, I., "Discontinuous Control Systems, Frequency-Domain Analysis and Design", Birkhäuser Boston, a part of Springer Science+Business Media, LLC, ISBN: 978-0-8176-4752-0. 2009.

[6]   Zaatri, A., Belhour S., "Etude et réalisation d'un hacheur PWM", *Revue des Energies Renouvelables,* vol. 13, no. 1, pp. 187-198, 2010.

[7]   Zaatri, A., Azzizi, N., Rahmani, F., "Minimization of energy losses into a PWM chopper", *World Journal of Engineering*, vol. 11, no. 4, pp. 441-446, 2014. https://doi.org/10.1260/1708-5284.11.4.441, 2014.

[8]   Lordejani, S., N., Yazdanpanah., M., J., "Sliding Mode Pulse Width Modulation for Voltage Control of a Voltage Source Inverter", *23rd Iranian Conference on Electrical Engineering,* 2015, pp. 1642 - 1646.

Model-Based Control Strategy for Autonomous Vehicle Path Tracking Task

Ahmad REDA [1], József VÁSÁRHELYI[2]

[1] Institute of Automation and Info-communication, Faculty of Mechanical engineering and Informatics, University of Miskolc, Miskolc, e-mail: autreda@uni-iskolc.hu
[2] Institute of Automation and Info-communication, Faculty of Mechanical engineering and Informatics, University of Miskolc, Miskolc, e-mail: autreda@uni-iskolc.hu

Abstract: Despite the advanced technologies used in recent years, the lack of robust systems still exists. The automated steering system is a critical and complex task in the domain of the autonomous vehicle's applications. This paper is a part of project that deals with model-based control strategy as one of the most common control strategies. The main objective is to present the implementations of Model Predictive Control (MPC) for an autonomous vehicle steering system in regards to trajectory tracking application. The obtained results are analysed and the efficiency of the use of MPC controller were discussed based on its behaviour and performance.

Keywords: Model based control, Model Predictive Control (MPC), trajectory tracking, degree of freedom (DOF), dynamic vehicle model.

1. Introduction

In recent years with the significant increase in the number of vehicles on the roads, many types of research and reports have raised the attention to the fact of increase the risk of road safety issues such as traffic congestion and car accidents which are caused by human errors. In this context, the autonomous vehicles have gained more attention as a solution to overcome these challenges, in addition to the other benefits it provides in terms of better fuel economy provision and reducing the pollution [1], [2]. The autonomous vehicle's applications can be divided into 3 main modules: Sensing and Perception, Planning and Control. Sensing and Perception is the fundamental module that provides the information of the driving environment to the vehicle letting the system know the surrounding environment in real-time such as surrounding obstacles, velocity, and vehicle location. In the planning module, the system

uses data provided by the previous sub-system (Sensing and Perception) to determine the safest and the most appropriate trajectory to be followed by the vehicle. In the Control module, the control strategies are applied to control the actuators of the different parts of the system in order to drive and steer the vehicle along the desired path [3]. Improving the automated steering system in order to develop a highly secure, stable and easy to drive autonomous vehicle has gained significant interest [4]. The vehicle models that can be used in trajectory tracking problems can be divided into three mains categories: Geometric, Kinematic and Dynamic vehicle models with several control strategies [5]. The paper presents preliminary research results of the proposed MPC controller based on the dynamic model and it is structured as follows: in the first section, the autonomous vehicle system review is presented. Second section describes the dynamic vehicle model and control strategy. The design of the vehicle model and the MPC controller are described in section three. In section four, the implementations and the obtained results are discussed. The conclusions of the paper are presented in section five.

2.   Autonomous vehicles model and control strategy

The vehicle model plays an essential role in regards to the system simulations process, which is a crucial stage in the development process of the controllers. In the simulation process, the properties of the controller are defined and the parameters are tuned in order to achieve the best performance. The vehicle (like robot) model can be divided into two main classes, holonomic system and non-holonomic system based on the number of controllable degrees of freedom (DOF) against the total number of DOF. In a holonomic system, the number of controllable degrees of freedom is equal to the total number of DOF. In contrast, a system with number of controllable degrees of freedom less than the total number of DOF is called a non-holonomic system. It is worth to mention that most of the vehicles are considered as non-holonomic due to the fact that only two degrees of freedom are controllable (the lateral positions and the longitudinal directions) [6], [7]. One more thing to take into consideration is that the vehicle model can be reduced to be two – tire models which is called a bicycle model. In bicycle models the right and the left tires are assumed to have the same behaviour. Trajectory tracking tasks based on [8], [9], can be divided into three main motion tasks which are, trajectory tracking, path following and point to point motion.

2.1 Dynamic Vehicle Model

Kinematic, Geometric and Dynamic models are the three main types of path tracking tasks. Unlike Geometric and kinematic model, the dynamic model considers the internal and external forces and describes the motion of the vehicle with respect to its position, velocity and acceleration. *Fig. 1* shows the dynamic vehicle model, where θ is the vehicle heading, v is vehicle velocity, δ_R and δ_F denote the rear and front steering angle respectively, F_F and F_R are the lateral forces that are applied on the front and rear tires respectively, L is the wheelbase of the vehicle, L_F and L_R are the rear and front half-wheelbases respectively, G is the gravity force, β_F and β_R are the sideslip angles of the front and rear wheels respectively [10], [11].
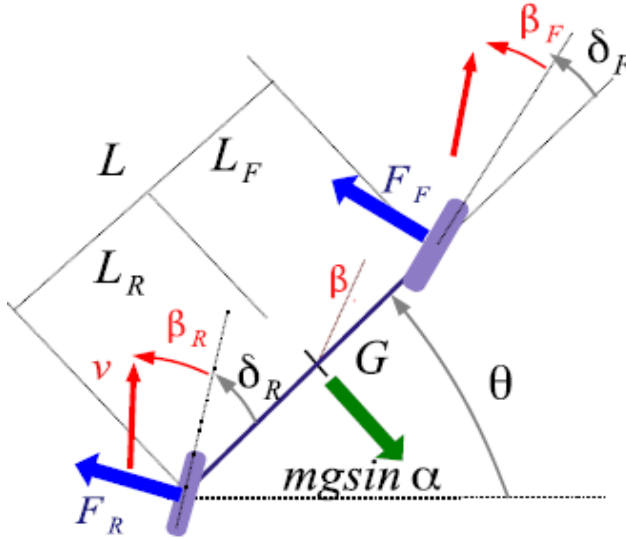
Figure 1: Dynamic vehicle model

2.2 Dynamic Controller

In the path tracking task, the control law of the dynamic controller includes the dynamic properties of the system. Taking the effects of the vehicle dynamics into consideration naturally makes the dynamic controllers more efficient and stable compared to geometric and kinematic controllers [12]. However, dynamic feedback (such as the torque) is required for this type of control strategy, which in turn requires a special type of sensors and more data processing. Several studies can be found regarding the use of the dynamic control strategy for autonomous vehicle tasks [13], [14]. In this paper, Model

Predictive Control strategy was used to control the autonomous vehicle model as a dynamic control strategy. Model Predictive Controller (MPC) is an optimization strategy for model-based control, and it can be implemented for linear and nonlinear systems. The optimization process is achieved by selecting the optimal values of the plant model which in turn provides the optimal performance in terms of tracking the reference output. MPC controller uses the plant model to simulate the vehicle path (for vehicle path tracking task) in the next P time steps (prediction horizon), meaning that it looks forward to make the predictions. MPC strategy uses different scenarios to achieve the optimization, where the optimal scenario is the one that minimizes the error between the predicted and the reference trajectory. MPC is an effective strategy for the systems where the model dynamics are unchanged [15].

3. Design of the MPC controller

Model Predictive Controller is used to control the front steering angle of the vehicle by means of adjusting and driving the lateral deviation (d) and the relative yaw angle (θ) to be very close to zero (see *Fig. 2*). To design an MPC controller, the model of the vehicle is created in the first step, and the parameters of the MPC are designed in the second step.

3.1 Design of the Dynamic Model of the Vehicle

In this paper, the bicycle model is used to describe the dynamics of the vehicle. *Fig. 2* shows the global position of the vehicle in (X, Y) axes. v_x is the longitudinal velocity and v_y is the lateral velocity. The vehicle model is described with the following parameters: total mass of the vehicle(m), yaw moment of the vehicle inertia(l_z), the distance from the front tires to the centre of gravity (l_f), the distance from the rear tires to the centre of gravity(l_r), the cornering stiffness of front tire (c_f), and the cornering stiffness of rear tire (c_r). The lateral motion and yaw motion are determined by the fundamental laws of motion, meaning that they are determined by forces which are (in this case) the forces that are applied on front and rear tires [16], [17].
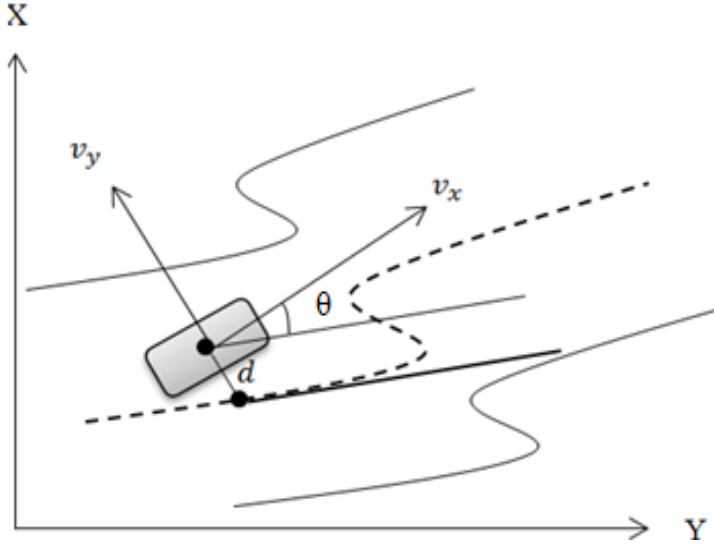
Figure 2: Position of vehicle model

Equations (1-a), (1-b) and (1- c) describe the lateral dynamics of the vehicle, where m is the mass of the vehicle, a_y is the acceleration in lateral direction y , ω is the yaw rate, F_F and F_R are the lateral forces that are applied on the front and rear tires, respectively.

$$ma_y = \textstyle\sum_i F_{y,i} = F_F + F_R \tag{1-a}$$

$$a_y = \dot{v}_y + \omega v_x \tag{1-b}$$

$$m(\dot{v}_y + \omega\, v_x) = F_F + F_R \tag{1-c}$$

The yaw dynamics of the vehicle is described by the sum of the all moments about the central gravity G (moments generated by front and rear tires) as (2) shows. Regarding to linear tire model, the tire forces are proportional to the corresponding slip angles (β_F, β_R) and the corner stiffness of the front and rear wheels (c_f, c_r) as equations (3-a) and (3-b) describe.

$$l_z\dot{\omega} = l_f F_F + l_r F_R \tag{2}$$

$$F_F = c_f \beta_F \tag{3-a}$$

$$F_R = c_r \beta_R \tag{3-b}$$

The bicycle model can be described as continuous state space representation as it is shown in (4) where:

States: $x_1 = v_y, x_2 = \theta, x_3 = \omega$.
Input: u=δ.

$$\frac{d}{dt}\begin{bmatrix} x_1 \\ x_2 \\ x_3 \end{bmatrix} = \begin{bmatrix} \dot{y} \\ \dot{\theta} \\ \dot{\omega} \end{bmatrix} \begin{bmatrix} \frac{-(2C_f + 2C_r)}{mv_x} & 0 & -v_x - \frac{-(2c_f l_f - 2c_r l_r)}{mv_x} \\ 0 & 0 & 1 \\ \frac{-(2C_f l_f - 2C_r l_r)}{I_z v_x} & 0 & \frac{-(2C_f l_f + 2C_r l_r{}^2)}{I_z v_x} \end{bmatrix} \begin{bmatrix} x_1 \\ x_2 \\ x_3 \end{bmatrix} + \begin{bmatrix} \frac{2c_f}{m} \\ 0 \\ \frac{2c_f l_f}{I_z} \end{bmatrix} \delta \quad (4)$$

The full discretized model for MPC controller is obtained by discretizing the continuous state space model using sample time ($T_s = 0.1$). In the next step the parameters of the controller need to be determined.

3.2 Design of the MPC model

The first step in the process of designing the MPC controller is to set the channels and the signal types of the plant model. In other words, to set the input and output channels. The signal types of input channels are: Manipulated variables (MV), Measured Disturbances (MD) and Unmeasured Disturbances (UD), whereas output channels are: Measured Outputs (MO) and Unmeasured Outputs (UO). In default configuration, all the inputs are considered as manipulated variables and all outputs are measured outputs. The MPC plant model in this paper was designed with two inputs, therefore the first and second input channels were set as MV for steering angle and MD for road yaw angle rate. respectively. In addition to the inputs, the model has four measured outputs, which are: lateral deviation, relative yaw angle, lateral velocity, and yaw rate ($\omega = \dot{\psi}$) as it is shown in *Fig. 3*. Yaw rate is the rotation rate of the car or in other words the changing rate of the heading angle of the car. Generally speaking, in the course of designing the parameters of an MPC controller, several recommendations can be taken into consideration [15]. In addition to design the parameters, the constraints of the manipulated variable (steering angle) were set as *Table 1* shows.
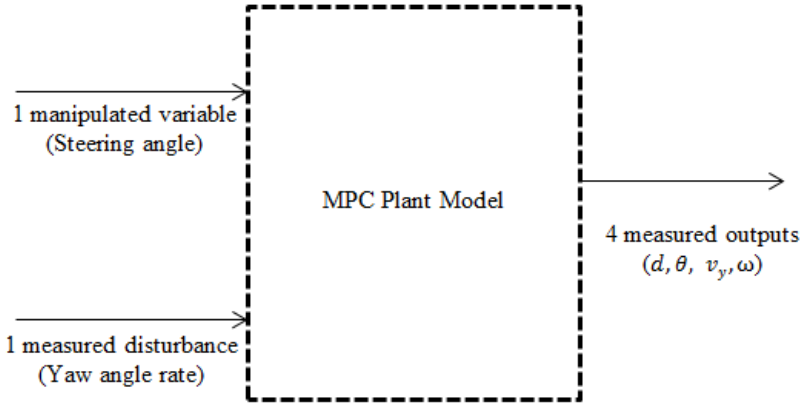
Figure 3: Inputs and outputs of MPC Plant model.

Table 1: Constraints and Parameters of the MPC controller

Parameters	
Sample Time (T_s)	0.1 seconds
Prediction Horizon (P)	20 seconds
Control Horizon (M)	20 seconds
Constraints	
Steering Angle (δ)	[-1.04 – 1.04] rad
Changing Rate of Steering Angle	[-0.26 – 0.26] rad

4. Simulation and results

For the simulation process, the weights of the inputs and outputs of the controller were determined as it is shown in *Table 2*. It is worth to point out that non-zero values were assigned to the variables which have a reference to follow and the weight refers to the priority of the variables, where the high weight indicates high priority.

Table 2: Parameters' weights of MPC controller

Parameter	Weight
Change of steering angle	0.1
Lateral deviation	1
Yaw Angle	0.1
Lateral Velocity	0
Yaw Rate	0

After determining the weights of the parameters, the inputs of the MPC controller were defined (reference trajectory, longitudinal velocity, lateral deviation and relative yaw angle). The reference trajectory can be determined in two different ways, the first one is by using the Driving Scenario Designer Toolbox in MATLAB, where the waypoints can be determined in order to create lane –change maneuver, and in this case, the reference yaw angles and lateral positions will be determined automatically by the toolbox. The second way (used in this paper) is by generating future lane curvature, which is used to calculate the lateral deviation and relative yaw angle of the created lane (see *Fig. 4*). The longitudinal velocity is considered a constant parameter.
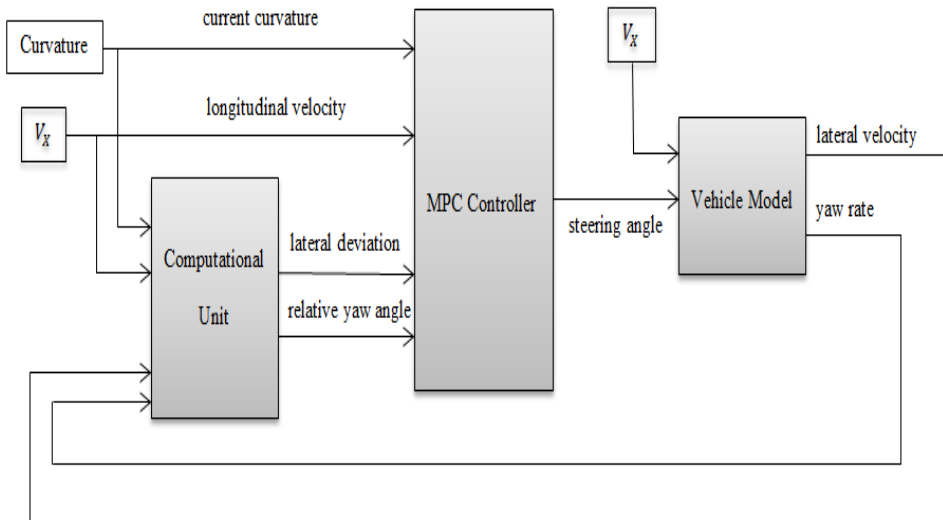
Figure 4: General Model of MPC and plant for Simulink

Fig. 5 shows the output control actions (steering angles) of the MPC controller after running the simulation, while *Fig. 6* and *Fig. 7* show the effects of these control actions on the lateral deviation and relative yaw angle which describe the performance of the controller.

Steering angle (deg)
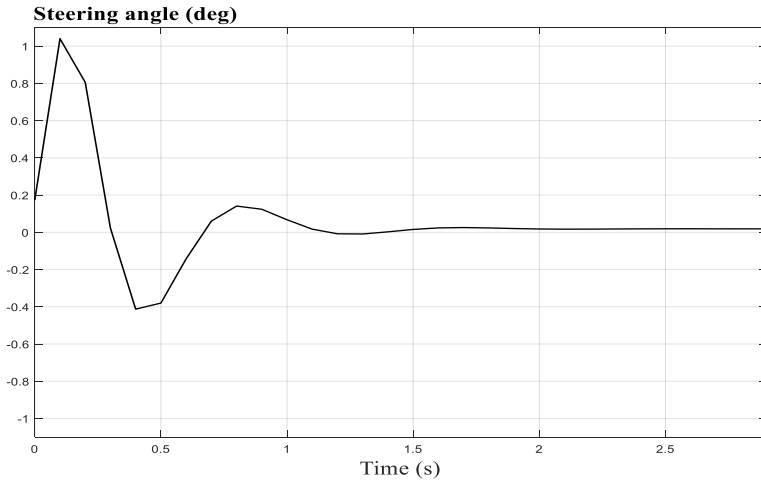
Figure 5: Control Actions of the MPC Controller

Lateral Deviation (m)
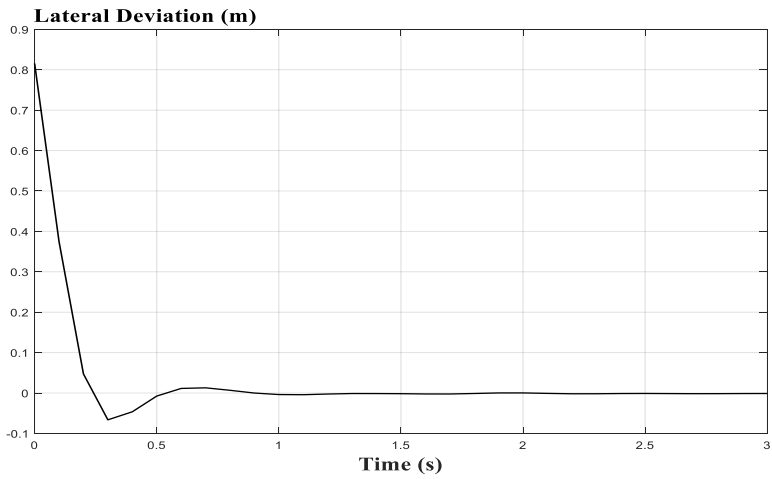
Figure 6: Lateral deviation resulting from the MPC implementation
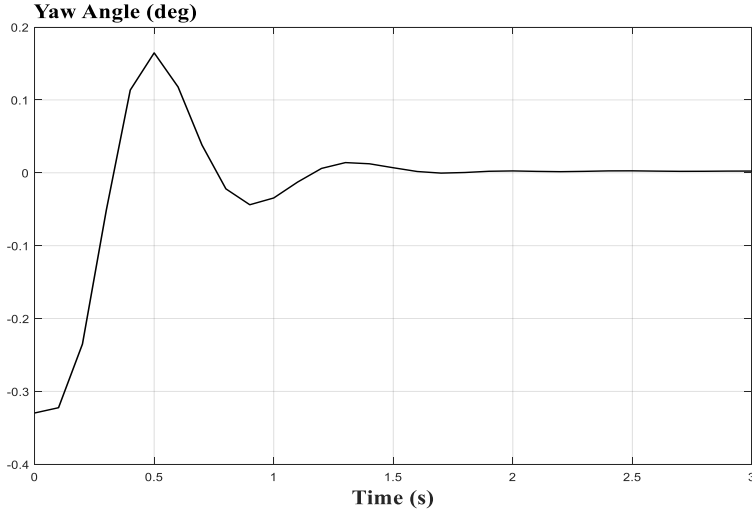
Figure 7: Relative yaw angle resulting from the MPC implementation

The obtained results show that the MPC controller succeeded in providing control actions that drive both relative yaw angle and lateral deviation to be very close to zero, meaning that, the designed MPC controller drove the autonomous vehicle along the reference path efficiently.

5. Conclusions

In this paper, a dynamic vehicle model and model based control strategy (model predictive controller) were used to implement trajectory tracking task for autonomous vehicle. The designed MPC controller succeeded in driving the vehicle within the desired trajectory by providing optimal control actions. Designing the vehicle model taking in consideration the internal and external forces and the well-designed MPC parameters played the essential role in achieving the satisfactory performance.

Acknowledgements

References

[1]   Fagnant, D. J., and Kockelman, K., "Preparing a nation for autonomous vehicles: opportunities, barriers and policy recommendations", *Transportation Research Part A: Policy and Practice*, pp. 167-181, 2015.

[2]   Department for Transport, "Research on the Impacts of Connected and Autonomous Vehicles (CAVs) on Traffic Flow: Summary Report", Atkins Ltd, 2017.

[3]   Pendleton, S. D. et al., "Perception, planning, control, and coordination for autonomous vehicles", *Machines*, vol. 5, no. 1, pp. 1-54, 2017.

[4]   Park, M., Lee, S., and Han, W., "Development of Steering Control System for Autonomous Vehicle Using Geometry-Based Path Tracking Algorithm", *ETRI Journal*, DOI: 10.4218/etrij.15.0114.0123, vol. 37, no. 3, pp. 617–625, 2015.

[5]   Bacha, S., Ayad, M. Y., Saadi, R., Aboubou, A., Bahri, M., and Becherif, M., "Modeling and control technics for autonomous electric and hybrid vehicles path following", *5th International Conference on Electric Engineering-Boumerdes-Boumerdes (ICEE-B)*, 2017.

[6]   Katrakazas, C., Quddus, M., Chen,W.-H., and Deka, L., "Realtime motion planning methods for autonomous on-road driving: State-of-the-art and future research directions", *Transp. Res. C: Emerg. Technol*, vol. 60, pp. 416 – 422, 2015.

[7]   Siegwart, R., Nourbakhsh, I., and Scaramuzza, D., "Introduction to Autonomous Mobile Robots", MIT Press, 2011.

[8]   Aguiar, A. P., and Hespanha, J. P., "Hespanha Trajectory-tracking and path-following of underactuated autonomous vehicles with parametric modeling uncertainty", *IEEE Transactions on Automatic Control*, vol. 52, no. 8, pp. 1362-1379, 2007.

[9]   Den Broeck, L. V., Diehl, M., Swevers, J., "Model predictive control approach for time optimal point-to-point motion control", *Mechatronics*, vol. 21, no. 7, pp.1203-1212, 2011.

[10] Amer N.H., Zamzuri H., Hudha K., and Kadir Z.A, "Modelling and control strategies in path tracking control for autonomous ground vehicles: A review of state of the art and challenges", *J. Intell. Robot. Syst*, DOI 10.1007/s10846-016-0442-0, vol. 86, no. 2, pp. 225-254, 2017.

[11] Lucet, E., Lenain, R., and Grand, C., "Dynamic path tracking control of a vehicle on slippery terrain", *Control Engineering Practice*, DOI: 10.1016/j.conengprac.2015.05.008, vol. 42, pp. 60-73, 2015.

[12] Poussot-Vassal, C., Sename, O., Dugard, L., and Savaresi, S. M., "Vehicle dynamic stability improvements through gain-scheduled steering and braking control", *Vehicle System Dynamics*, vol. 49, no. 10, pp. 1597-1621, 2011.

[13] Benine-Neto, A., Scalzi, S., Mammar, S., and Netto, M., "Dynamic controller for lane keeping and obstacle avoidance assistance system", *13th International IEEE Conference on Intelligent Transportation Systems (ITSC)*, pp. 1363–1368, 2010.

[14] Zhao, P., Chen, J., Mei, T. and Liang, H., "Dynamic Motion Planning for Autonomous Vehicle in Unknown Environments", in *Proceedings of IEEE Intelligent Vehicles Symposium (IV)*, pp. 284–289, 2011.

[15] Reda, A., Bouzid, A., and Vásárhelyi, J., "Model Predictive Control for Automated Vehicle Steering", *Acta Polytechnica Hungarica*, vol. 17, no. 7, pp. 163-182, 2020.

[16] Turri, V., Carvalho, A., Tseng, H. E., Johansson, K. H., and Borrelli, F., "Linear model predictive control for lane keeping and obstacle avoidance on low curvature roads", *Proc. IEEE Conf. Intell. Transp. Syst.*, pp. 378-383, 2013.

[17] Katriniok, A., Maschuw, J. P., Christen, F., Eckstein, L., and Abel, D., "Optimal vehicle dynamics control for combined longitudinal and lateral autonomous vehicle guidance", in *Proc. IEEE Eur. Control Conf*, pp. 974-979, 2013.

The Impact of Integrated Maintenance Actions Optimization on Strategic Machines Lifetime

Mohammed Abdellatif BENSACI[1], Aoul Elias HADJADJ[2]

[1] Department of Hydrocarbon production, Faculty of Hydrocarbons and Energies Renewables and pieces of land, University of Ouargla, Algeria, e-mail: bensaci.ab@ouargla-univ.dz& abdelatif.bensaci@gmail.com
[2] Department of Electromechanics, Faculty of Engineering Sciences University of Annaba, Algeria e-mail: hadjadj.elias@yahoo.fr

Abstract: This article is based on the quantitative study of reliability, maintainability, availability (*RMA*), on the Pareto diagram (*ABC*) and on the analysis of the failure modes and their impact on criticality (*FMECA*). The developed approach aims, at first, implementing two optimization procedures (code development, Simulink modelling in MATLAB) and using two methods (graphical, analytic) of the Weibull parameters. The results obtained via code (which is based on the Weibull graph method of two parameters) are a bit divergent. The evaluation criteria are rather far from that of the model (which is based on the maximum likelihood of three-parameter Weibull distribution). This will allow to locate the critical elements, and to determine the systematic preventive time of replacements. An application case validates the proposed study objective.

Keywords: Optimization, Maintenance, Weibull, MATLAB, Impact, Maximum likelihood

1. Introduction

In a context of maintaining the strategic machines of the hydrocarbon sector, particularly that of the processing units at high levels of readiness, the optimization of maintenance actions *RMA*, *ABC*, *FMECA* is one of the key elements to consider to have an impact on the readiness during the lifetime of these machines and especially that of the critical element. An integrated maintenance approach integrates several steps aimed at this objective, using a Simulink model and a calculation code in MATLAB.

In the first step, a historical file analysis on the selected machine in a fixed period of time is made, which will enable carrying out the quantitative study of *RMA*, *ABC* in order to optimize the parameters of performance and to have their

impact on lifetime. For this study, several laws of distribution can be applied, in particular the Weibull one, whose main properties are expressed by the table below:

Table 1: Main properties of the Weibull-distribution [1]

Reliability	Density of probability	Function of division	Failure rate
$R(t) = e^{-\left[\frac{t-\gamma}{\eta}\right]^{\beta}}$	$f(t) = \frac{\beta}{\eta}\cdot\left[\frac{t-\gamma}{\eta}\right]^{\beta-1}\cdot e^{-\left[\frac{t-\gamma}{\eta}\right]^{\beta}}$	$F(t) = 1 - e^{-\left[\frac{t-\gamma}{\eta}\right]^{\beta}}$	$\lambda(t) = \frac{f(t)}{R(t)} = \frac{\beta}{\eta}\left[\frac{t-\gamma}{\eta}\right]^{\beta-1}$

β: Shape parameter (*without unit*);
η: Scale parameter (*unit of time*);
γ: Position parameter (*unit of time*).

These optimized parameters are based on the form parameter β and the average operating time before the first failure, or meantime before failure *MTBF* for repairable systems [2]. Knowing these indicators makes it possible to update the evolution of the failure rate during the lifetime of a machine. Updating the evolution period of this rate makes it possible to characterize the category of the failure type as well and to locate the faulty element(s) to optimize the criticality in *FMECA*, then to define an adequate maintenance policy. This article highlights the optimization impact of *RMA, ABC, FMECA* on the life of a boosting station "*K-101-A*" motor-compressor assembly at the Haoud-Berkaoui (*HBK*) production center of Sonatrach, based on Weibull-distribution law of two and three parameters and based on the history of failures and feedback.

2. Approach and methodology

The following methodology was adopted.

A. Quantitative study

Based on feedback, as currently practiced in institutions, through the implementation of a system of reporting adverse events, optimization could be made by the use of Pareto-diagram (*ABC*) method. The various operating times were recorded according to the machine's history file, exploiting the fault history during a limited period. They were classified in an ascending order. The distribution function of the probability associated with these data is calculated using empirical relations according to the size of data.

Table 2: Empirical relations by size of data [3]

Sample size	Formula	Cumulative frequency
$N \leq 30$	Median rank	$F_i = \dfrac{i - 0.3}{N + 0.4}$

The two procedures (code calculation, Simulink modelling) are used to find the matching values of the parameters β, η and γ of Weibull-distribution, which optimize the best available data. There are several estimation methods to perform this case study, accordingly to the two applied procedures. The graphical method (Weibull paper) is the basis of the calculation code and the analytical method (maximum likelihood) is the basis of the Simulink modelling.

To determine whether Weibull-distribution application is acceptable or not, the Kolmogorov-Smirnov test is performed. The KS test is used to determine if a sample has come from an assumed continuous probability distribution which consists of calculating the difference between the estimated $F(ti)$ empirical distribution function and the $F(t)$ theoretical one and takes the maximum of the differences in absolute value ($D_{n.max}$). This value is compared with the $D_{n.\alpha}$ limiting value corresponding to the level α of confidence which is obtained from the table of Kolmogorov-Smirnov test. If $D_{n.max} > D_{n\,.\alpha}$, the application is declined [3].

The graphical method: On the functional Allan Weibull paper, we represent the set of nodes $M_i(t_i,\ F(t_i))$, where t_i represents the time (here it is the time between failures, *TBF*) and $F(t_i)$ is the frequency estimated by the middle ranks. The Weibull functional paper makes possible to find the two parameters β and η [4]. The distribution function associated with a Weibull-law with the parameters β and η ($\gamma = 0$) is defined by:

$$F(t) = 1 - e^{-\left(\frac{t}{\eta}\right)^{\beta}}. \tag{1}$$

Fitting of the parameters of the Weibull distribution to data can be visually done using the Weibull plot (*Fig. 1*): on this plot the observed data must be laid along a straight line. This Weibull line is determined by the used calculation code.

The maximum likelihood method: In this method, a system of maximum likelihood function equations with three parameters of Weibull-distribution is established in the first step. Then an adaptive Simulink model is used to solve the equations, which cannot overcome in all cases the limitations of the traditional numerical methods as its efficiency is low [5]. The three-parameter Weibull distribution model is expressed by the following probability density function:

$$f(t) = \frac{m}{\eta}\left(\frac{t-\gamma}{\eta}\right)^{m-1} \cdot \exp\left(-\left(\frac{t-\gamma}{\eta}\right)^m\right),\tag{2}$$

where: m is the shape parameter ($m > 0$); η is the scale parameter ($\eta > 0$), γ is the position parameter. If we randomly select n dates of an object failures whose lifetime obeys to the three-parameter Weibull-distribution, the time of failures are $t_1 \leq t_2 \leq \ \leq t_n$.
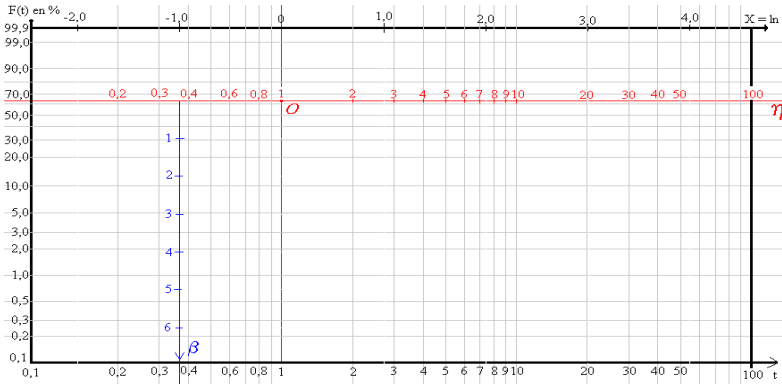
Figure 1: Weibull paper

The associated likelihood function is expressed as a probability density function [6]:

$$L(m,\gamma,\eta) = \prod_{i=1}^{n} f(t_i,m,\gamma,\eta) = \prod_{i=1}^{n}\frac{dR(t_i,m,\gamma,\eta)}{dt}.\tag{3}$$

The distributed log-likelihood functions are [7], [8]:

$$\ln L(t; m,\eta,\gamma) = n(\ln m - \ln \eta) + (m-1)\sum_{i=1}^{n}\ln\left(\frac{t_i-\gamma}{\eta}\right) - \sum_{i=1}^{n}\left(\frac{t_i-\gamma}{\eta}\right)^m.\tag{4}$$

Searching separately $\frac{\partial \ln L}{\partial m}, \frac{\partial \ln L}{\partial \gamma}, \frac{\partial \ln L}{\partial \eta}$, and after finishing, the log-likelihood equation is [7][8]:

$$\frac{1}{m} - \frac{\sum_{i=1}^{n}(t_i-\gamma)^m \ln(t_i-\gamma)}{\sum_{i=1}^{n}(t_i-\gamma)^m} + \frac{1}{n}\sum_{i=1}^{n}\ln(t_i-\gamma) = 0,\tag{5}$$

$$\frac{m-1}{m}\sum_{i=1}^{n}\frac{1}{t_i-\gamma} - \frac{n\sum_{i=1}^{n}(t_i-\gamma)^{m-1}}{\sum_{i=1}^{n}(t_i-\gamma)^m} = 0,\tag{6}$$

$$\eta^m = \frac{1}{n}\sum_{i=1}^{n}(t_i-\gamma)^m.\tag{7}$$

We use *EMV* in Simulink for the Weibull three-parameter distribution. Using its graphical modeling capabilities, the equations are drawn in the Simulink model window [7], [8]. The estimation of the parameters can be carried out without programming, so handling the Weibull distribution with three-parameters using the *EMV* solution becomes simple and automatic.

Meaning of the parameters: According to the existing criteria of evaluation of the optimization of maintenance in the industrial world, one distinguishes three major criteria, which are *cost*, *security*, *availability*.

The concept of *availability* implies three other notions showing the interaction between them. The D_o operational availability for an object is related to the ability to be repaired. It reflects the effectiveness of its maintenance and it can be determined as follows: *MTBF / (MTBF + MTTR)* [10].
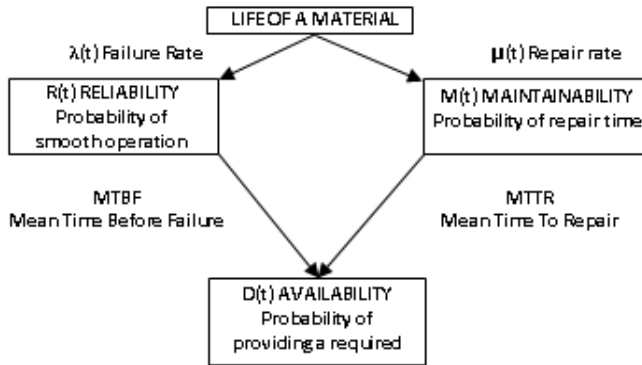
Figure 2: RMA interaction and lifetime of equipment [9]

Parameter analysis: The shape parameter gives the appearance of the distribution of failures $\lambda(t)$. It is dimensionless. Thanks to the estimated value of the form parameter β, one can model the characteristics of the different phases of the lifetime of an object.

B. Qualitative Study

According to the history of the machine, we rely on feedback from all operators, which can add value to the analysis. During a limited period the various information obtained are recorded, with a view to updating and ensuring the validity of all the information useful to the study. One of the most used criteria for categorizing failures is the lifetime of the object at the moment of the failure.
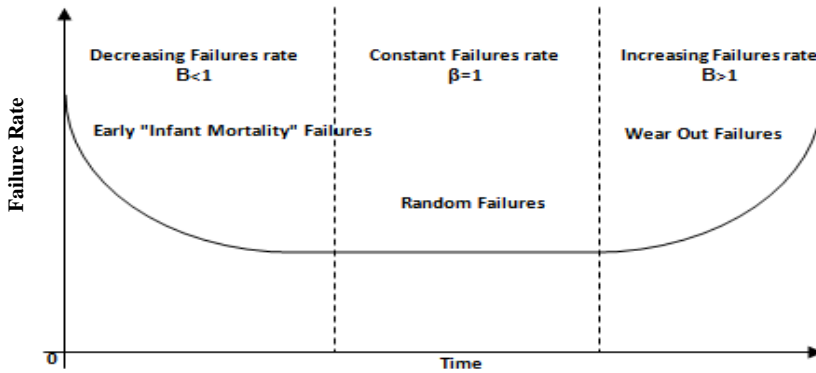
Figure 3: Allure of a failure rate in "bathtub" [11]

Meaning of breakdowns: The operation of the developed algorithm counting the number and the nature of the failures is schematized in a simplified way on *Fig. 4*. This algorithm is applied for each machine choosing from the list of all failures those in which it is affected by that failure [12].
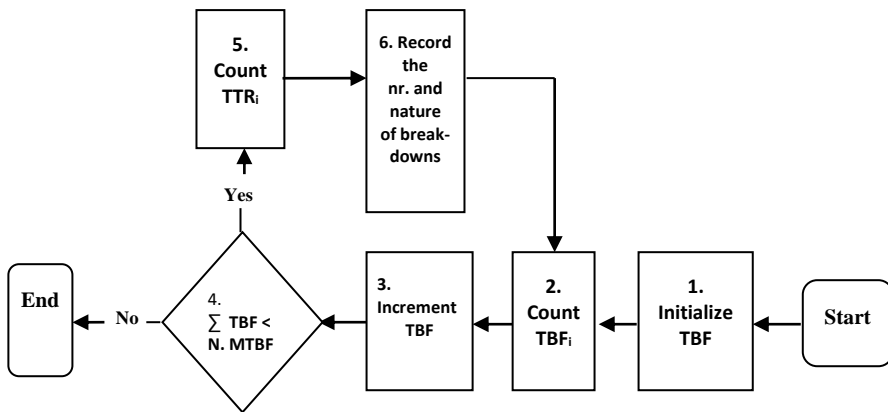
Figure 4: Logical algorithm counting the "Number and Nature" of failures [12]

Failure analysis: The first objective is to insert the fault in the working machine at the exact position where it appeared (*Fig. 5*).

The classification of the equipment is accordingly to the previously detailed criteria; we can summarize them by the criterion *G* (*gravity*), criterion *F* (*occurrence*), criterion *D* (*not detected*) criterion *C* (*criticality*). This analysis will help determine the most critical equipment by using *C=F·G·D* [14].
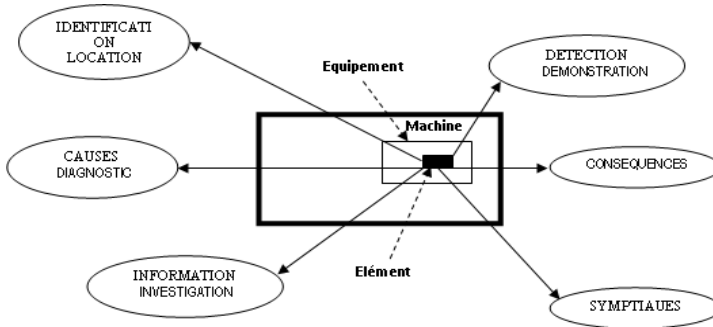
Figure 5: The criteria for inserting a fault in the machine [13]

The second objective is to determine the period T of the systematic intervention. In this policy the Kelly criterion is used in determining the optimal T which corresponds to the optimal period of the systematic intervention. For this it is necessary to know the cost of the reparations C_c (which is, by hypothesis, equal to the cost of failure), the cost of the preventive maintenace C_p and the parameters of the Weibull-distribution (β and η). We admit $r = C_c / C_p$ as the economic criticality ratio of the failure. The range of its validity is $2 < r < 100$ [15]. On the chart (*Fig. 6*)

$$x = \frac{T_0}{\eta} . \tag{8}$$
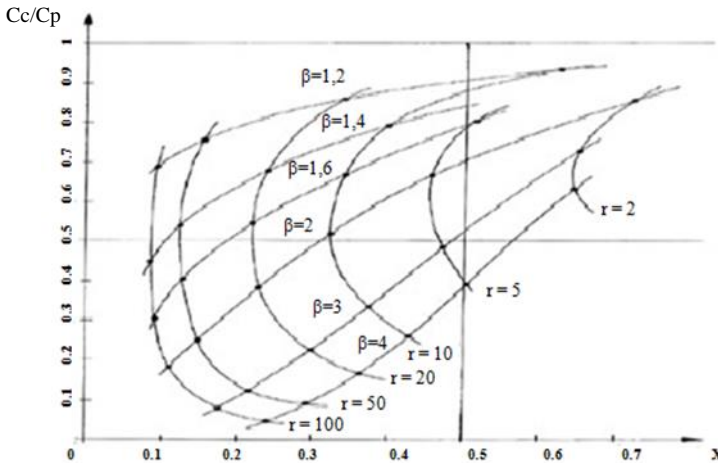
Figure 6: Kelly's abacus

C. Approach

The concept of integrated maintenance relies on the exchange and interaction between these actions, synthetized in three main steps (*Fig. 7*).
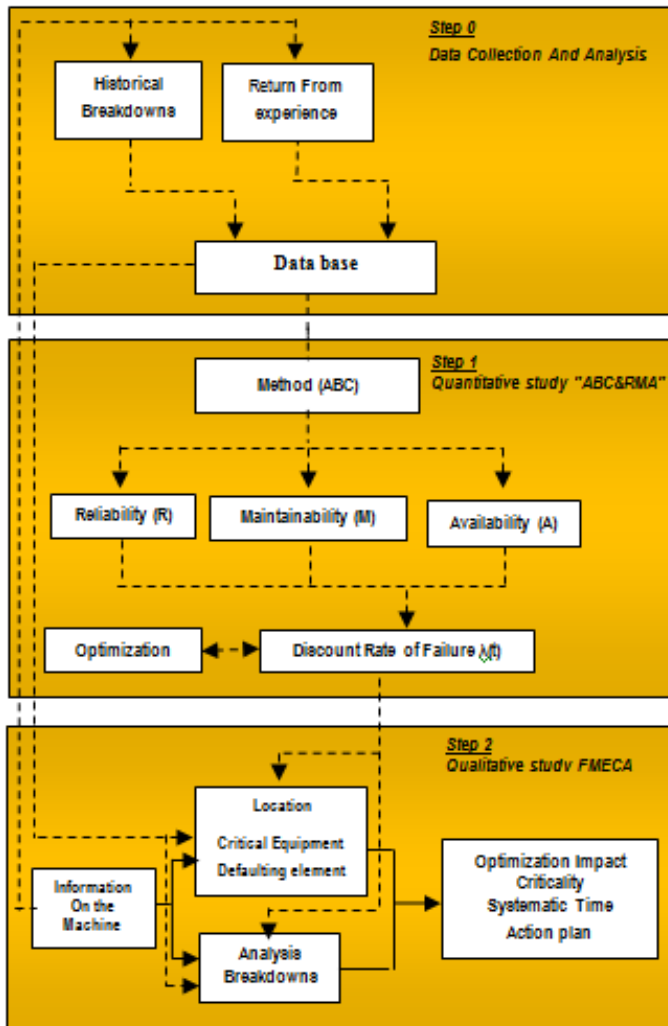
Figure 7: Global approach.

It is particularly important to note that the quantitative study of *RMA* is generally modeled within the algorithm integrated in the step (*1*).
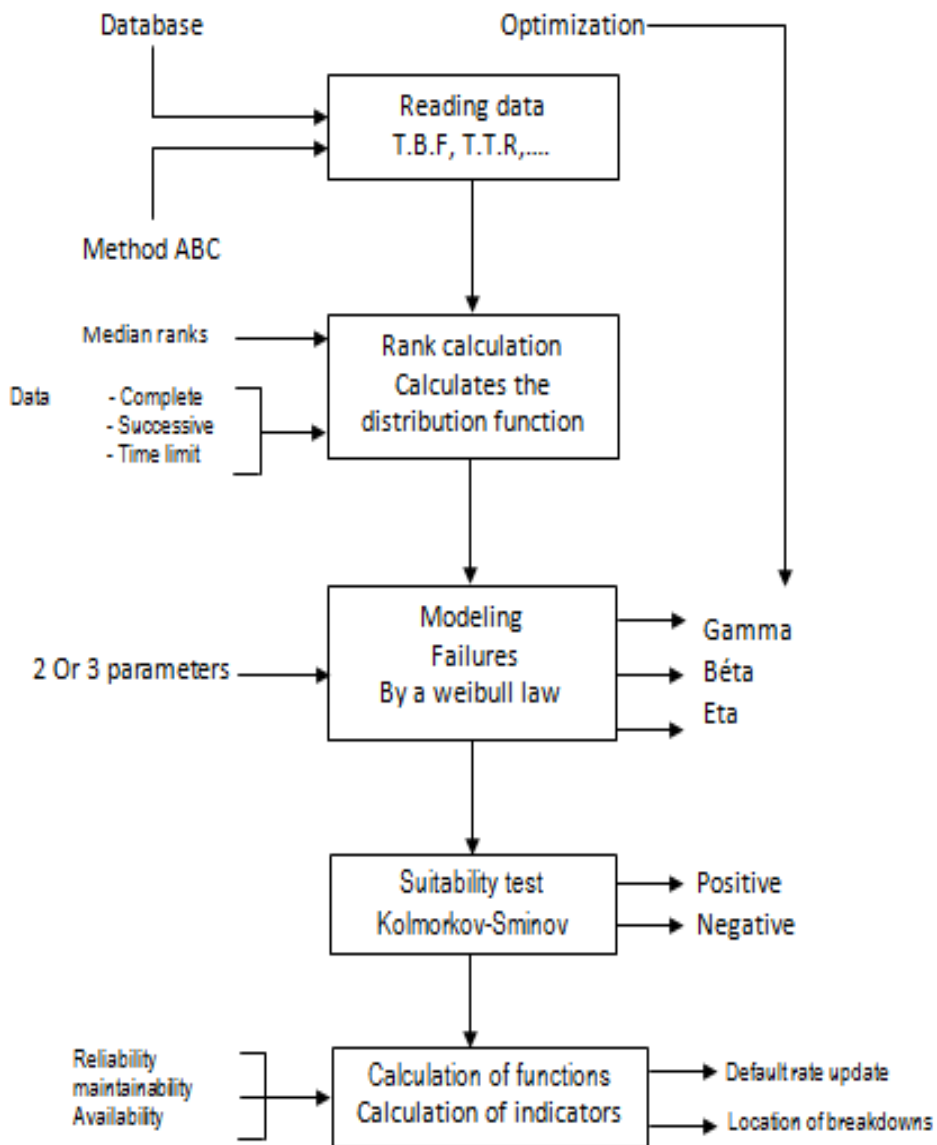
Figure 8: Algorithm of optimization in the quantitative study RMA
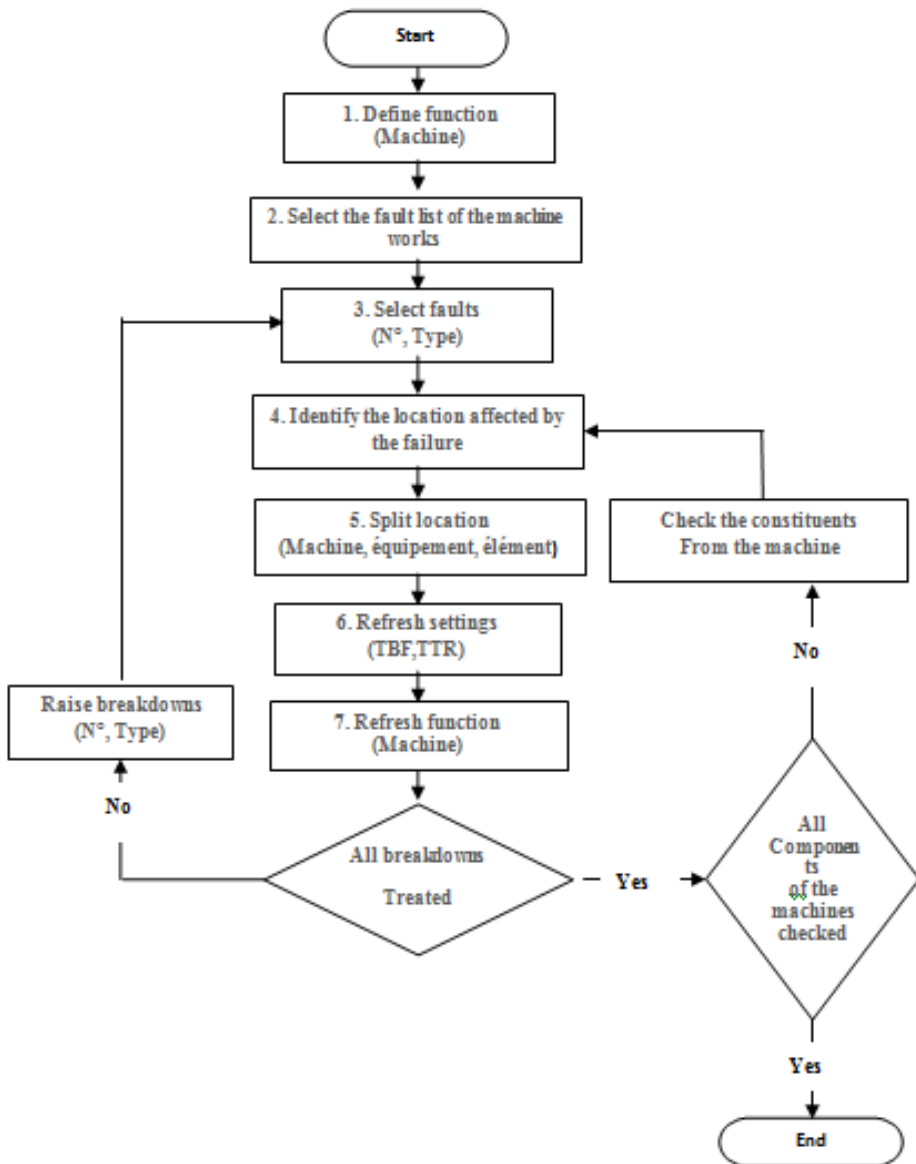
Figure 9: Organizational chart of the optimization procedure strategy

A preliminary optimization phase is necessary.

3. Case study: Booster "*K101-A*" Motor-Compressor of "*HBK / Sonatrach ALGERIA*"

The station aims to recover the flared gas in a quantity of 1042000 m^3/d in order to ship it to the gas treatment unit.
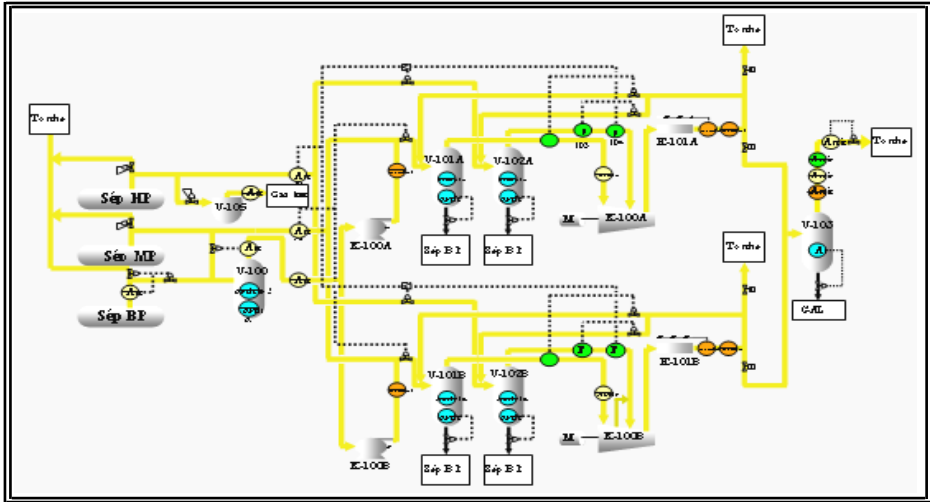
Figure 10: Process diagram of HBK Boosting Station

It usually consists of suction flasks, two motor compressors, a cooling system and a starting flask to recover condensates. *HBK* booster motors (*A* and *B*) are of the centrifugal type and driven by electric motors [17].

A. Quantitative and qualitative study

This study is based on the number of breakdowns to each equipment during the period between 1994 and 2004. The *ABC* curve is used to select the elements to be considered in our study. It is used to rank the equipment in an order of priority.

Table 3: Overall ranking of elements [18]

Designations	N°order	Nbr failures	plurality	Failure (%)
Lubricant Circuit /Compressor	1	04	04	18.18
Alignment Tree /Compressor	2	02	06	27.27
Pallier / Motor	3	03	09	40.90
Water Sealing Circuit /Compressor	4	02	11	50
Alignment Tree / Motor	5	01	12	54.54
Transformer of Start / Motor	6	01	13	59.09
Pallier / Multiplier	7	02	15	68.18
Regulatory chain Vibration / Compressor	8	02	17	7.27
Power Panel / Motor	9	02	19	86.36
Lubricant Pump /Multiplier	10	01	20	90.90
Antipump loop /Compressor	11	01	21	95.45
Transmitter Temperature / Multiplier	12	01	22	100
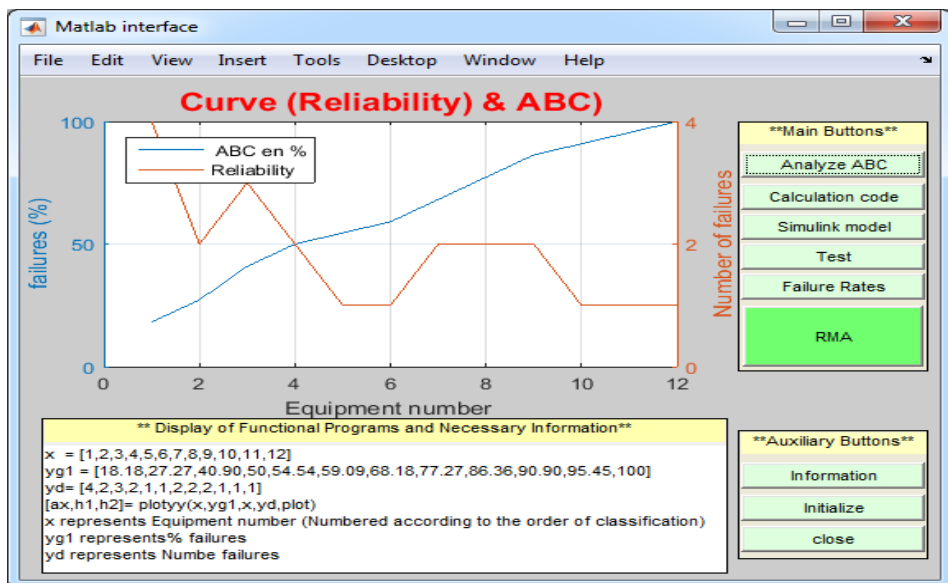
Figure 11: Curves (Reliability & ABC)

Zone *A*: 25% of equipment, representing 50 to 70% of the numbers of failure. They are therefore to be studied in priority the compressor.

It is concluded from the analysis made above that the equipment requiring support for its maintenance is the compressor; it is the most critical equipment.

Table 4: Preparation of the application data

$N°$	TTR(h:m)	TBF(h:m)	$F_{estimated}$	$TBF×(1/150)$	$F(\%)$
1	14:30	22:40	0.0614	0.149	6.14
2	16	1681	0.1491	11.20	14.91
3	17:30	1971:30	0.2368	13.14	23.68
4	18	2510	0.3245	16.73	32.45
5	18:30	2522	0.4122	16.81	41.22
6	23	4030:10	0.5	26.86	50
7	24	4213	0.5877	28.08	58.77
8	48	5110	0.6754	34.06	67.54
9	54	5685:10	0.7681	37.90	76.81
10	56	5712	0.8508	38.08	85.08
11	56:30	6984	0.9385	46.56	93.85

Two parameters: The graphical determination of the parameters through the Weibull paper which has been validated by a calculation code.
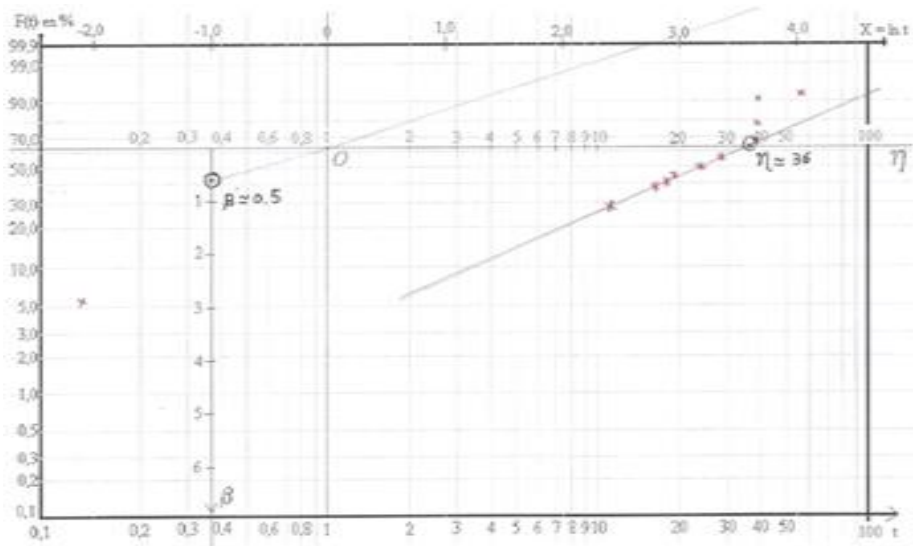
Figure 12: Weibull paper
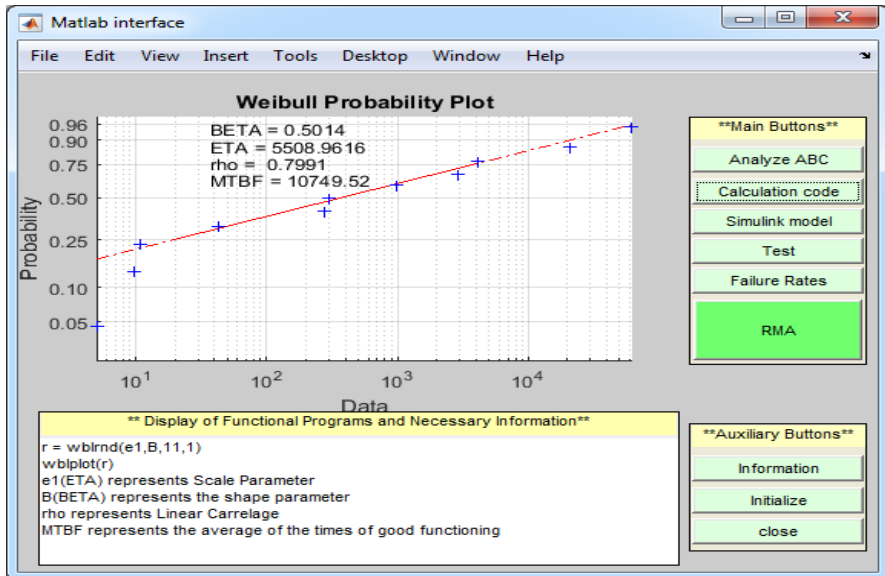
Figure 13: Weibull probability plot (calculation code)

It makes possible to find the critical hints of failure of the analyzed equipment:

$\beta = 0.50$; $\gamma = 0$; $\eta = 5509$.

Three parameters: the *EMV* will be implemented in a Simulink-model.
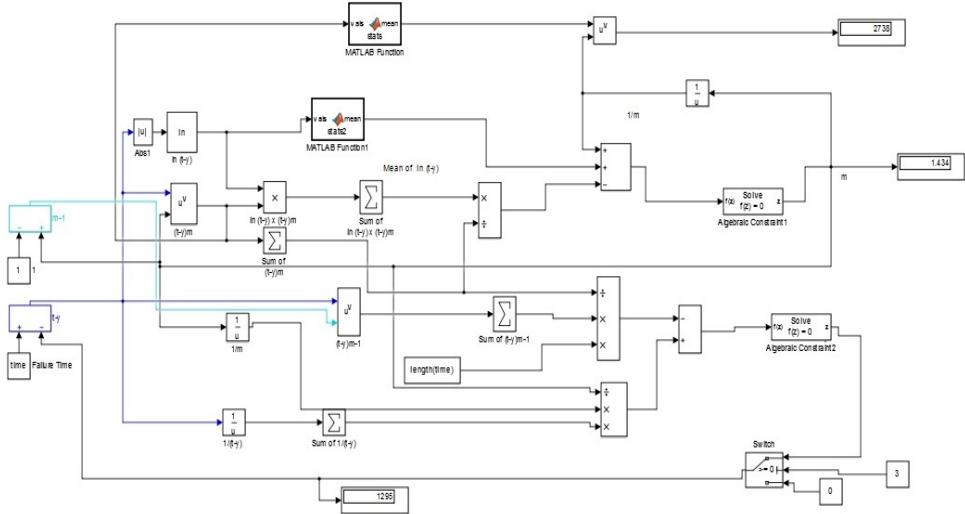
Figure 14: EMV Simulink model, $\beta = 1.434$; $\gamma = 1295$; $\eta = 2738$

Analysis and meaning: we have to test the Weibull model.
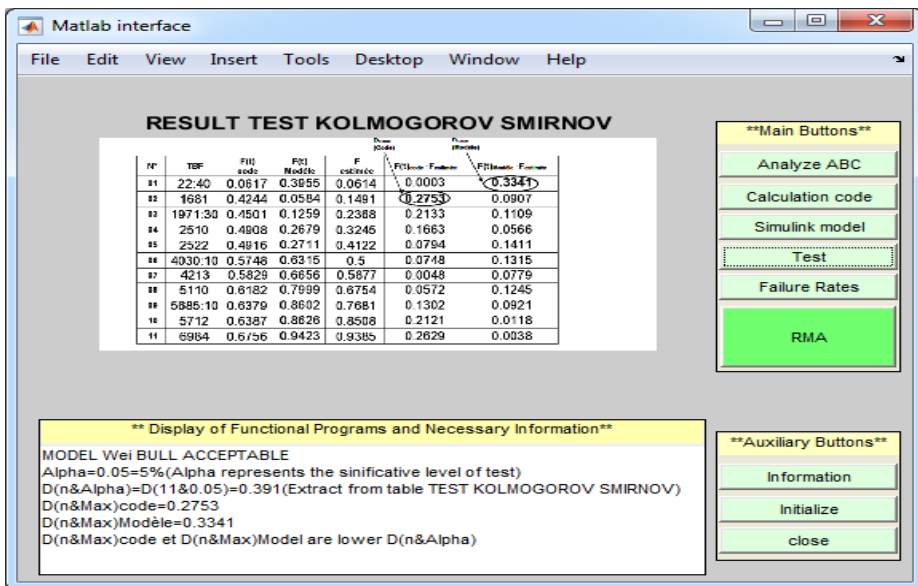
Figure 15: Kolmogorov-Smirnov test

Updating the evolution of the failure rate gives two different age scales:
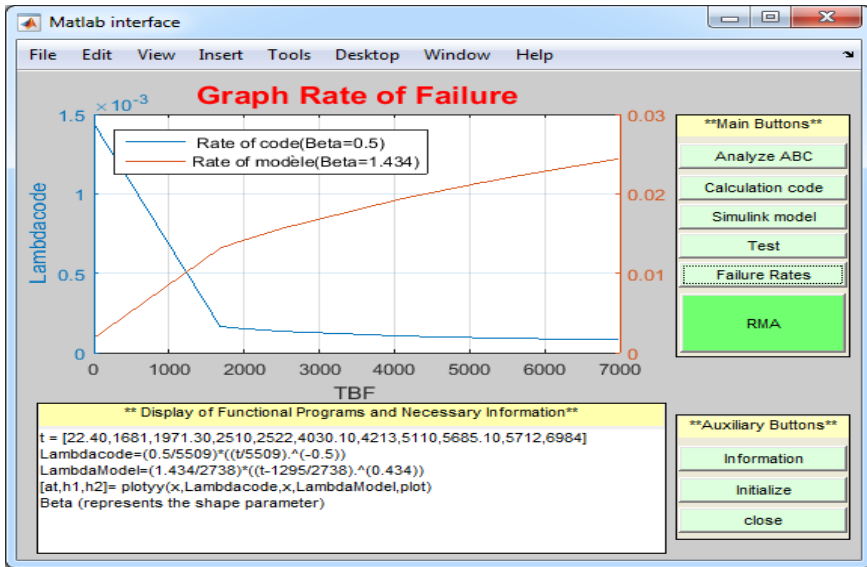
Figure 16: Allures of the rate of failure

The period of youth ($\beta = 0.50$) and the period of wear "old age" ($\beta = 1.434$).
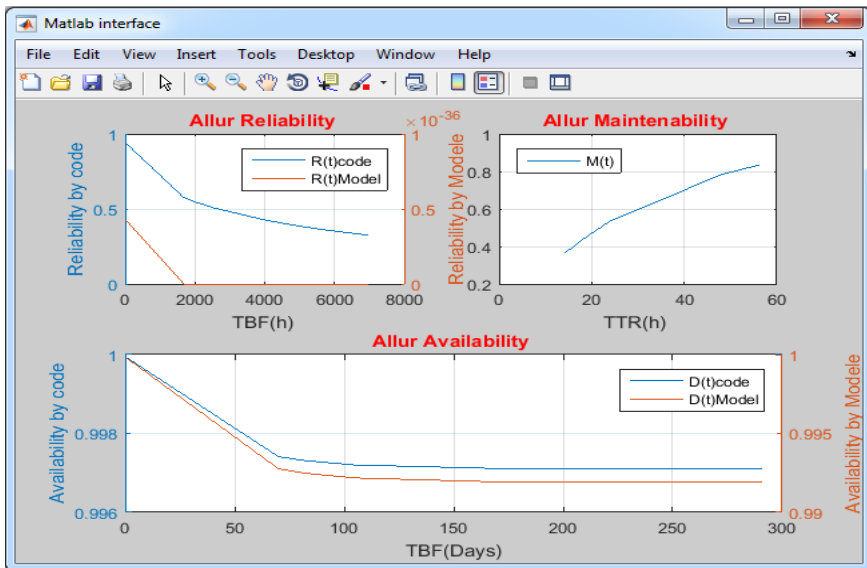
Figure 17: Allures RMA

The results obtained after the calculation are according to the equations:

$$M(t) = 1 - e^{\mu \cdot t}, \ \ R(t) = e^{-\left[\frac{t-\gamma}{\eta}\right]^{\beta}}, \ \ D(t) = \frac{\mu}{\lambda + \mu} + \frac{\lambda}{\lambda + \mu} \cdot e^{-(\mu+\lambda)\cdot t}, \tag{9}$$

which allows to draw the above allure of *RMA* for the two procedures: $\beta = 0.50$, $\beta = 1.434$.

Reliability, between the two procedures there is almost a difference of 0.5 (50%) from the beginning to the end of the phase which directly affects the cost of the maintenance (repairs).

Maintainability, shows that the two procedures ensure a direct proportionality between *TTR* and *M(t)* which directly affects the security maintenance.

Availability, in the beginning *TBF* 0 to 70 days, the two procedures shows a rapid regression but from 70 to 290 days there is a constant availability with a difference of approximately 0.05 (5%): D_o (code) = 0.96, D_o (model) = 0.91. The criteria of optimization gives:

Table 5: Optimization criteria

Procedures	Cost	security	Availability
Calcul Code	less	critical	more
Simulink Model	more	critical	less

According to the criteria of criticality in this phase of aging $\beta = 1.434$.

Table 6: Determination of criticality

failures	N^bre/TBF	Nature	Integration	criticality
Labyrinth seals	04/11275	Break/fissure	Lubricant circuit	8
Gasket of sealing	02/4203	Wear	Water circuit	20
Mechanical Garnish	02/11197	Break/fissure	Chain of vibration	12
Bearing	02/7656	Deformation	Alignment shaft	18

The model of Kelly to determine the optimum time of intervention based on the direct and indirect cost of maintenance.

Table 7: Corrective and preventive maintenance costs "gasket sealing"

Cost	C_c(DA)	C_p(DA)
Corrective	67960	/
Preventive	/	211820

By using the abacus of Kelly, for $r = 3$ and $\beta = 1.434$ we extract the value $x = 0.6$ which requires the optimal time of systematic intervention equal to $T_o = 1643$. Action plan, the obtained strategy of maintenance is required and adopted by *FMECA*.

FMECA : ANALYSIS OF FAILURE MODES OF THEIR EFFECTS AND THEIR CRITICITIES										
Machine: motorcycle compressor Equipment: Compressor	Dated:									
The element	function	Failure mode	causes	effects	detection	criticality				Action to engage (Maintenance type)
						F	G	D	C	
gasket of sealing	Ensure of sealing	Usury	Tired	overheating	Oil leak	5	4	1	20	Verification and Change (Corrective & Preventive)
bearing	Keep the rotor position	Deformation	Tired	Bad rotation Rotor	Visual	3	3	2	18	Change of bearing (Corrective)
Mechanical Garnish	Ensure of sealing	- Break - fissure	Tired	overheating	Oil leak	4	3	1	12	Change (corrective)
Labyrinth seals	Reduce gas leaks	- Break - fissure	- Corrosion - overloading	Increased gas leak	Low flow and gas pressure	4	2	1	8	Treatment and replacement of seals (Corrective & Preventive)

3. Conclusion

In this article it is shown the impact of the optimization of the integrated maintenance on the strategic machine lifetime. The approach is based on two qualitative analysis ABC, RMA, and the quantitative FMECA. In this approach, the two procedures are presented as code calculation and Simulink model by the use of Weibull-distribution law. The first one, namely the graphical method via Weibull-distribution, has two parameters ($\beta = 0.50, \eta = 5509$) and the second is based on the maximum likelihood method (EMV) with a Weibull-distribution with three parameters ($\beta = 1.434, \gamma = 1295, \eta = 2738$). MATLAB software is used in the both procedures, both in programming and Simulink modelling. The implementation of such approach demonstrates its contribution to maintaining machine lifetime. Indeed, it permitts a better estimation of the operational availability of the studied machine, resulting D_0 (code) = 0.96, and D_0 (model) = 0.91. The criticality of 20 identifies the critical element on which a particular attention is to be applied by the optimal time for systematic

intervention of 1643 hours. Briefly, the approach has constituted an actual way to the optimization of the actions of the maintenance.

References

[1]   Mebarkia, D., "Search for an optimal solution for the operation and maintenance of Algerian pipelines taking into account the reliability of the equipment of the different lines", Magister thesis, Reliability Laboratory of Equipment and Materials, Faculty of Hydrocarbons and Chemistry, University of Boumerdes, Joins 2013.

[2]   Marc, T., "Predictive maintenance reliability and vibration of machines", University Presses of Québec, 2012.

[3]   Meslameni, W., "Optimization of maintenance times of a gas turbine Optimisation des temps de maintenance d'une turbine à gaz", *International Journal of Applied Research and Technology*, vol 1, 2018.

[4]   Homeomath, Papier de Weibull, "http://homeomath2.imingo.net/loiweibull2.htm".

[5]   Yang, M., Nie, H., "Advanced Algorithm for Maximum Likelihood Estimation of Three Parameter Weibull Distribution", *Journal of Nanjing University of Aeronautics& Astronautics*, 39(1), pp. 22-25, 2007.

[6]   Mfetoum, I. M., Essiane, S. N., "Estimation of Weibull model parameters: application to the modeling of the reliability of the CAMRAIL railway ballast mechanical tapping machine", *Journal of Science, Technology and Development*, Special Edition, pp. 117-121, July 2016.

[7]   Shi, J. Z., Shao, R., Chen, X., "Weibull distribution based on Matlab / Simulink Maximum likelihood estimation", *Journal of Henan Science*, Vol.29, 1004-3918, 2011.

[8]   Shi, J. Z., et al., "Random Censored Data MLE of Weibull Distribution Based on Simulink", *Advanced Materials Research*, Vols. 542-543, pp. 1463-1466, 2012.

[9]   Celeux, G., Corset, F., Lannoy, A., Ricard, B., "Designing a bayesian network for preventive maintenance from expert opinions in a rapid and reliable way", *Reliability Engineering and System Safety*, vol. 91(7), pp. 849-856, 2006.

[10]   Bensaci, M. A., "Management of a maintenance integrated into the centrifugal compressor motorcycle k 101-A", Magister thesis, Electromechanical Systems Research Laboratory, Department of Electromechanics, Annaba University, 2006.

[11]   Harish, K. N. S., Choudhary, R. P., Murthy, Ch. S. N., "Failure Rate Analysis of Shovel and Dumper in Opencast Limestone Mine using RWB and ANN", *International Journal of Innovative Technology and Exploring Engineering (IJITEE)*, vol. 8, Issue 5, March, 2019.

[12]   Samir, H., "Model of performance evaluation of a production line of a sequence of n distinct products on m machines with (ml) buffer stocks", MSc Thesis, Department of Mechanical Engineering Faculty of Science and Engineering, University Laval Quebec, 2012.

[13]   Bouanaka, M.L., "Contribution to the improvement of the operational performances of the industrial machines", Memory presented for the diploma of magister in mechanical engineering, Department of Mechanical Engineering, Faculty of Sciences of the Engineer, University of Constantine, 2008/2009.

[14]   Donier, L., Sansberro, D., Barthod, V., Clerget, E., Tissot, D., "AMDEC risk analysis of the preparation of doses to be administered by a dry oral forms automation", *International Journal of Science Direct*, Vol. 52, Issue 1, pp. e42-e43, March 2017.

[15]   Lyonnet, P., "The mathematical maintenance and methods", *4th edition, LAVOISIER*, October 2000.

[16] Fadhil, A., "A Comparison Between the Bayesian and the Classical Estimators of Weibull Distribution", *Journal of Kufa for Mathematics and Computer*, Vol.1, No.8, Dec 2013.

[17] Habbel, L., Boucetta, O., "Study and Maintenance of a Centrifugal Compressor", Final Thesis for Engineering Diploma, Faculty of Hydrocarbons and Chemistry, Department of Transport and Hydrocarbon Equipment, University Mohamed Bougara Boumerdes, 2006.

[18] Bensaci, M.A., "Historical Tables Breakdowns of a K-101A Motocompressor", Internship Report, Sonatrach in Division Production Branch Regional HUD Berkaoui Maintenance Division, 2006.

Study of Reliability in a Repairable System by Markov Chains

Naima TAMALOUSSI[1], Azzedine BOUZAOUIT[2]

[1] Department of Mechanical Engineering, Faculty of Technology, University of Skikda, Algeria,
e-mail: naimatamaloussi@yahoo.com
[2] Department of Mechanical Engineering, Faculty of Technology, LRPCSI Laboratory of
research, University of Skikda, Algeria, e-mail: bouzaouit21@gmail.com

Abstract: In the industrial sector, maintenance of production facilities plays an important role to carry out production by increasing the reliability and availability of the production process. Predictive maintenance strategy seems adequate to anticipate the failure and degradation of the state of such equipment. A reliability study is needed to quantify indicators to describe the functioning of any system over time. In this paper, we present the results of a stochastic modeling conducted on the analysis of the availability of motor-pump system, installed in a cooling circuit in an industrial complex. The equipment considered in this study is composed of four subsystems. The proposed model is a dynamic Markovian approach, for the purpose of a comparison with the analytical calculation in terms of the indicators' evaluation of the dependability of the studied system, including instant availability. The different states of the system components and the transition functions between these states have also been characterized. The results of availability obtained by the model are well correlated with those calculated analytically, confirming that the proposed model is very powerful, it will help predict the future states of the system, in order to predict any necessary preventive maintenance actions.

Keywords: Reliability, repairable system, Markov chain, modelling, transition matrix.

1. Introduction

The reliability of the various industrial achievements becomes an important issue at the economic, ecological and human levels. Technology is moving too fast, materials are becoming too complex for common sense to be enough to predict the risks [1], [2]. Stochastic processes such as the Markov processes are

used to model the evolution of a system in the course of time [3]. The quantification of these processes is carried out either by analytical calculations when that is possible, or using simulation of Assembles-Carlo, or with deterministic numerical algorithms [4]. These tools of quantification can be difficult to use for people not initiated with these methods, thus tools of assistance to modeling such as the Dynamic Bayesian Networks, the Boolean logic driven Markov processes BDMP, were developed. These tools are generally coupled with the calculation algorithms. The quantification of the systems to be modeled is assisted by an intuitive chart of the system.

For a whole reparable system, adequate models are required to ensure a good risk prediction, so to have a good performance of the system. This modeling is called stochastic modeling.

The stochastic modeling often relates to reparable systems. This approach is the base of the monitoring methods, diagnosis and maintenance.

For a reparable system, it is necessary to introduce another probabilistic concept: the availability $A(t)$ is the probability that the device functions at moment t [5].

For that, one can rely on the description of the different degradations states of the system until the failure. The passage from a state to another is done by transitions. These transitions are regarded as instantaneous in the Markov model [6]. A stochastic process is a whole of random variables $(X_T)_{T=0}$ with values in the whole of the observations. A process is Markovian if the transition probability of the future states depends on the present state but does not depend on the past states [7].

The stochastic processes are used in modeling systems of discrete nature, and more precisely to model the temporal evolution of the dynamic systems. Indeed, such systems generally evolve from one state to another, and what matters to the modeler is the characterization of these states changes. Both the discrete-time and the continuous-time Markov chains [8], are defined and characterized by their probabilities of transition from a state to another [9].

The Markov chains are a succession of random variables $(X_n, n \in N)$, where X_n represents the state of the system at moment n. The fundamental property of Markov chains known as property of Markov is that its future evolution depends on the past only through its current value. In other words, conditionally with X_n and X_{n+k} ($k \in N$) are independent. The applications of the Markov chains [10] are very numerous (networks, genetics of the populations, mathematical, stock management, stochastic algorithms of optimization, simulation).

We can then define the law of "probability of transition" from a state (i) towards another state (j) by:

$$P_{i,j} = P(X_n = j | X_{n-1} = i). \tag{1}$$

A system can be defined like a whole of interdependent components, designed to fulfill a given function, under conditions given at an interval of time [11].

For each system, it is important to clearly define the elements, which characterize it, namely: the function, the structure, the operating conditions and the environment in which it has to operate. The reliability of a system is expressed by the probability that this device achieves a necessary function under conditions of use for a period of time; it is thus a value ranging between 0 and 1. In the following we denote it by *R(t)*, where *t* indicates the duration of the mission.

$$R\,(t)\;=\;P\{lifespan\ of\ the\ system > t\}. \tag{2}$$

Let us recall that the lifespan of a system is a measure of the rendered quantity of service. According to the studied system, it is expressed in term of time, kilometers, or other.

The fact that the failure of a system can occur at any time brings us to consider this quantity as a random variable to which we can associate a function of density of probability *f(t)*. It is important to recall that *f(t)* is the probability that the lifespan of a system lies between *t* and *t + dt*, or the probability that it breaks down between *t* and *t + dt*.

$$f\,(t) \cdot dt\;=\;P\{t < lifespan\ of\ the\ system < t + dt\}. \tag{3}$$

The function of distribution or the function of distribution associated with the lifespan *F(t)*, can be interpreted as the probability that the system still functions at the moment *t*.

$$F(t) = P\{\,lifespan\ of\ the\ system \le t\}. \tag{4}$$

The failure of equipment can be characterized by a rate (λ) called failure rate. This rate is also called rate of chance or death rate. It is defined as being the conditional probability that the equipment breaks down between the moment *t* and $t + \Delta t$ knowing that it survived until the moment *t*. It can also be defined as the proportion of components having survived until the moment *t*. It also represents the speed of arrival of the breakdown [12].

$$\lambda(t) = \frac{N\,(t+\Delta t) - N\,(t)}{N\,(t)}, \tag{5}$$

with:

- $N\,(t)$: component count having survived until the moment *t*;
- $N\,(t+\Delta t)$: component count having survived until the moment $t+\Delta t$.

The increase in the complexity of a mechanical system makes its reliability to decrease, if one does not take compensatory measures. This system is formed of independent components that are to say in series. It is said that the system is without redundancy. The reliability of these systems worsens dramatically with the increase of the number of the components.

When reliability is studied, one is interested not only in the probability of breakdown, but also in the number of breakdowns in particular, in order to repair the system on time.

From this point of view, two new parameters of reliability become our center of interest. The availability by definition is very close to reliability, except that the required system must function at the moment (*t*) and not over a period of time (*0* to *t*).

For a system, with the assumption of a constant failure rate λ and of a constant repair rate μ, it is shown that the instantaneous availability is defined by (8):

$$\lambda \ = \ 1 \ / \ MTBF \tag{6}$$

$$\mu \ = \ 1 \ / \ MTTR, \tag{7}$$

with:
MTBF: Mean time between failures;
MTTR: Mean time to restore.

The traditional instantaneous availability of the equipment is given by the following equation:

$$A(t) \ = \frac{\mu}{(\lambda + \mu)} + \frac{\lambda}{\lambda + \mu} e^{-(\lambda + \mu)t}. \tag{8}$$

When λ and μ are independent of time, and when *t* becomes large, one notes that *A(t)* tends towards a constant value. This value is often called asymptotic availability. It is equal to:

$$A_\infty = \frac{1}{1 + \lambda/\mu}. \tag{9}$$

The determination of *A(t)* will be done starting from the estimate of the reliability parameters. By analogy with reliability, it is possible to give to maintainability a probabilistic definition: "maintainability is the probability of restoring a system under specified operating conditions, in wished limits of time, when maintenance is accomplished under conditions and with prescribed means" [12].

The maintainability index (*M*) is the probability that a device is repaired before time *t*:

$$M(t) = 1 - e^{-\mu t} \tag{10}$$

$$MTTR \ = \ \Sigma TR \ / \ N \tag{11}$$

MTTR: Mean time to repair;
$\sum TR$: Total repair time.

2. Methodology of work

We present in our study the case of a continuous process of feeding a boiler which feeds a steam turbine, which functions without interruption. The machine, which ensures the correct operation of this system, is a group motor-driven pump HPT 28-20, as can be seen in *Fig. 1*.

Figure 1: General view of the pump HPT 28-20 m 8 floors

We note that the group is made up of the following elements:

- an electric motor;
- a reducing coupler;
- a nourricier pump;
- a feeder pump.

A. Determination of the reliability characteristics

The machine history of failures and their times duration are summarized and given by *Table 1*.

I. Calculation of the failure rate (λ)

To calculate the failure rate λ, we must calculate first the *MTBF* (Mean time between failure, equal: the sum of *TBF* on *N*). In our case, the sum of *TBF* is 29304 hours and *N* is equal to 30. Then we can calculate λ (see (6)), *TBF* values are given in *Table 1*.

II. Calculation of the repair rate (μ)

To calculate the rate of repair μ one must initially calculate the *MTTR* (Mean time to repair, equal: the sum of *TTR* on *N*). In our case, the sum of the *TTR* is 172 hours and *N* is equal to 30. Then one can calculate μ (see (7)). The values of *TTR* are given in *Table 1*.

Table 1: Duration of good operation (TBF), and repair (TTR) of the feeder pump

N°	TTR(h)	TTF(h)	TBF(h)	N°	TTR(h)	TTF(h)	TBF(h)
1	04	24	20	16	08	1104	1096
2	08	1056	1048	17	08	600	592
3	08	4296	4288	18	04	432	428
4	18	1032	1014	19	04	912	908
5	04	1896	1892	20	04	600	596
6	08	168	160	21	18	576	558
7	18	1776	1758	22	04	72	68
8	01	648	647	23	15	672	457
9	08	1344	1336	24	04	432	428
10	08	1104	1096	25	01	312	311
11	18	96	78	26	09	624	615
12	16	3456	3440	27	08	336	328
13	18	1704	1686	28	16	456	440
14	08	1632	1624	29	16	96	80
15	04	1272	1268	30	10	5520	5510

The notation used in *Table 1* is:
TTR: total repair time;
TTF: total operating time;
TBF: running time.

B. Markov chain of the studied system

This method results from a mathematical theory. One has a whole of states of components, which, combined, makes it possible to define the whole of the states of the system. This system is divided into two subsets:
- operating condition;
- state of breakdown.

One models the process like two subsystems (*S1*, *S2*) "in series" (Sealing system - valve of safety). The breakdown of one of the two systems causes the breakdown of the system.

The Markov chain of the system is represented in *Fig. 2*.
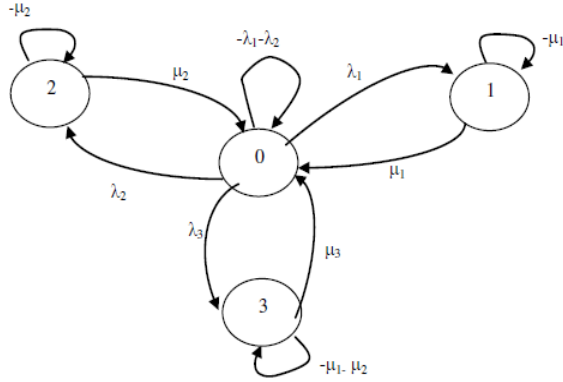
Figure 2: Markov graphical model of the system

The exponential law is selected to model the probability of failure of the feeder pump. The states of the system must be defined first. In the case of N "binary" components, we get a maximum number of 2^N states [13]. Then, it is necessary to count all the possible "transitions" between the various states from the system by identifying their causes. In our case $N = 2$ thus the number of states is $2^2 = 4$:

- State 0: *S1*, *S2* subsystems function;
- State 1: *S1* subsystem is broken down;
- State 2: *S2* subsystem is broken down;
- State 3: subsystems *S1*, *S2* are broken down,

with:

S1: subsystem 1 (sealing system);
S2: subsystem 2 (valve of safety).

The associated equation of states is then:

$$P'_0(t) = -2(\lambda_1 + \lambda_2)P_0(t) + \mu_1 P_1(t) + \mu_2 P_2(t) + (\mu_1 + \mu_2)P_3(t) \quad (12)$$

$$P'_1(t) = \lambda_1 P_0(t) - \mu_1 P_1(t) \quad (13)$$

$$P'_2(t) = \lambda_2 P_0(t) - \mu_2 P_2(t) \quad (14)$$

$$P'_3(t) = (\lambda_1 + \lambda_2) P_0(t) - (\mu_1 + \mu_2)P_3(t) \quad (15)$$

$$A(S) = P_0 \cdot (SI - M)^{-1} \quad (16)$$

P_0: Vector of initial conditions, $P_0 = [1\ 0\ 0\ 0]$;
P_1: Probability of state 1;
S: Laplace variable;
M: Transition matrix;

I: Identity matrix, $I = \begin{bmatrix} 1 & 0 & 0 & 0 \\ 0 & 1 & 0 & 0 \\ 0 & 0 & 1 & 0 \\ 0 & 0 & 0 & 1 \end{bmatrix}$.

The transition matrix M combines the graph:

$$M = \begin{bmatrix} -4\lambda & \lambda & \lambda & 2\lambda \\ \mu & -\mu & 0 & 0 \\ \mu & 0 & -\mu & 0 \\ 2\mu & 0 & 0 & -2\mu \end{bmatrix}. \tag{17}$$

Put: $\lambda_1=\lambda_2=\lambda_3=\lambda$, $\mu_1=\mu_2=\mu_3=\mu$.

The solution is based directly on the Laplace transform so the equation (16) becomes:

$$A(S) = P_0 \cdot \begin{bmatrix} S+4\lambda & -\lambda & -\lambda & -2\lambda \\ -\mu & S+\mu & 0 & 0 \\ -\mu & 0 & S+\mu & 0 \\ -2\mu & 0 & 0 & S+2\mu \end{bmatrix}^{-1}. \tag{18}$$

The following model shows the availability of the system:

$$A(s) = \frac{S^2+3\mu\,S+2\mu^2}{S^3+(4\lambda+3\mu)S^2+(6\lambda\mu+2\mu^2)S} \cdot \tag{19}$$

By returning to the time domain:

$$A(t) = \frac{\mu}{3\,\lambda+\mu} + \frac{6\lambda(16\,\lambda^2+\mu^2)}{2(3\lambda+\mu)(16\,\lambda^2+\mu^2)} \cdot e^{-\left(2\lambda+\frac{3\mu}{2}-\frac{1}{2}\sqrt{(16\,\lambda^2+\mu^2)}\right)t}. \tag{20}$$

3. Results and discussion

We have all the parameters necessary to plot the curves for the reliability and maintainability functions. They are represented respectively by *Fig. 3* and *Fig. 4*.
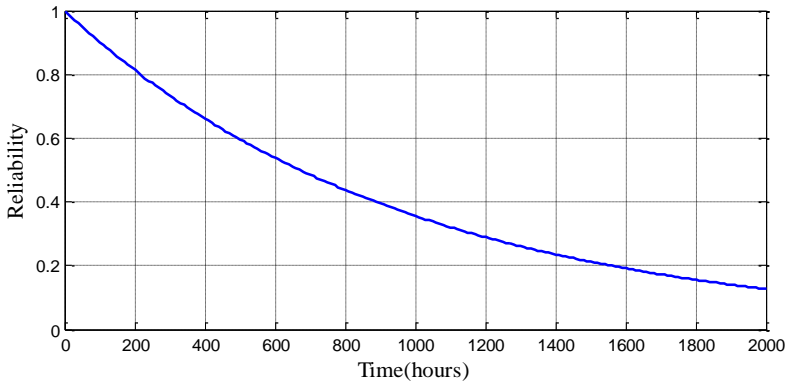
Figure 3: Curve of reliability

According to *Fig. 3*, which represents the reliability of the system, one can see clearly that for an average time of operation (*MTBF* = 976.8 h), the reliability is about 37 %. This percentage of reliability is considered to be low, which can be interpreted as the absence of a regular maintenance program.
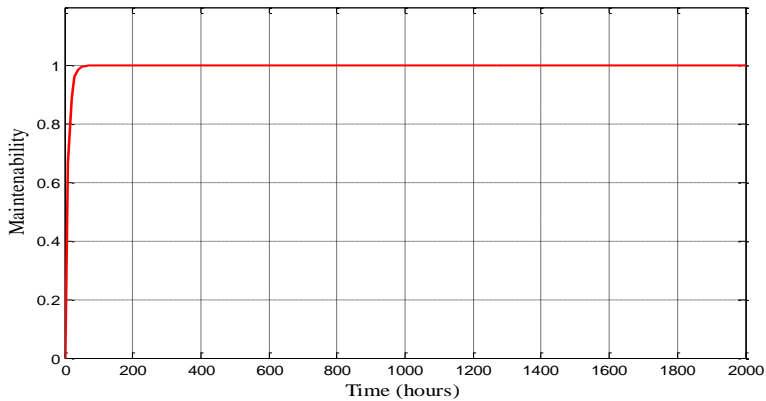
Figure 4: Curve of maintainability.

The maintainability of the motor-driven pump is represented in *Fig. 4*. According to this curve, one can see clearly that maintainability increases abruptly and reaches significant values in a very short time, the only interpretation of this being that the equipment encounters several technical problems, which require the stops to repair them.

The availability is represented by *Fig. 5*.
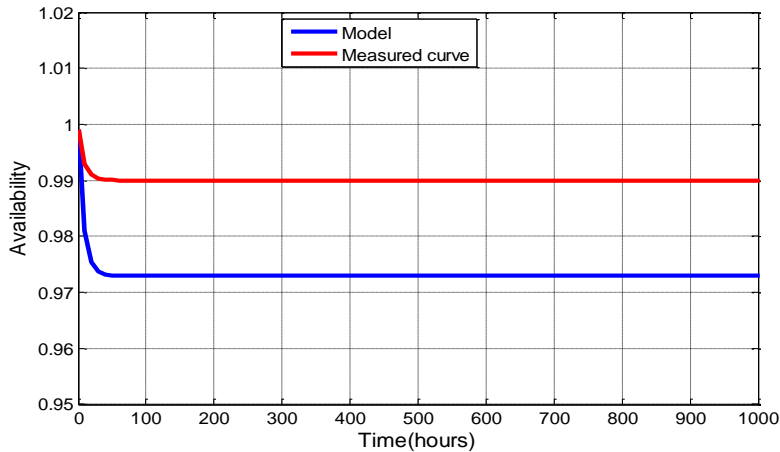
Figure 5: Curve of availability

Fig. 5 represents the availability of the system, according to analytical computations based on the *MTBF* and according to the Markov model proposed; one can observe that the computed values and the model availability are well correlated. The coefficient of correlation is of the order (R=0.996) this value confirms that the suggested Markov model is very powerful, and will contribute to the future prediction of the state of the motor-driven pump without waiting the breakdown. According to the objectives of the maintenance service (the availability of the system), and based on the proposed model, we can foresee the time necessary to schedule a preventive maintenance action.

4. Conclusion

Industrial systems are becoming complex and associated maintenance is becoming more expensive. Maintenance strategies are at the heart of this concern. These need to have reliability indicators, specific to each system that can be measured or modeled to trigger conditional preventive maintenance actions. On the other hand, predictive maintenance consists of using models to predict the reliability of the components of such a system, with the aim of increasing its availability through the implementation of anticipated interventions, in order to reduce the time required for maintenance. In this context, stochastic models of degradation are mathematical models that describe the degradation of a system over time. This degradation often leads to a decrease in the performance of the production system. Markov model is often used when evaluating the availability

of repairable systems, based on the principle of changing the state of one component to another with the characterization of the transition between these states.

The proposed model is a dynamic Markov model approach, for the purpose of a comparison with the analytical calculation in terms of evaluation of availability indicator of the studied system. The different states of system components as well as the transition functions between these states have also been characterized. The proposed model adequately describes the instantaneous availability required for the future states prediction of the studied system, and consequently the improvement of the maintenance program.

References

[1]   Alain, P., Michel, G., Maurice, M., "Reliability of systems", Editions Eyrolles, Paris, vol (15), No 4, pp. 778-790, Jul 2000.

[2]   Jean, L., G., "Reliability of systems. Mathematical methods", Masson, Paris, 1991.

[3]   Shophie, M., Cocozza, T., Michel, R., "Various stochastic models for maintenance optimization", *Journal of the French Statistical Society*, vol 3, Paris, pp. 9-21, 2000.

[4]   Cocozza, T., "Stochastic process and reliability of mathematical systems and applications", N°28, 1997.

[5]   Pascal, "Modelling malfunctions of a system under maintenance activities. Research master's report", 2007.

[6]   Agnes, L., Claudie, C., "Stochastic processes and modeling", ismag master 2 - mi00451x, 2012.

[7]   Claire, P. E., "Dependability", 3rd TR - SE option, 2012.

[8]   Banege, L., "Stochastic process. Markov chains and Poisson Process", 2004.

[9]   Bouzaouit, A., HadjadjAouel, E., Bennis, O. "Stochastic modeling for the follow-up the bearing degradation", U.P.B, Sci Bull, N°79, pp. 209-218, 2017.

[10] Bouzaouit, A., Bennis, O., Gahgah, M., "Modelling of the dynamic evolution of the state change of the bearings", *RECENT Journal*, vol (3), pp. 254-258, 2012.

[11] Parick, L., Marc, T., Toscana, R., "Reliability, diagnosis and predictive maintenance systems", Lavoisier SAS, 2012.

[12] Monchy, F., "The maintenance function, Training in Management of Industrial Maintenance", Collection of technologies from University to industry, MASSON, 1991.

[13] Benchouia, N., "The sacking of Reliability Systems has PEMFC fuel", Doctoral thesis, Skikda University, Algeria, 2014.

Improvement of the Hammer Drill Performance (Algerian Quarries Conditions)

Samia NEMOUCHI[1], Elias HADJADJ AOUL[2]

[1] Mechanical Genetics Department, University of August 20,
1955 Skikda21000Algeria, e-mail: Nemouchisamia@hotmail.com
[2] Electromechanical Systems Laboratory, Department of Electromechanical,
BadjiMokhtar – Annaba University, Annaba, Algeria, e-mail: hadjadj.elias@yahoo.fr

Abstract: The factors which influence the performance characteristics of a hammer drill are examined; drilling data are analyzed to determine these factors. Methods for selecting the appropriate drilling are also highlighted. Two models are used in order to compare optimal drilling parameters. The main one is the machine output.

Keywords: Adjustment parameter, axial force, drilling speed, rock, productivity.

1. Introduction

Because of mining industry importance in the national economy, many researchers started to work to increase the production. It is impossible to speak about underground careers or mines, nor even tunnels, without speaking about the drilling machines [1], [2], [3]. Their role is significant and effective for and to the improvement of the production [4]. Several factors can affect drilling performances, which can be divided into controllable factors (rotation speed, air compressed forces) and factors which cannot be controlled (rock properties and geological patterns) [5], [6]. Thus, there have been improved the factors which make it possible to control and link the rate of penetration and the characteristics of the rocks, because the force of drilling and the speed excess influence the drilling tools' wear [7], [8], [9], [10] and thus increase production cost [11].

2. Nomenclature

D: Piston diameter (mm);
d_1: Diameter of the piston rod (mm);
d_2: Diameter of the helical rod (mm);
G: Weight of the piston (kgf);
l_a: Stroke of the piston (mm);
s_a: The useful surface of the piston to carry outward journey;
s_r: The useful surface of the piston to carry return journey;
p_a: Compressed air pressure in the cylinder inlet chamber. It is equal to the pressure in the supply network (kgf / cm^2);
p_e: Compressed air pressure in the exhaust Chamber. We take 0.8 to 1.2 (kgf / cm^2);
k_1: Coefficient taking account of the losses by friction between the piston and the cylinder (k_1 = 0.85 to 0.95);
T_{aux}: Downtime of the puncher due to technical causes (min);
h: Height of the drilled hole (m);
T_{org}: Loss of time due to work organization;
T_f : productive working time of a rotary hammer during a cycle, (min);

k_2: Coefficient taking into account friction and rotation losses of the foil (k_2 = 0.5 to 0.7);
F_a: The force applied to the piston during the outward journey (kgf);
E_{ou}: The energy of a piston stroke (kgf·m);
σ_d: Specific resistance of rock drilled according to the scale of Prof. Protodiakonov;
d_f: Drilling diameter (44 mm);
ξ_e: Efficiency of the energy transmission from the foil to the rock. We take (0.4 to 0.7);
f: The hardness of the rock
u_1: Coefficient of friction between the cutter and the rock (0.3 to 0.5);
C_e: Blunt coefficient (1.2 to 1.3);
α: Sharpening angle, degree;
z: Number of cutting edges (1 to 3);
K_{tec}: technical coefficient of a hammer drill;
$V_{f exp}$: experimental forging speed (m/min);
L: Footage of the drilled hole, (m);
K_{exp}: Operating coefficient of a hammer drill
σ_{com}: Compressive strength.

3. Basic functional parameters of the pneumatic perforator

It is assumed that the compressed air pressure in the cylinder chambers at the inlet and during its exhaust is constant.

The basic parameters of the perforator are as follows:

➢ Number of piston strokes per minute, n_c (coups/min);
➢ Number of foil turns per minute, n_r (tr/min);
➢ Energy from a stroke of the piston, E_c (kgf·m);
➢ Specific consumption of compressed air, C_{air} (m^3/min).

Determination of the forces applied to the piston

The useful surface of the piston for carrying out the outward journey is:

$$s_a = \frac{\pi}{4} \cdot \left(D^2 - d_2^2 \right).$$ (1)

And for the return journey:

$$s_r = \frac{\pi}{4} \left(D^2 - d_1^2 \right). \tag{2}$$

The force applied to the piston during the outward journey is equal to

$$F_a = \left(s_a \cdot p_a - s_r p_e \right) \cdot k_1. \tag{3}$$

The energy of a piston stroke is equal to its kinetic energy of the piston

$$E_{ou} = F_a \cdot l_a. \tag{4}$$

4. Choice of the rational operating regime of percussive drilling machine

The best selection of the perforators depends mainly on the mining conditions, but it depends also on the rock properties and the tools' quality and machine performance. Many researchers have investigated (theoretically or experimentally) the percussion drilling, the researchers carried out tests of exploitation and laboratory tests for the goal to determine the indices of exploitation and the design features, Among researchers Karbatchev and Semenov studied the operation of the mining machinery [13].

4.1. Drilling speed

A: by the first method (A. Karbatchev):

$$V_f = \frac{4 \cdot E_{ou} \cdot n_c}{\pi \cdot d^2 \cdot \delta_{comp} \cdot \left(\text{tg} \frac{\alpha}{2} + u_1 \right) \cdot c_e}; \tag{5}$$

B: by the second method (V. Semenov):

$$V_f = \frac{1.3 \cdot E_{ou} \cdot n_c}{d_f^2 \cdot \sigma_d} \cdot \xi_e. \tag{6}$$

4.2. The productivity of a rotary hammer

Theoretical productivity is the number of meters of holes drilled during the time unit:

$$Q_{theo} = 60 \cdot V_f \cdot T_P. \tag{7}$$

The operating productivity depends on the degree of use of the technical possibilities of a rotary hammer under the concrete conditions of the exploitation:

$$Q_{\exp} = Q_{tech} \cdot k_{\exp} \cdot T_P .$$ (8)

5. Results and discussion

Table1: Technical characteristics of the Atlas Copco pneumatic perforator type (RH658 L) [12]

Parameters	Indices	Values
Piston diameter	D, mm	65
Piston rod diameter	d_1, mm	40
Diameter of the helical rod	d_2, mm	30
Weight of piston	G, kgf	2.4
Piston strokes	l_a, mm	36
Punch mass	M, kg	23

Table 2: The input parameters of a rotary hammer

s_a (cm^2)	2610
s_r (cm^2)	2060
n_c (coups/min)	2222

Table3: The variation of the energy of a stroke of the piston as a function of the pressure of the compressed air

Test nr.	P_a (kgf/cm^2)	E_{ou} (kgf·m)
Test 1	2	0.85
Test 2	2.5	1.205
Test 3	3	1.55
Test 4	3.5	1.91
Test 5	4	2.26
Test 6	4.5	2.614
Test 7	5	2.96
Test 8	5.5	3.319
Test 9	6	3.67
Test 10	6.5	4.024
Test 11	7	4.37

Table4: The variation of the drilling speed as a function of the compressed air pressure by the two methods (A. Karbatchev, V. Semenov)

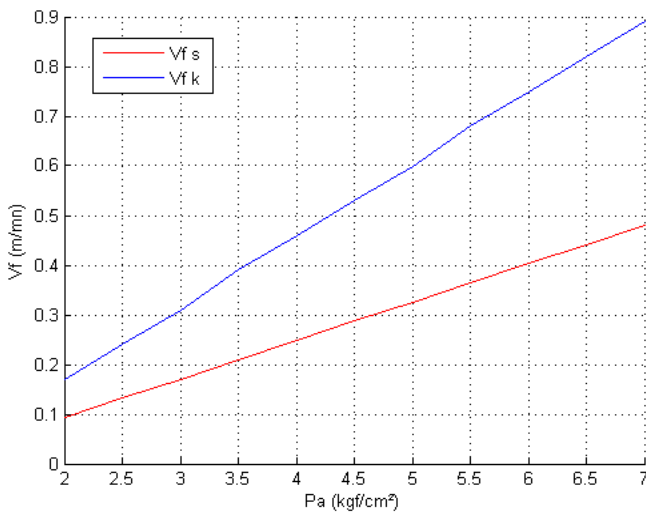| Test nr.	P_a (kgf/cm^2)	V_{fs} (m/min)	V_{fk} (m/min)
Test 1	2	0.093	0.17
Test 2	2.5	0.132	0.24
Test 3	3	0.170	0.31
Test 4	3.5	0.210	0.39
Test 5	4	0.248	0.46
Test 6	4.5	0.287	0.53
Test 7	5	0.325	0.60
Test 8	5.5	0.364	0.68
Test 9	6	0.403	0.75
Test 10	6.5	0.442	0.82
Test 11	7	0.480	0.89

Figure 1: The variation of the drilling speed as a function of the compressed air pressure by the two methods (A. Karbatchev, V. Semenov)

During the experimental experiments the axial force varies, the time and the length are measured; the drilling speed is calculated by the following formula:

$$V_{f\exp} = \frac{L}{T_f} \quad \text{m}/\text{min} .$$

(9)

To process the results, we used the least squares method and checks with the correlation coefficient (see *Fig. 2*)

Table5: Result of the experimental study of a hammer drill working in the conditions of the (Hadja-Soud) quarry (Algeria)

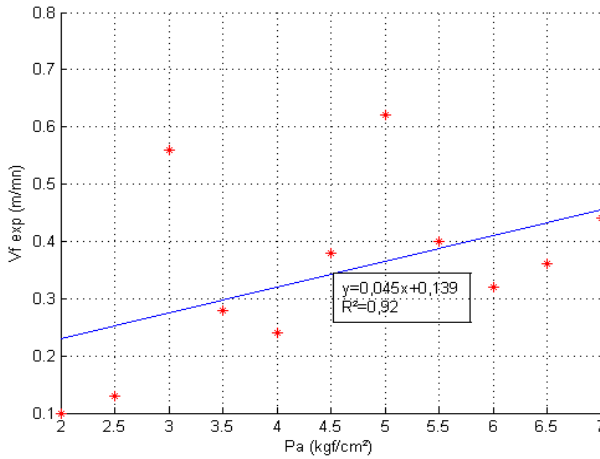| Test nr.	P_a (kgf/cm^2)	$V_{f\,exp}$ (m/min)
Test 1	2	0.10
Test 2	2.5	0.13
Test 3	3	0.56
Test 4	3.5	0.28
Test 5	4	0.24
Test 6	4.5	0.38
Test 7	5	0.62
Test 8	5.5	0.40
Test 9	6	0.32
Test 10	6.5	0.36
Test 11	7	0.44

Figure2: the variation of the experimental forging speed as a function of the compressed air pressure

The results obtained from the productivity (yields) of a rotary hammer under the conditions of the (Hdjar -soud) quarry (Algeria).

Table 6: Productivity (yields) by the method of (V. Semenov)

Test nr.	V_{fs} (m/min)	h (m)	Q_{theo} (m/post)	K_{exp}	Q_{exp} (m/post)
Test 1	0.093	300	39.06	0.95	37.107
Test 2	0.13	250	54.6	0.93	50.77
Test 3	0.17	230	71.4	0.90	64.26
Test 4	0.21	200	88.2	0.87	76.73
Test 5	0.24	180	100.8	0.84	84.67
Test 6	0.28	170	117.6	0.81	95.25
Test 7	0.32	160	134.4	0.78	104.83
Test 8	0.36	150	151.2	0.75	113.4
Test 9	0.40	140	168	0.72	120.96
Test 10	0.44	130	184.8	0.68	125.664
Test 11	0.48	100	2016	0.60	120.96

Table 7: Productivity (yields) by the method of (A. Karbatchev)

Test nr.	V_{fk} (m/min)	h(m)	Q_{theo} (m/post)	K_{exp}	Q_{exp} (m/post)
Test 1	0.17	300	39.06	0.92	65.68
Test 2	0.24	250	54.6	0.88	88.70
Test 3	0.31	230	71.4	0.84	109.36
Test 4	0.39	200	88.2	0.79	129.40
Test 5	0.46	180	100.8	0.74	142.96
Test 6	0.53	170	117.6	0.70	155.82
Test 7	0.60	160	134.4	0.66	166.32
Test 8	0.68	150	151.2	0.62	177.92
Test 9	0.75	140	168	0.58	182.7
Test 10	0.82	130	184.8	0.54	185.97
Test 11	0.89	100	201.6	0.45	168.21

Table 8: Productivity (yields) by the method of (experimental)

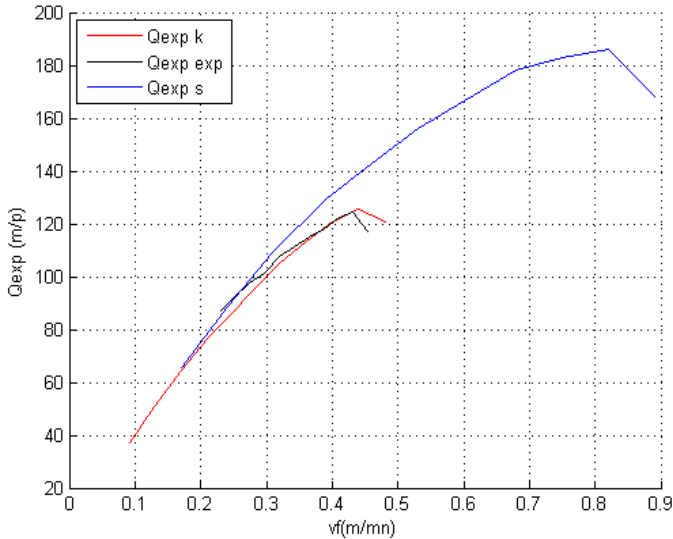| Test nr.	V_{fex} (m/min)	h (m)	Q_{theo} (m/post)	K_{exp}	Q_{exp} (m/post)
Test 1	0.23	300	96.6	0.90	86.94
Test 2	0.252	250	10.5	0.88	92.4
Test 3	0.275	230	113.4	0.86	97.52
Test 4	0.297	200	121.8	0.83	101.09
Test 5	0.32	180	134.4	0.80	107.52
Test 6	0.342	170	142.8	0.78	111.38
Test 7	0.365	160	151.2	0.76	114.91
Test 8	0.387	150	159.6	0.74	118.10
Test 9	0.41	140	172.2	0.71	122.26
Test 10	0.432	130	180.6	0.96	124.61
Test 11	0.455	100	189	0.62	117.18

Figure3: Graphical comparison of the results of calculation of the productivity (yields) of exploitation by the three methods (A. Karbatchev, V. Semenov, experimental)

6. Conclusion

The rational parameters of the operating regime of percussive drilling machines in the (Hdjar -soud) quarry conditions are presented in *Table 9*.

Table 9: Optimal parameters of a hammer drill

P_a Kgf/cm^2	E_{ou} (kgf·m)	V_f (m/min)	productivity	
			Q_{the} (m/post)	Q_{exp} (m/post)
6.5	4.02	0.44	184.8	125.664

The main objective of the present work is to underline the importance of the functioning parameters of the drilling machines and the choice of their quality. Based on the results obtained, it can be drawn that the Karbatchev method is better than Semenov one.

According to the results obtained from the regression model proposed, it can be concluded that there is a strong linear correlation between the speed and air pressure (correlation coefficient values $R \geq 0.92$). A good agreement between theory and experiment is clearly expressed.

References

[1]   Khochman, L, Hadjadj, A.E., "New Méthodologie Sélection of Shilling Machines", *Arian Journal of Information Technologie*, 5 (12), pp. 1310-1312, 2006.

[2]   Mehennaoui, S., Khochemane, L., "Optimization of setting parameters of a rotary drilling rig using Sim Hydraulics Toolbox", *J. Contemporary Engineering Sciences*, vol.8, no.3, pp. 115-120, 2015.

[3]   Derdour, F. Z., Kezza, M., "The optimization of the operation parameters of a rotary percussion shilling machine using the Taguchi methods", *World Journal of Engineering*, vol. 15, lssue 1, pp.62-69, 2017.

[4]   Hoseinie, S. H., Aghababaei, H., Pourrahimian, Y., "Development of a new classification system for assessing of rock mass drillability index (RDi)", *International Journal of Rock Mechanics & Mining Sciences*, vol. 45, pp. 1–10, 2008.

[5]   Yarali, O., Kahraman, S., "The drillability assessment of rocks using the different brittleness values", *Tunnelling and Underground Space Technology*, vol. 26, pp. 406–414, 2011.

[6]   Yaşar, E., Ranjith, P. G., Viete, D. R., "An experimental investigation into the drilling and physico-mechanical properties of a rock-like brittle material", *Journal of Petroleum Science and Engineering*, vol. 76, pp. 185–193, 2011.

[7]   Richard, T., Germai, C., Detournay, E., "A simplified model to explore the robot cause of stick–slip vibrations in shilling system within drag bits", *Journal of Sound and Vibration*, vol. 305, pp. 432–456, 2007.

[8]   Afeni, T. B., "Optimization of drilling and blasting operations in an open pit mine - the SOMAIR experience", *J. Mining Science and Technology*, vol. 19, pp. 736–739, 2009.

[9]   Yue, Z. Q., Lee, C. F., Law, K. T., Tham, L. G., "Automatic monitoring of rotary-percussive drilling for ground characterization—illustrated by a case example in Hong Kong", *International Journal of Rock Mechanics & Mining Sciences*, vol. 41, pp. 573–612, 2004.

[10] Huang, B.-W., Kuang, J.-H., Yu, P., "Effect of crack on Trilling vibration", *Journal of Sound and Vibration*, vol. 322, pp. 1100–1116, 2009.

[11] Ryu, S., Cho, J.-W., Park, J.-Y., Lee, J.-W., Jeong, M.-S., Song, C.-H., Kim, J.-G., and Song, J.-J., "Optimum Operating Conditions of a Multi-Hammer Drilling Machine Assessed using a Linear Percussion Test", *International Journal of Precision Engineering and Manufacturing*, Vol. 16, No. 7, pp. 1415-1422, 2015.

[12] https://www.atlascopco.com< handheld< rok-drills<pneumatic-rok-drills

[13] Rabbouche, Z., Khochemane, L., Bennis, O., "Study of the determination of the rational operating regime of percussion drilling machines", *International Journal of Engineering and Technology (IJET)*, Vol. 9, No. 2, Apr-May 2017.

Thermosolutal Convection in a Porous Medium Cavity Subjected to Heat and Mass Flux: A Discrete Fracture Effect

Zakaria AOUF[1], Chakib SELADJI[1]

[1] Energetic and Applied Thermal Laboratory (ETAP), Faculty of Technology, Aboubekr belkaid University, Tlemcen, 13000, Algeria;
zakaria.aouf@mail.univ-tlemcen.dz / c_seladji@mail.univ-tlemcen.dz

Abstract: Species separation in heterogeneous porous media is a field of interest of many industrial activities. In our investigation, the effect of a single discrete fracture on the thermosolutal convection coupled with the Soret effect have been analyzed. The main results show that the fracture can greatly affect the behavior of the thermogravitational flow and might play a positive role to the separation caused by the Soret effect. Furthermore, the fracture tilted to the cold wall causes a large separation compared to the one tilted to the hot wall with the same angle. Therefore, the separation process could be greatly improved.

Keywords: Soret effect; thermodiffusion; permeability; fracture; separation.

Nomenclature

A	aspect ratio of the porous matrix, H'/L'
a	Rayleigh ratio, R_{TF}/R_{TPM}
C	dimensionless solute concentration, $(C' - C'_0)/\Delta C'$
C'_0	reference solute concentration
$\Delta C'$	characteristic solute concentration, $j'H'/D$
D	mass diffusivity of species
D_T	thermodiffusion coefficient
e	aperture of the fracture, e'/H'
$\vec{g}$	gravitational acceleration vector, m/s²
H'	height of the cavity, m
$\vec{j'}$	constant mass flux, mole/m²/s
K	permeability of the porous medium
K_F	permeability of the fracture
L'	width of the cavity, m

Le	Lewis number, α/D	
N	buoyancy ratio, $\beta_s \cdot \Delta S'/\beta_T \cdot K \cdot \Delta T'$	
Nu	Nusselt number, eq. (7)	
$\vec{\mathbf{q}'}$	constant heat flux, W/m^2	
R_T	thermal Darcy-Rayleigh number for the porous medium, $g \cdot \beta_T \cdot K \cdot \Delta T' \cdot H'/(\alpha \cdot \nu)$	
R_{TF}	thermal Darcy-Rayleigh number for the fracture, $g \cdot \beta_T \cdot K_F \cdot \Delta T' \cdot H'/(\alpha \cdot \nu)$	
S	species separation parameter, $C_{max} - C_{min}$	
S_P	Soret parameter, $S_0' \cdot D_T \cdot \Delta T'/(D \cdot \Delta S')$	
Sh	Sherwood number, Eq. (7)	
t	dimensionless time, $t' \cdot \alpha/(H'^2 \cdot \sigma)$	
T	dimensionless temperature, $(T' - T_0')/\Delta T'$	
T_0'	reference temperature, K	
$\Delta T'$	characteristic temperature, $q'H'/\lambda$	
u	dimensionless velocity in X direction, $u' \cdot H'/\alpha$	
v	dimensionless velocity in Y direction, $v' \cdot H'/\alpha$	
(X,Y)	dimensionless coordinates, $(X'/H', Y'/H')$	

Greek Symbols

α	thermal diffusivity
β_S	solute concentration expansion coefficient
β_T	thermal expansion coefficient
ε	normalized Porosity, ε'/σ
ε'	porosity of the porous medium
λ	thermal conductivity, W/m/K
ν	kinematic viscosity of the fluid
ρ	density of the fluid mixture
$(\rho c)_F$	heat capacity of the fluid mixture
$(\rho c)_{PM}$	heat capacity of the saturated porous medium
σ	heat capacity ratio, $(\rho c)_{PM}/(\rho c)_F$
ψ	dimensionless stream function, ψ'/α

Superscripts

$'$	for dimensional variable

Subscripts

F	Fracture
PM	porous medium
Opt	refers to optimum value
Max	refers to maximum value
Min	refers to minimum value
0	refers to Reference state

S   refers to solutal
T   refers to thermal

1. Introduction

Due to the thermodiffusion effect [1], a mass fraction gradient is spontaneously created when a liquid or gas mixture is subjected to a temperature difference. The thermodiffusion effect, also called Soret effect [2], or Ludwig-Soret effect [3] causes a separation of components, where generally the heavier or larger molecular species concentrate near the colder surface. Coupling of this Soret effect with natural convection magnifies the primary separation coming from the Soret effect. This is known as the thermogravitational phenomenon. Clusius and Dickel [4] invented the thermogravitational column (TGC) in order to separate isotopes, which was developed theoretically by Furry et al. [5] and extended for liquids by DeGroot [6]. However, the developed TGC was declined due to the operating features and so researchers are encouraged to combine the TGC technique with other separation mechanisms and modified cell designs [7]. Lorenz and Emery [8] promoted the idea of filling the thermogravitational cells with a porous medium, which allows working with large dimension cells. In this regard, many works have recently been carried out to buttress these phenomena. For instance, Lee et al. [9] investigated the effect of various forms of non-uniform basic temperature gradients on thermogravitational convection in an isotropic porous layer using non-equilibrium models. Two-field temperature models were used for the energy equation and the Forchheimer-extended Darcy model to describe the flow. It is found that the linear temperature profile provides a reinforcement of stability, compared with the non-uniform temperature gradients. Abahri et al. [10] studied the thermogravitational separation of a binary liquid mixture in a horizontal porous annulus space heated isothermally from the inner cylinder. Theoretical and numerical results reveal that the separation can be increased for small values of Rayleigh number. Grigor'ev and Rivin [11] used the thermogravitational column to determine thermodiffusion factors of organic liquids mixture. A comparison of the calculated values of the Soret coefficient and the experimental data obtained has been presented with a satisfactory agreement. In terms of the separation ratio, and the cross-diffusion, Lewis and Rayleigh numbers, Mutschler et al. [12] suggests two analytical models to describe the thermogravitational separation of N-component mixtures in a vertical cavity filled by a porous medium. Their theoretical model supports strongly the experimental results. Recently, Mojtabi et al. [13] studied the influence of the thickness and the nature of the bounding horizontal plates on the separation of a binary mixture in a horizontal porous cavity. Authors found that the ratio of the plate to the porous layer thickness and the ratio of their thermal

conductivity greatly affect the species separation. The analytical results were confirmed by direct numerical simulations. Kozlova and Ryzhkov [14], studied the transient separation of a multicomponent mixture in a cylindrical thermogravitational column. The evaluation of separation in vertical direction is solved analytically and compared with two-dimensional numerical simulation of binary and ternary mixture, where a good agreement is observed. Hashemipour et al. [15] performed an experimental and numerical study to separate toluene/n-heptane mixture by TGC. Good concordance can be seen between experimental and numerical results. The separation factor can reach 1.17 when the optimal conditions are achieved (feed flow rate, cut, temperature gradient). In a packed thermogravitational cell, maximum separation is associated with an optimal permeability of porous medium as it was a subject of interest to most researchers [16], [17].

Thermosolutal convection in vertical porous cavity can be driven either by double diffusion (the solute gradient is induced by the solute boundary condition), or by cross diffusion (the solute gradient is induced by thermal boundary condition via Soret effect) [18]. However, in many practical applications, the thermosolutal convection is driven by both double diffusive convection and Soret effect [19]. In this wise, Amahmid et al. [20] studied the double diffusive convection in a vertical cavity subjected to horizontal gradient of heat and mass. They focused on the situation in which thermal and solutal buoyancy forces are opposed to each other and found that multiple steady state solutions are possible. Er-Raki et al. [21] studied the Soret effect on double diffusive boundary layer flowing in a vertical porous layer. Based on the parallel flow approximation, an analytical solution was developed which allows a detailed parametric study of the governing parameters effect on the convective flow and on heat and mass transfer characteristics. These analytical results were compared with the numerical solution. Jiang et al. [22] examined numerically the effect of natural convection on the Soret effect in a vertical cavity heated laterally. They used the mathematical model of Shukla and Firoozabadi to calculate molecular diffusion, thermodiffusion, and pressure diffusion coefficients as functions of temperature, pressure, and other physical properties of the binary mixture at each point of the grid. As a function of separation factor, their results indicate that as permeability increases, separation increases until it peaks at 10 md (md: millidarcy, a non-S.I. unit of the permeability), then decreases. Jiang et al. [23] examined using the same mathematical model the effect of medium heterogeneity in a stratified porous vertical cavity. They found that the Soret effect is strongly dependent on medium heterogeneity; the authors announced that the separation in heterogeneous porous medium is always greater than in homogeneous one. Their declaration is further elaborated in the results section of this paper. Jaber [24] thereafter studied the effect of the permeability in a fractured porous medium

cavity filled with a ternary mixture with the consideration of likely thermodiffusion effect. The system was set at 10 md for the permeability of the porous medium, while the permeability of the fracture was varied from 10 to 1000 md. The outcome showed an increasing of the flow field in the fracture, which affects the behavior of each component.

Limited studies considered the Soret effect while investigating the thermosolutal convection phenomenon in heterogeneous porous media. This study has the objective of investigating the role of a discrete fracture on thermosolutal convection coupled with the Soret effect in an isotropic porous media saturated by a binary fluid. The fracture has been considered as another porous medium with slightly higher permeability. More precisely, the influence of the fracture characteristics (permeability, positioning, thickness) on the fluid flow and heat and mass transfer is examined in terms of the separation parameter "S", which is defined as the difference of the maximum concentration in the hot wall and the minimum concentration in the cold wall [25].

2. Problem formulation

The problem studied in this paper is performed using a numerical finite difference method. Within a rectangular cavity, the thermosolutal convection is coupled with the Soret effect in a two-dimensional fractured porous media saturated by a binary fluid. The same configuration is used as the one presented in [21]. Neumann boundary conditions for solute and temperature are applied to the vertical walls of the cavity such that it is heated and salted from the right-end, while the horizontal walls are adiabatic and impermeable (*Fig. 1*). Darcy's law is governing the flow which is assumed laminar and incompressible. The thermophysical properties of the mixture are considered constant. Note that for this study, the Soret parameter is assumed constant, the negligible effect of the mass concentration variation on the heat transfer (Dufour effect) is not considered. Using the Boussinesq approximation, the dimensionless governing equations of the mathematical model are as follows [26]:

$$\frac{\partial^2 \psi}{\partial x^2} + \frac{\partial^2 \psi}{\partial y^2} = -R_T \cdot \left(\frac{\partial T}{\partial x} + N \cdot \frac{\partial C}{\partial x} \right), \tag{1}$$

$$\varepsilon \cdot \frac{\partial C}{\partial t} + \frac{\partial (u \cdot C)}{\partial x} + \frac{\partial (v \cdot C)}{\partial y} = \frac{1}{Le} \cdot \left(\nabla^2 C + S_P \cdot \nabla^2 T \right), \tag{2}$$

$$\frac{\partial T}{\partial t} + \frac{\partial (uT)}{\partial x} + \frac{\partial (vT)}{\partial y} = \nabla^2 T. \tag{3}$$
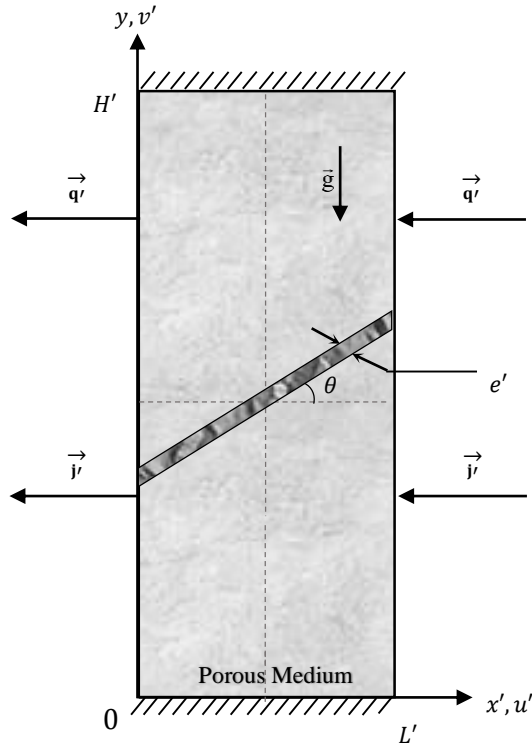
Figure 1: Geometry of the physical system

Introducing the stream function (the flow velocity components can be expressed as the derivatives of the scalar stream function), the dimensionless velocity components are calculated as follows:

$$u = \frac{\partial \psi}{\partial y}; \quad v = -\frac{\partial \psi}{\partial x} \ . \tag{4}$$

The non-dimensional governing parameters appearing in the equations are the thermal Darcy-Rayleigh number, R_T, the Lewis number Le, the buoyancy ratio N, the Soret parameter, Sp, and the aspect ratio, A. They are defined in equation 5.

$$R_T = \frac{g\beta_T K \Delta T' H'}{\alpha \nu}; \quad Le = \frac{\alpha}{D}; \quad N = \frac{\beta_S \Delta C'}{\beta_T \Delta T'}.$$
$$\varepsilon = \frac{\varepsilon'}{\sigma}; \quad Sp = \frac{D_T C_0' \Delta T'}{D \Delta C'}; \quad A = \frac{H'}{L'} = 5 \tag{5}$$

Note, that the classical separation ratio φ is related to S_p and N by the relation $Sp = \varphi / N$ [26]. In terms of dimensionless variables, the boundary conditions are defined in (6) [21].

$$
\begin{cases}
\psi = 0, & \dfrac{\partial T}{\partial x} = 1, & \dfrac{\partial C}{\partial x} = 1 - S_p & \text{for} \quad x \in \left\{0, \dfrac{1}{A}\right\} \; ; y \in [0, \quad 1], \\[2ex]
\psi = 0, & \dfrac{\partial T}{\partial x} = 0, & \dfrac{\partial C}{\partial x} + S_p \cdot \dfrac{\partial T}{\partial y} = 0 & \text{for} \quad x \in \left[0, \dfrac{1}{A}\right] \; ; y \in \{0,1\}.
\end{cases}
\tag{6}
$$

The heat and mass transfer rates, quantified in terms of the Nusselt and Sherwood numbers, can be calculated from the following expressions:

$$
Nu = \frac{1}{\nabla T} = \frac{1}{T(L',H'/2) - T(0,H'/2)}
$$
$$
Sh = \frac{1}{\nabla C} = \frac{1}{C(L',H'/2) - C(0,H'/2)}
\tag{7}
$$

The mathematical model is applied to the entire cavity. Moreover, a specific permeability is applied to the fracture, which is expressed by a different Rayleigh number (R_{TF}).

3. Numerical method

The governing equations are discretized using a central finite difference scheme and solved with the alternate direction implicit (ADI) method, using a (Fortran 90) numerical code software. A first order forward scheme is used for the transitory term in the Darcy equation, which is solved with the successive over relaxation (SOR) method. A second order forward or backward scheme is used for Neumann boundary conditions. The results are obtained when the system satisfies the convergence criteria (the relative error corresponding to T, C, and Ψ between successive time steps for each node is less than 10^{-9}). The effect of the grid size on the results was analyzed using uniform rectangular mesh. *Table 1* indicates satisfying results when using a grid with at least 171×171 nodes. The maximum relative errors for *Nu*, *Sh*, and *S* do not exceed 1.5%.

Table 1: Effect of the grid size for $R_T = 50$, $R_{TF} = 150$, $Le = 10$, $S_p = 0.5$, and $\theta = 70$.

Grid	*Nu*	*Sh*	*S*	Relative error %
71×71	2.5400	11.59	0.3837	4.93
101×101	2.5430	11.8	0.3916	2.97
131×131	2.5480	11.91	0.3956	1.98
171×171	2.5510	11.97	0.3976	1.48
301×301	2.5540	12.05	0.4015	0.52
501×501	2.5548	12.09	0.4035	0.02
601×601	2.5549	12.09	0.4036	0

4. Results and analysis

The aim of this study is to understand the effects of a discrete fracture on heat and mass transfer in porous media. More attention is given to determine the optimum fracture conditions that gives a higher separation for an aspect form $A = 5$, and a buoyancy ratio $N = 0.4$. To achieve this objective, an inclined fracture passed across the center of the cavity was established as depicted in *Fig. 1*. The latter is characterized by an angle θ, an aperture e, and a specific Rayleigh number R_{TF} as determined by the fracture permeability. Furthermore, the ratio of the fracture Rayleigh number R_{TF} over the porous medium Rayleigh number R_T is calculated and denoted as, a=R_{TF}/R_T. For all simulations, a mono-cellular flow occurred in the cavity.

4.1 Validation

The mathematical model and resolution process need to be validated using a known case. For this purpose, the boundary conditions were modified to reproduce the results of Khadiri et al. [26] in which the authors studied the Soret effect on double-diffusive convection in a square porous cavity heated and salted from the bottom *Fig. 2* shows the comparison of the concentration profiles in the mid-width of the cavity corresponding to a bi-cellular flow obtained with different values of Soret parameter S_p from this study and that of [26], good agreement could be seen. Results show that at $Y = 0.18$, the concentration remains unchanged when S_p is varied. This behavior was denominated by [26] as a neutral position and has not been explained. However, using a small Rayleigh number $R_T = 50$ (for example), the Soret effect becomes more important and dominates convection forces, for which these neutral positions disappear. This outcome is shown in *Fig. 3* even though such results were not presented by [26].
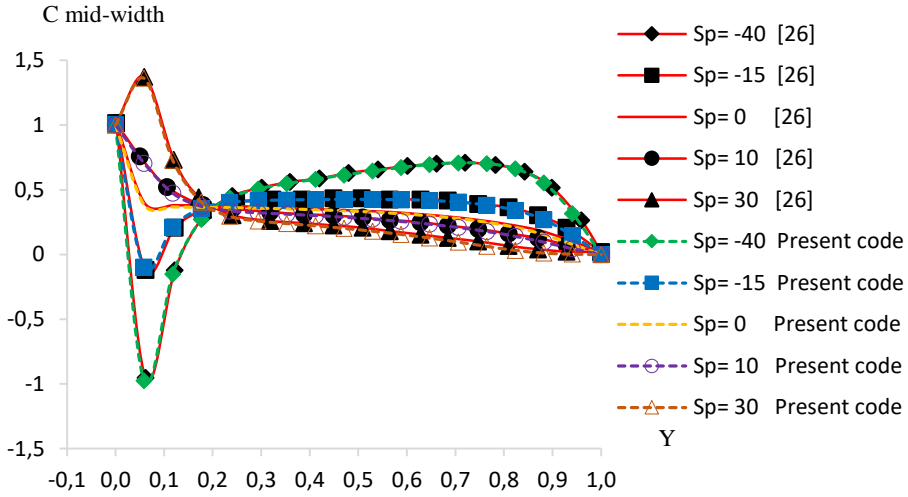
Figure 2: Vertical profiles of concentration at *X*=0.5 for *A*=1, R_T=200, *Le*=10, *N*=0.1, and various values of *Sp*
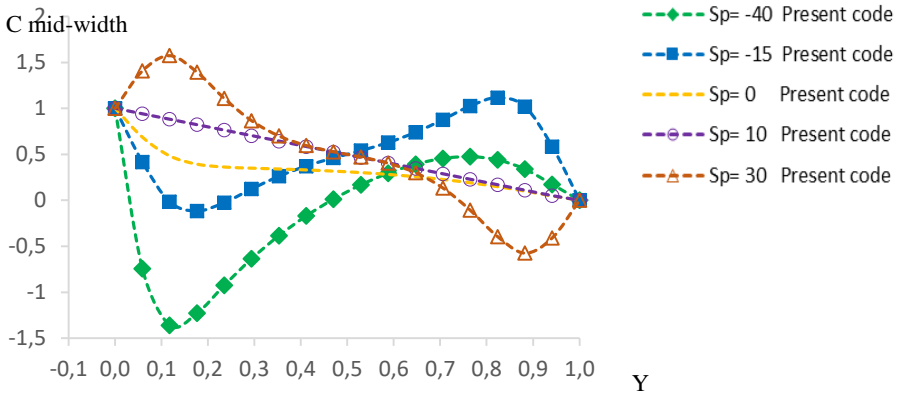

Figure 3: Vertical profiles of concentration at *X* = 0.5 for *A* = 1, R_T = 50, *Le* = 10, *N* = 0.1, and various values of S_p

4.2. Soret parameter effects

The contribution of the convection with the Soret coefficient depending on the permeability of the medium can lead to a higher separation of the mixture constituents. The effect of Soret parameter is investigated for an extent Rayleigh number scope. *Fig. 4* shows that the separation for all the Soret parameter has the same pattern, in which three different zones are distinguished: at low Rayleigh number ($R_T < 0.01$) the permeability of the porous medium is low, and only diffusion and thermodiffusion effects cause the mass transfer (purely diffusive regime). Augmenting R_T leads to growth in convection forces, the contribution of the convection forces with the Soret effect performs the peak of the separation at an optimal Rayleigh number R_{Topt} and creates a diagonal concentration gradient in the cavity. At high values of Rayleigh number, convection forces dominate the process, mixing the constituents of the binary fluid, where thermodiffusion is considered as a secondary phenomenon displays no significant effect, and the separation in this zone is less than in purely diffusive regime zone. Furthermore, the separation is also affected by the Soret parameter sign. Generally, for positive Soret value, the bigger and heavier components migrate to the cold wall of the cavity (left end) and might give a negative Sherwood number. However, for negative value of Soret parameter, thermodiffusion effect is opposing diffusion effect (in our case), were the heavier component moves towards the hot wall of the cavity (right-end) and withhold the gradient of concentration, which explains the higher separation values. More results are shown in *Table 2*. For $R_T = 0.01$, the gradient of concentration is made horizontally and (the difference of concentration calculated at the middle of the cavity) is almost the same as S, but for $R_T = 1$, the concentration gradient is diagonal, and the separation becomes more important. Note that depending on the reference value in the dimensionless process, the separation can be higher than 1.
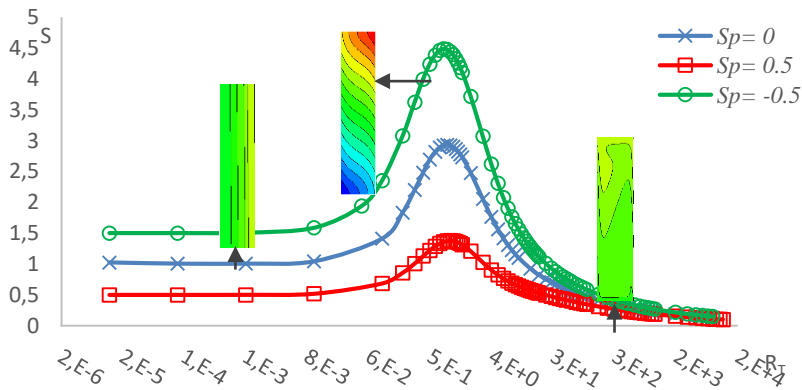

Figure 4: Separation as function of R_T for *Le*=10, *N*=0.4, and various values of *Sp*

Table 2. Effect of Soret parameter (*Sp*) sign at different R_T for *Le*=10 and homogeneous porous medium

R_T	Sp	ψ_{Min}	ψ_{Max}	Nu	Sh	$\nabla C = \frac{1}{Sh}$	S
0.01	-5	0.0E+00	4.2E-04	1.000	0.167	5.995	6.792
	-2	0.0E+00	2.7E-04	1.000	0.335	2.985	3.253
	0	0.0E+00	1.7E-04	1.000	1.000	1.000	1.005
	2	0.0E+00	7.5E-04	1.000	-1.000	-1.000	1.024
	5	-7.5E-04	0.0E+00	1.000	-0.250	-4.000	4.093
1	-5	0.0E+00	1.9E-01	1.018	0.446	2.242	17.139
	-2	0.0E+00	1.7E-01	1.013	0.748	1.337	8.859
	0	0.0E+00	1.5E-01	1.009	1.803	0.555	2.923
	2	0.0E+00	9.4E-02	1.004	-1.470	-0.680	3.121
	5	-4.9E-02	0.0E+00	1.001	-0.281	-3.559	9.691
450	-5	0.0E+00	2.6E+00	4.884	6.336	0.158	0.818
	-2	0.0E+00	3.0E+00	5.523	7.703	0.130	0.515
	0	0.0E+00	3.4E+00	5.809	14.870	0.067	0.296
	2	0.0E+00	3.8E+00	5.611	-13.990	-0.071	0.110
	5	-3.2E-01	5.9E+00	5.008	-2.191	-0.456	1.542
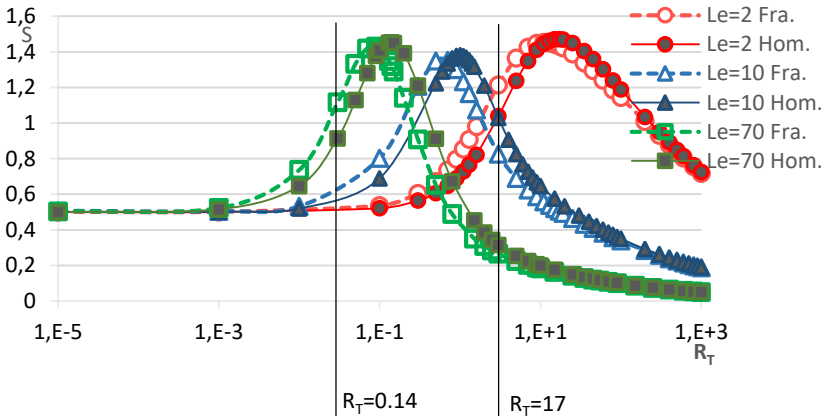
Figure 5. Separation in fractured PM vs. Homogeneous PM for $\theta = 70°$, $S_p = 0.5$, $\alpha = 30$, and different values of *Le*
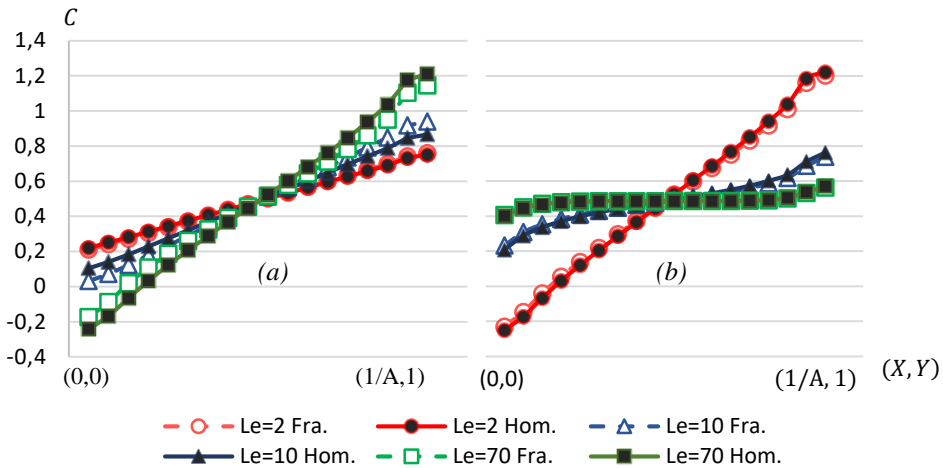
Figure 6. Diagonal profiles of concentration (with & without Fracture) for
Le = 2, 10, 70 at *(a)* R_T = 0.14, *(b)* R_T = 17

4.3 Effect of the Lewis number

Fig. 5 shows the separation parameter S for different value of Le for an inclined fracture of $\theta = 70°$, $e = 0.038$, and a Rayleigh ratio $a = 30$, solid lines correspond to homogeneous porous medium (HPM), and dotted ones correspond to heterogeneous (fractured) porous medium (FPM). It is clearly demonstrated that the more the Lewis number is increasing (Le), the convection forces becomes more effective, which moves forward the optimal Rayleigh number R_{Topt}, and makes the peak of separation more pointed. Similar results were found by [27] in horizontal cavity.

The fracture behavior towards different Le values is almost the same, adding a fracture (characterized by a higher permeability) to the porous medium, leads to improving the entire permeability of the medium, which favors more the convection forces, and gives a better separation S as long as is less than R_{Topt}. For Rayleigh numbers R_T more than R_{Topt}, the fracture decreases the separation. However, a slight difference is observed for higher Lewis numbers, the fracture has more negative effect on the separation when Rayleigh number R_T is more than R_{Topt}. This could be referred to the nature of the fluid, in the literature $Le = 2$ for gas [27], $Le = 10,70$ for liquid [28].

Fig. 6 shows the concentration profiles at the diagonal for homogenous and fractured porous media for a fracture of $\theta = 70°$, $e = 0.038$, and Rayleigh ratio $a = 30$. At the center of the cavity, the mixture persists homogeneous for different Rayleigh and Lewis numbers, deviation is more observed in the cavity extremes. The optimal Rayleigh number for $Le = 70$ is $R_T = 0.14$, what explains a higher concentration gradient for $Le = 70$ as seen in *Fig. 6 (a)*, for $Le = 10$, the fracture plays a positive role, raising the total permeability of the medium and augmenting the separation S by 19.2%. However, for $Le = 2$, and $R_T = 0.14$, there are no convection forces in the cavity, the fracture has no significance effect, and the concentration profiles represent the boundary conditions effect. *Fig. 6 (b)* shows a higher concentration gradient for $Le = 2$, since $R_T = 17$ corresponding to the optimum. However, for $Le = 10$, and 70, $R_T = 17$ is higher than the optimal, and the convection forces cause a homogeneous mixture.

4.4. The fracture's permeability effects

In order to better understand and confirm the effect of the fracture's permeability on the separation, different Rayleigh numbers were set to the fracture R_{TF}, for different values of porous medium Rayleigh number R_T. Three different values of R_T were investigated vis-à-vis; less than, equal, and higher than the optimum correspond to *(a)*, *(b)*, and *(c)* respectively (*Fig. 7*). Comparing the separation caused by the fracture with that caused by the homogeneous porous medium, when the porous medium permeability is less than the optimal *(a)*, the fracture plays an important role, raising the separation by 93% at its peak $R_T = 3$, then it starts decreasing. However, when the porous medium's permeability is higher than or equal to the optimal as in *(b)* and *(c)*, the fracture can apply a negative effect on the separation. The fracture existence strongly affects the behavior at the optimal Rayleigh number R_{opt}. For a heterogeneous porous media, it was stated by [23] that due to heterogeneity condition of the problem, the separation ratio in heterogeneous porous media is always higher than that in homogeneous porous media. However, throughout these results, their statement is valid when the total porous medium permeability is less than the optimal, and this does not contradict with their results.
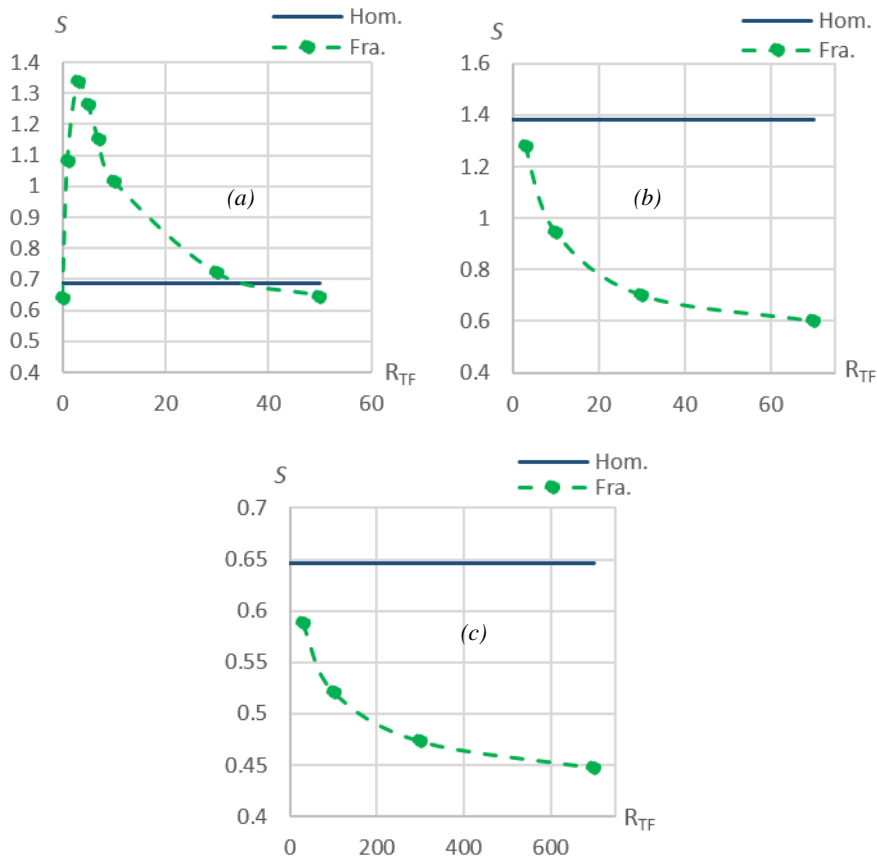
Figure 7: Effect of the fracture's permeability on the separation for $Le = 10$, $\theta = 90°$, $e = 0.038$, and different Rayleigh numbers *(a) $R_T = 0.1$, (b) $R_T = 1$, (c) $R_T = 10$*

4.5. The fracture's orientation (θ) effect

Separation of component by Soret effect becomes more important when it is accompanied by low convection forces. For a better understanding of how these two effects contribute together, a special attention is given to the region that follows the onset of the convection forces. We traced the separation at low Rayleigh number (R_T) for $e = 0.038$, $S_p = 0.5$, $Le = 10$, and $\alpha = 30$ for different fracture's angles (*Fig. 8*). The results show that for R_T less than 0.5, the separation in fractured porous media is always better than in homogeneous ones. As predicted, fractures precede the optimal R_T for the separation whatever the angle. However, comparing vertically symmetrical fractures, curves are identical for $\theta = 70°$ and $\theta = 110°$, but they become different for angles near the horizontal. In

order to understand the main cause of this variance, the heat and mass transfer represented by Nusselt and Sherwood numbers are presented in *Fig. 9 (a)* and *(b)* respectively. For a vertical fracture, the mass transfer is almost the same as in homogeneous porous medium (without fracture) with some slight decrease, while the horizontal fracture significantly increases it. As explained in [29], the horizontal dynamics in the Clusius and Dickel thermogravitational column is governed by Soret effect, and at low Rayleigh number R_T weak convection forces exist, thus, the mass transfer is made horizontally by diffusion and thermodiffusion effects. Therefore, the more the fracture is inclined towards the horizontal, the higher mass transfer is. The same observation can be seen for Nusselt number (*Fig. 9 (a)*) since the same boundary condition are applied for heat and mass transfer.
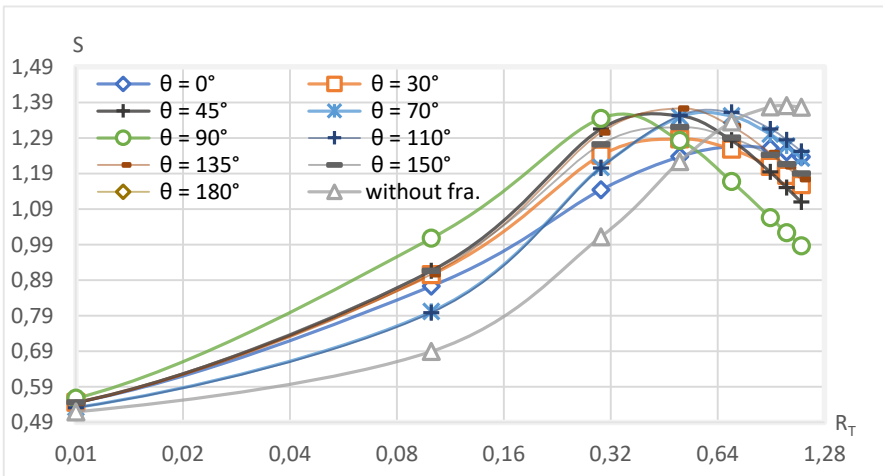
Figure 8: Effect of the fracture's orientation on the separation for Le=10, e=0.038, Sp=0.5, and α=30 at low Rayleigh numbers
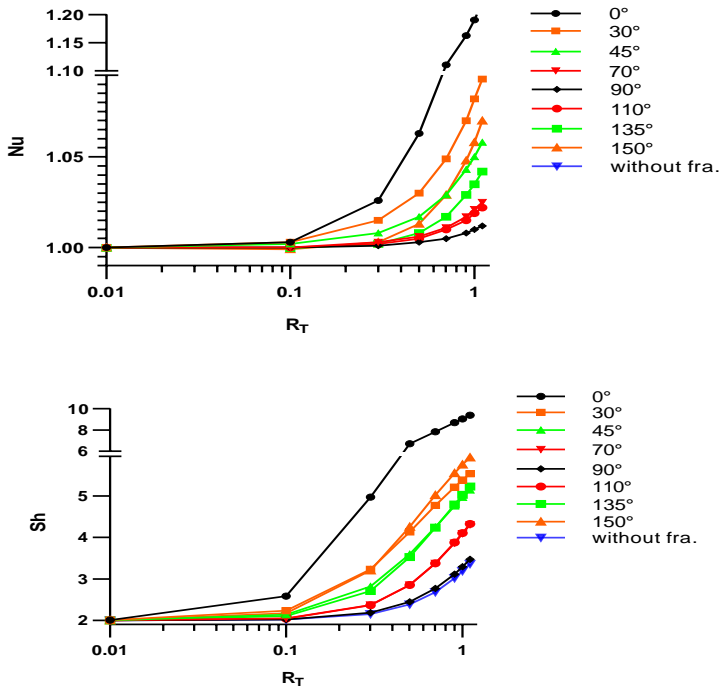
Figure 9: Nusselt (*Nu*) and Sherwood (*Sh*) numbers for *Le*=10, *e*=0.038, *Sp*=0.5, and *α*=30 at low Rayleigh numbers

The heat and mass transfer made by vertically symmetric fractures of an inclination of θ and π-θ is the same in most cases, but it becomes more differentiated for small θ (closely horizontal fracture). Note that the length of the fracture is variable with the angle, but it is the same for vertically symmetric fractures.

The difference between the vertically symmetric fracture behavior towards heat and mass transfer is a result of a combination of several effects including the direction of convection circulation, the gravity acceleration, boundary conditions, and the Soret parameter sign in our case, for positive Soret parameter, the mass transfer for the heavier component is made towards the cold wall (left end) by both diffusion and thermodiffusion effects. However, with the same counter clockwise convection flow direction, fractures inclined towards the cold wall (left-end) and heated from the bottom have more important convection forces than the ones inclined toward the hot wall (right-end) and heated from the top. For inclined fracture near the vertical, this difference no longer persists, for instance $\theta = 70°$, and $\theta = 110°$.

5. Conclusion

Thermosolutal convection in porous media is significantly affected by the contribution of Soret effect and convection forces, where the permeability of the medium is the dominant parameter. The fracture effect on the thermosolutal convection, considering the Soret effect has been rarely studied before. In this investigation, a fractured porous medium from the center of the cavity is considered and characterized by slightly higher permeability to improve the TGC separation technique.

Deducing from the analysis carried out in this study, we conclude that the fracture in the porous medium strongly influences the behavior of the thermogravitational flow and the corresponding heat and mass transfer performance in the cavity, which has effects on the separation.

At low Rayleigh numbers R_T, the Soret effect dominates the mass transfer process, and the addition of a fracture to the porous medium plays an important role in enhancing convective forces, which leads to increase heat and mass transfer and promotes better separations (depending on its permeability and position). However, the fracture can cause a negative effect on the separation when the Rayleigh number of the porous medium is higher or equal to the optimal value.

Particular attention is given to the orientation of the fracture. It comes from the analysis, that at low Rayleigh number R_T, the more the inclination of the fracture is close to the horizontal; the more it favors the heat and mass transfer. Furthermore, due to the heating source, fractures inclined towards the cold wall have higher convection forces than the ones inclined towards the hot wall. This could increase or decrease the separation depending on R_T and α.

References

[1]   De Groot, S. R., "L'effet Soret-diffusion thermique dans les phases condenses", Doctoral Thesis, Amsterdam, 1945.
[2]   Soret, C., "Sur l'état d'équilibre que prend au point de vue de sa concentration une dissolution saline primitivement homogène dont deux parties sont portées à des températures différentes", *Arch. Sci. Phys. Nat.*, vol. 2, pp. 48-61, 1879.
[3]   Ludwig, C., "Diffusion zwischen ungleich erwarmten Orten gleich zusammengesetzer", Akad. Wien. Math. Naturwiss, vol 20, pp. 539-539, 1856.
[4]   Clusius, K. and Dickel, G., "New process for separation of gas mixtures and isotopes", *Naturwissenschaften*, vol. 26, pp. 546-546, 1938.
[5]   Furry, W. H., Jones, R. C., and Onsager, L., "On the theory of isotope separation by thermal diffusion", *Phys. Rev.*, vol. 55, pp.1083-1093, 1939.
[6]   DeGroot, S. R., "Theorie phénoménologique du procédé thermogravitationnel de séparation dans un liquid", *Physica IX*, vol. 8, pp. 801-816, 1942.
[7]   Philomena, G. G. and Barbara, F., "Clusius-Dickel separation: a new look at an old technique", *Separation Science*, vol. 12, no. 2, pp. 103-169, 1977.

[8]   Lorenz, M. and Emery, A. H., "The packed thermodiffusion column", *Chemical Engineering Science*, vol. 11, pp. 16-23, 1959.

[9]   Lee, J., Shivakumara, I. S. and Mamatha, A. L., "Effect of non-uniform temperature gradients on thermogravitational convection in a porous layer using a thermal non-equilibrium model", *J. Porous Media*, vol. 14, pp. 659-669, 2011.

[10] Abahri, O., Sadaoui, D., Mansouri, K., Mojtabi, A. and Mojtabi, M. C., "Thermogravitational separation in horizontal annular porous cell", *Mechanics & Industry*, vol. 18, no. 1, pp. 106-116, 2017.

[11] Grigor'ev, V. and Rivin, E., "Determination of the Soret coefficient based on the separation of mixtures of organic liquids in a thermogravitational column", *Theoretical Foundations of Chemical Engineering*, vol. 51, no. 4, pp. 464-467, 2017.

[12] Mutschler, D., Larabi, M. A. and Mojtabi, A., "Theoretical models for the thermogravitational separation process in porous media filled by n-component mixtures". *The European Physical Journal E*, vol. 40, no. 4, pp. 49-56, 2017.

[13] Mojtabi, A., Ouattara, B., Rees, D. A. S. and Charrier-Mojtabi, M.-C., "The effect of conducting bounding horizontal plates on species separation in porous cavity saturated by a binary mixture", *Int. J. Heat Mass Transfer*, vol. 126, pp. 479-488, 2018.

[14] Kozlova, S. V. and Ryzhkov, I. I., "The transient separation of multicomponent mixtures in a cylindrical thermogravitational column", *Int. J. Heat Mass Transfer*, vol. 126, pp. 660-669, 2018.

[15] Hashemipour, N., Karimi-sabet, J., Motahari, K., Monfared, S. M., Amini, Y., And Moosavian, M. A., "Experimental and simulation investigation on separation of binary hydrocarbon mixture by thermogravitational column", Molliq, 2018.

[16] Benano-Melly, L. B., Caltagirone, J. P., Faissat, B., Montel, F., and Costeseque, P., "Modelling Soret coefficient measurement experiments in porous media considering thermal and solutal convection", *Int. J. Heat Mass Transfer*, vol. 44, pp. 1285-1285, 2001.

[17] Marcoux, M. and Costeseque, P., "Study of transversal dimension influence on species separation in thermogravitational diffusion columns", *Journal of Non-Equilibrium Thermodynamics*, vol. 32, no. 3, pp. 289-298, 2007.

[18] Boutana, N., Bahloul, A., Vasseur, P., and Joly, F., "Soret and double diffusive convection in a porous cavity", *J. Porous Media*, vol. 7, no. 1, pp. 41-57, 2004.

[19] Alloui, Z., Merabtine A., and Vasseur, P., "Soret and thermosolutal effects on natural convection in a vertical cavity filled with a binary mixture", *The Canadian Journal of Chemical Engineering,* vol. 88, pp. 718-727, 2010.

[20] Amahmid, A., Hasnaoui, M., Mamou, M., and Vasseur, P., "On the transition between aiding and opposing double diffusive flows in a vertical porous matrix", *J. Porous Media*, vol. 3, pp. 123-137, 2000.

[21] Er-Raki, M., Hasnaoui, M., Amahmid, A., Mamou, M., and Bourich, M., "Soret effect on double-diffusive boundary layer flows in a vertical porous cavity", *J. Porous Media*, vol. 10, pp. 783-795, 2007.

[22] Jiang, C. G., Saghir, M. Z., Kawaji, M., and Ghorayeb, K., "Two-dimensional numerical simulation of thermogravitational convection in a vertical porous column filled with a binary fluid mixture", *Int. Journal of Thermal Sciences*, vol.43, pp. 1057-1065, 2004.

[23] Jiang, C. G., Saghir, M. Z., and Kawaji, M., "Numerical analysis of thermal-solutal convection in heterogeneous porous media", *Journal of Applied Mechanics*, vol. 73, pp. 21-25, 2005.

[24] Jaber, T. J., "Numerical study of permeability effect on convection in fractured porous media filled with hydrocarbon ternary mixture", *Proceedings of CHT-08 ICHMT Int. Symposium on Advances in Computational Heat Transfer*, Marrakesh, Morocco, May 11-16, 2008.

[25] Charrier-Mojtabi, M. C., El Hajjar, B., Ouattara, B., Mojtabi, A., and Costesèque, P., "Soret-driven convection and separation of binary mixtures in a porous horizontal slot submitted to a heat flux", *C. R. Mecanique*, vol. 339, pp. 303-309, 2011.

[26] Khadiri, A., Amahmid, A., Hasnaoui, M., and Rtibi, A., "Soret effect on double-diffusive convection in a square cavity heated and salted from below", *Numerical Heat Transfer*, Part A, vol. 57, pp. 848-868, 2010.

[27] El Hajjar, B., "Sur le couplage Thermodiffusion - Convection: Séparation et instabilités induites par de nouvelles configurations géométriques et thermiques", Doctoral Thesis, IMFT, Toulouse, 2008.

[28] Goyeau, B., Songbe, J. P., and Gobin, D., "Numerical study of double-diffusive natural convection in a porous cavity using the Darcy–Brinkman formulation", *Int. J. Heat Mass Transfer*, vol. 39, pp. 1363-1378, 1996.

[29] Costesèque P., Fargue D., Jamet P., "Thermodiffusion in porous media and its consequences", in "Thermal nonequilibrium phenomena in fluid mixtures", *Lecture Notes in Physics*, Köhler W. and Wiegand S., Eds., Springer, Berlin, Heidelberg vol. 584, pp. 389-427, 2002.

Corrosion Resistance of Coatings Produced by Spraying Powders Under a Laser Beam in a Saline Environment NaCl 3% by the Electrochemical Method

Samia AOUICI[1], El Hadi BOUSSAHA[2], Ferial KRID[3],
Fadia MECHATI[3]

[1]Department of Mechanical Engineering, Faculty of Technology,
University 20 August 1955 Skikda, Algeria, e-mail: auoici_s@yahoo.fr, s.aouici@univ-skikda
[2]Department of Petrochemistry and Process Engineering, Faculty of Technology,
University 20 August 1955 Skikda, Algeria, e-mail: bhedi3@yahoo.fr
[3]Chemical and Environmental Engineering Research Laboratory, LGCE, Department of
Petrochemistry and Process Engineering, Faculty of Technology, University 20 August 1955
Skikda, Algeria, e-mail: kridferial11@gmail.com f.krid@univ-skikda.dz
f.mechati_26@hotmail.com

Abstract: The manuscript focuses on the study of corrosion resistance in NaCl medium of a 304L type stainless steel after application of protective nickel-based and cobalt-based coatings produced by powder spraying under a continuous CO_2 laser (10.6 µm wavelength) beam. Using polarization and electrochemical impedance spectroscopy methods, the results found confirm that metallic coatings produced under high energy beams offer excellent protection up to an efficiency of $E = 98.12\%$ in aggressive environments with salinity to 3%.

Keywords: Corrosion; stainless steel, salinity, electrochemical methods, laser cladding, efficiency.

1. Introduction

The flexibility and efficiency of high-energy beams such as CO_2 lasers have allowed the versatility of their application in several industrial domains [1], [3]. One of the major problems encountered in industry is the degradation of certain machine parts under the effect of corrosion, which requires their protection in order to extend their life and reduce economic costs [4], [5].

In order to ensure protection against corrosion and abrasion, nickel and cobalt alloys are widely used in industry for the coating of machine parts working at very high temperatures [6], [7]. Surface treatments carried out under high energy beams by powder injection offers the possibility to apply a broad

variety of metallurgical coatings on the surface of materials, and they can be effective and economical solutions [4].

Indeed, the importance of this type of treatment is asserting itself more and more, because it is one of the rare means easy to implement and to reduce the cost of production. With this new technology, the coatings produced can give new properties to the base materials [8].

Studies have shown the effect of the treatment on the geometric quality of the laser sheath obtained by powder injection [9], [10]. However, the effectiveness of protecting coatings against corrosion remains to be examined. Due to the interaction of stainless steel with aqueous solutions, especially during desalination (water treatment) and petrochemicals process in which the alloy is in contact with highly concentrated saline and acidic environments, corrosion problems arise [11], [12]. Research in the field of stainless steels corrosion used in chlorinated media is of great practical value. The initiation of pitting by chlorides causing rupture of the passive film occurs at a so-called pitting potential. To explore pitting of steel many investigations have been made, the theories estimate that Cl^- penetrates and migrates through passive films. Between pitting potential and Cl^- concentration a linear relationship has been reported elsewhere. Some researchers have attributed the influence of the interaction of chlorides with nitrogen and sulfur included during the bites. Others have studied the effect of pH on the corrosion of stainless steels [13].

The present paper is a study of corrosion resistance generated by deposits of nickel base and cobalt base alloys produced by powder projection under CO_2 laser beam in a NaCl medium. Coaxial injection of powder is used to localize the powder flow for production of deposits on a 304L stainless steel. Polarization and electrochemical impedance spectroscopy methods were used as an experimental tool for this research [14], [16].

2. Experimental procedure

2.1 Materials

Samples of an austenitic stainless steel as substrates are chosen. Indeed, this type of steel exhibits virtually no allotropic transformation on heating and cooling [17]. Prior to coating, the cubic shaped (1 x 1 cm^2) X3CrNi18-10 (304L) (0.03% C, 0.75% Si, 18% Cr, 68.7% Fe, 10% Ni, 1.5% Mn, 0.02% P) were cleaned with acetone and rinsed with alcohol. Before any deposition, the powders of Cenium 36 (Ce36) (36% Ni, 30% Cr, W, 1% C) and METCO 18C (M18C) (40% Co, 18% Cr, 26.8% Ni, 20.5% Fe, 0.2% C, W, 3.5% Si, Mn, 3% B, 6% Mo) undergo a drying treatment for approximately 30 minutes at 200° C. The two working electrodes are prepared from a 304L stainless steel one coated

with nickel and the other with cobalt. The models are presented by the figures below.
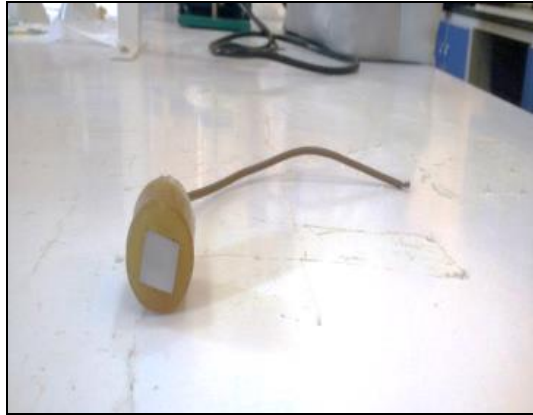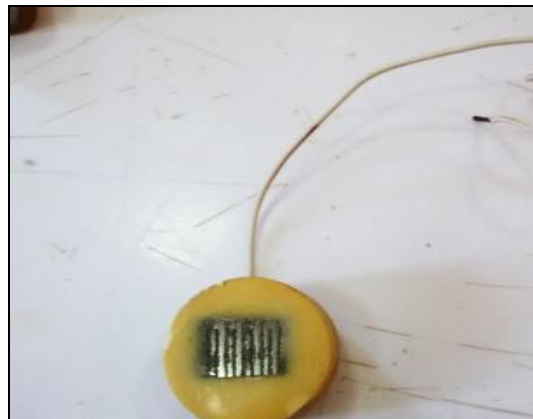

Figure 1: Working electrode 304L

Figure 2: Working electrodes 304L nickel coating

With 1200 grade emery paper the exposed area was mechanically abraded because the good quality of the surface state of the deposits made does not require the use of repeated polishing. It is then washed with distilled water, degreased with acetone and finally dried before each experiment. The corrosive medium is a 3% NaCl solution prepared by dissolving 30 g of powdered NaCl crystallized in a liter of distilled water, then stirred to obtain a homogeneous solution. Before their microstructural characterization, samples were polished and cleaned using the following reagent: 150 cm^3 HCl, 25 g K$_2$Cr$_3$O$_7$, 50 cm^3 H$_2$O Keller's reagent.

2.2 Laser claddings

The heat source used is a continuous CO_2 laser (CILAS CI 4000) whose output power from the cavity varies between 200 and 3600 W. To focus the beam on the surface of the sample, a focal lens of 191 mm is used. The manufacturing process involves injecting powder into a bath of molten metal on the surface of the workpiece under the laser beam. This moves with a constant speed with respect to the beam. The powder dispenser used is of type 4MP (METCO). A system of nozzles, arranged around the lens and the focused beam, directs the powder and the protective argon jet towards the part, in the same axis as the laser beam *(Fig. 3)*. The processing parameters have been previously optimized: energy density (95.103 W / cm^2); travel speed (5 mm / s); powder flow rate (20g / min); workpiece nozzle distance (20 mm); powder / beam tilt (15 degrees), *Fig. 3.*
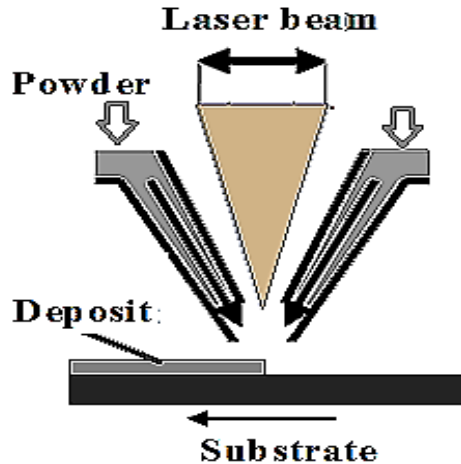
Figure 3: Powder spray coating process

2.3 Electrochemical measurement setup

The experimental setup is an electrochemical cell composed of conventional three electrodes which are: the working electrode made up of the steel to be tested with an (1 x 1 cm^2) exposed area to the corrosive solution. The reference electrode (calomel) and the auxiliary electrode consisting of a platinum plate (1 x 1 cm^2). A Volta lab PGZ 301 potentiostate controlled by Tacussel model corrosion analysis software (Voltamaster 4 and EC-lab demo) was used for electrochemical measurements. In Nyquist representation the EIS data were given.

3. Results and discussion

3.1 Laser claddings microstructure

The microstructure of the deposit M18 cobalt-based powder / 304L obtained by SEM is presented in *Fig. 4*. The structure is mixed type, the balance is cellular or dendritic, oriented randomly. The existence of various growth regimes therefore leads to very distinct structures with different properties, which is confirmed by other studies [18]. The 1.2 mm thick sheathed layer obtained has a good morphological appearance with a low dilution rate.
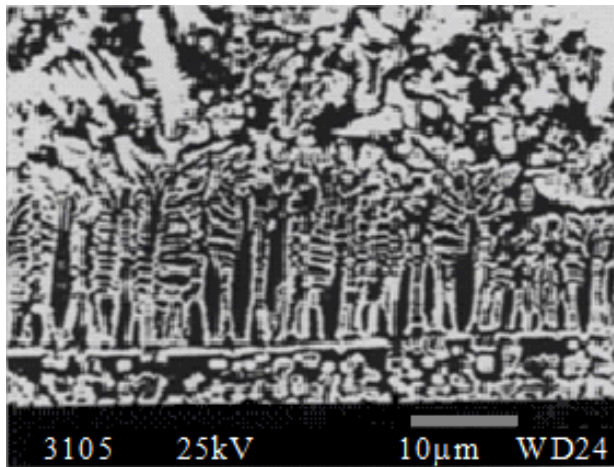
Figure 4: Microstructure at the coating-substrate (Metco18) / 304L

Several areas can be distinguished. A slightly marked transition zone with the substrate is associated with an interface probably characterized by solidification with a flat front. It is a monocrystalline and homogeneous growth layer. An area adjacent to the interface in which an austenitic primary phase develops.

3.2 Microhardness profile

A Vickers's microhardness tester was used. The microhardness measurements under a load of 200 g (*Fig. 5*) were taken along a cross section of the deposit. The fluctuations recorded at the level of hardness correspond to the various zones described by the morphologies presented in *Fig. 4*. The hardness filiation carried out highlights the existence of different mechanical properties between the various parts of the deposit and the support. Indeed, from the point

of view of hardness, an appreciable gain was recorded due to the change brought about by this surface treatment.

The results of the literature confirmed that during processing, precipitates of complex borides and carbides of the M7C3 type form, which strengthen the matrix and therefore give it new properties such as good resistance to friction [19-21].
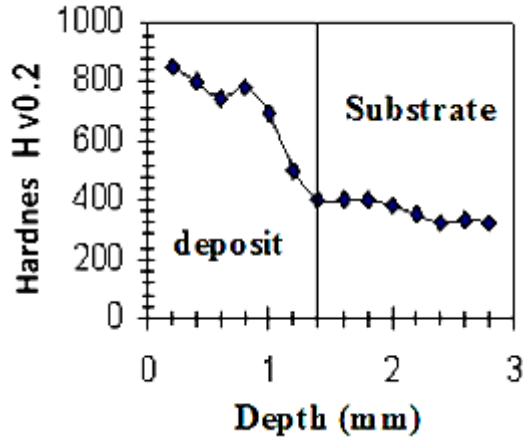
Figure 5: Microhardness profile along the deposit

3.3 Polarization curves

The potentiodynamic polarization curves for stainless steel in the 3% NaCl medium in the absence and presence of nickel-based and cobalt based coating are shown in *Fig 6, Fig 7*. It can be seen that anodic and cathodic reactions of stainless steel with the saline environment are inhibited in the presence of protective deposits which reduces the dissolution of stainless steel by delaying the degradation reaction. In presence of this coating the corrosion potential is moved to the more noble value (positive) playing the role of anodic corrosion inhibitor. Obtained by extrapolation of the Tafel lines, the electrochemical corrosion parameters as a corrosion potential (E_{corr}), corrosion current density (i_{corr}), cathodic and anodic Tafel slopes (β_c, β_b) are grouped in *Table 1*. The efficiency of inhibition ($E\%$) is determined from the following relation:

$$E\% = \frac{1 - i_{corr}}{i_{corr}^0} \cdot 100 . \tag{1}$$
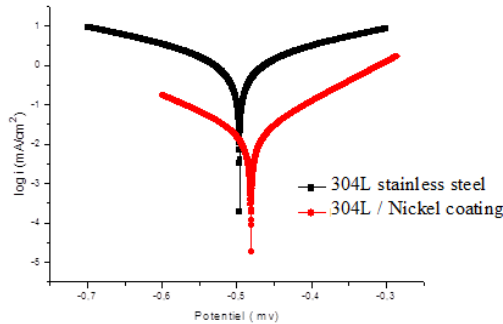
Figure 6: Polarization curves of 304L steel in 3% NaCl in absence and presence of nickel coating
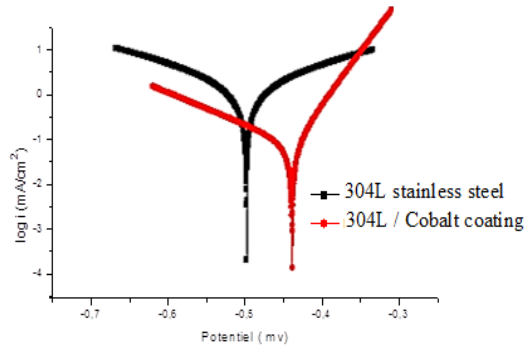
Figure 7: Polarization curves of 304L steel in 3% NaCl in absence and presence of cobalt coating

In the presence of coatings, the corrosion density (i_{corr}) expressed in mA·cm^2, directly proportional to the corrosion rate, decreases, which probably inhibits corrosion and remarkably for nickel compared to results *Table 2* [22] from the literature, which prove the effectiveness of the laser process used. The current density and corrosion polarization resistance of 304L steel in 3% NaCl are 0.2993 (mA / cm^2) and 57.69 (Ω·cm^2), respectively. These values change by the application of the nickel and cobalt based metallic coating ((304L / Ni coating.) (304L / Co coating), therefore leading to a decrease in i_{corr} and an increase in R_p, which confirms the high value of efficiency presented in *Table 1*, the effective protective barrier role of the applied coating.

Table 1: Potentiodynamic polarization parameters for stainless steel in 3% NaCl in absence and presence of Ni and Co coating at 298 K

	E (i=0) (mV)	R_p ($\Omega \cdot cm^2$)	i_{corr} (mA/cm^2)	β_a (mV)	β_c (mV)	*Coeff.*	E (%)	Corrosion rate Cr (μm/year)
304L	-488.8	57.69	0.364	78.8	-125.3	1	-	3.96
304L/ Ni coating	-486.3	647.10	0.026	72.5	-89.7	0.9993	98.12	0.25
304L/ Co coating	-481.1	149.28	0.084	52.2	-64.8	0.9953	83.22	0.96

Table 2: Corrosion rate of 304L stainless steel specimens, coated in a chlorinated nickel bath [22]

Concentration Al$_2$O$_2$ (g/l)	Corrosion rate (μm/year)	Current density (μA/cm^2)	E_{Corr}/E_{CS} (mV)
Uncoated	4.635	0.3963	-354.7
0	3.006	0.3743	-363.3
5	1.284	0.1098	-356.5
10	1.656	0.1415	-361.5
15	2.651	0.2267	-336.3
20	1.961	0.1638	-364.7

3.4 Electrochemical impedance spectroscopy measurements

Schematized by *Fig.8* and *Fig.9*, the diagrams of impedance in Nyquist representation traces in the absence and presence of metallic coatings reduce to unreformed capacitive semicircles indicating that corrosion process has been controlled by a single phenomenon which is the transfer of charge.
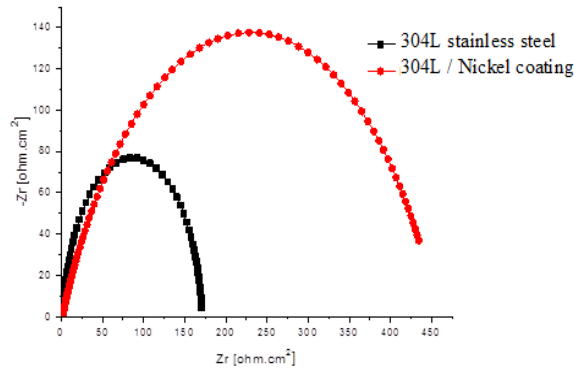
Figure 8: Nyquist diagrams of 304L stainless steel in 3% NaCl medium in the absence and presence of the nickel-based coating
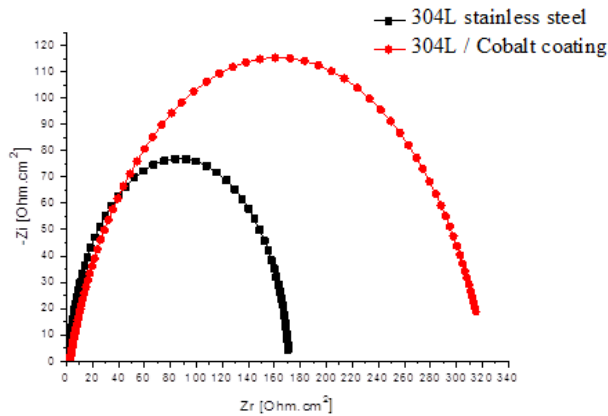
Figure 9: Nyquist diagrams of 304L stainless steel in 3% NaCl medium in the absence and presence of the cobalt-based coating

The simulated curves essentially follow the experimental data. *Table 3* presents the values of solution resistance (R_s), load transfer resistance (R_{tc}), total capacitance (C_{dl}), which were calculated by simulating the experimental data with the EC-Lab software.

It is noted that the diameter of the semicircles is proportional to the transfer resistance which is higher in the presence of deposits and remarkably for nickel. The undeformed regular shape indicates a homogeneous and complete distribution of the protective film on the substrate surface which is confirmed by the results obtained and carried on the *Table 2*, showing that there is an

increase in the transfer resistance R_{tc} load with coating application as capacitance values decrease.

Table 3: Values associated with the impedance parameters stainless steel in 3% NaCl in absence and presence of Ni and Co coating at 298 K

	R_S (Ω·cm^2)	R_{tc} (Ω·cm^2)	C_{dl} (μF/cm^2)	E (%)
304L	16.20	150.2	0.4827 10^{-3}	-
304L/ Ni coating	8.82	2008.0	0.4002 10^{-3}	91.82
304L/ Co coating	9.24	1840	0.4055 10^{-3}	83.22

4. Conclusion

From the electrochemical study for the characterization of the corrosion behavior in saline environment of coatings made under laser beam we conclude that:

With an efficiency of E = 98.12 % and a distribution homogeneity according to the results obtained from the study using the methods of polarization and electrochemical impedance spectroscopy the coatings carried out under high beam can constitute a solution for the fight against corrosion in the case of parts working in saline environments and can act effectively as a corrosion inhibitor for steels.

The difference between the efficiency values obtained for the two cases of coating nickel base, cobalt base respectively (E (%) 98.12; 83.22) brings us back to reflect on the influence of the quality of the powders used as filler material.

The very low corrosion rate obtained in the case of laser coatings shows that this method offers better protection against corrosion.

The laser process according to the impedance curves ensures continuity and uniformity of the protective layers deposited.

Acknowledgements

References

[1]   Pelletier, J. M., Sahour, M. C., Pilloz, M., and Vannes, A. B., "Influence of processing conditions on geometrical features of laser claddings obtained by powder injection", *Journal of Materials Science*, vol. 28, pp. 5184-5188, 1993.

[2]   Sallamand, P., "Surface alloy and coatings produced under a laser beam by spraying powder on an aluminum-based substrate: microstructural, mechanical and tribological characterization", Thesis, INSA Lyon, 1994.

[3]   Sexton, C. L., Byrne, G., and Walkins, K.G., "Alloy development by laser cladding: an overview", *Journal of Laser Applications*, vol. 13, 2-11, 2001.

[4]   Hidouci, A., Pelletier, J. M., Ducoin, F., Dezert, D., El Guerjouma, R., "Microstructural and mechanical characteristics of laser coatings", *Surface and Coatings Technology*, vol. 123, pp. 17-23, 2000.

[5]   Pei, Y. T., Ouyang, J. H., and Lei, T.C., "Microstructure of bonding zones in laser-clad Ni-alloy-based composite coatings reinforced with various ceramic powders", *Surf. Metall. Mater. Trans*, vol. 27A2, pp. 391-400, 1996.

[6]   Sexton, C. L., Byrne, G., and Walkins, K. G., "Alloy development by laser cladding: An overview", *Journal of Laser Applications*, vol. 13, pp. 2-11, 2001.

[7]   Safonov, A. N., and Aleksenko, S., "Effect of laser treatment on the wear resistance of steels", *Metal Science and Heat treatment*, vol. 40, pp. 399-401, 1998.

[8]   Ajao, J., and Hamar-Thibault, S., "Influence of additions on the solidification behaviour of Ni-B alloys- crystallography of Ni-Ni3B eutectic", *Journal of Materials Science*, 1988.

[9]   De Oliveira, U., Ocelik, V., and De Hosson, J. T. M., "Analysis of coaxial laser cladding processing conditions JTM", Surface & Coatings Technology: 197.2-3, 127-136 10. vol. 23, pp. 1112–1125, 2005.

[10]   Boussaha, E. H., and Al., "Study of powder particle size effect on microstructural and geometrical features of laser claddings using response surface methodology RSM", *Electrical and Mechanical Engineering, Acta Universitatis Sapientiae*, vol. 11, pp. 99-116, 2019.

[11]   Da Rocha, J., Gomes, J., D'Elia, E., "Aqueous Extracts of Mango and Orange Peel as Green Inhibitors for Carbon Steel in Hydrochloric Acid Solution", Mater Research, 17:1581-1587. https://doi.org/10.1590/1516-1439.285014, 2014.

[12]   Aounitia, A., Elmsellema, H., Tighadouinia, S., and Al. "Schiff's base derived from 2-acetyl thiophene as corrosion inhibitor of steel in acidic medium", https://doi.org/10.1016/j.jtusci.11.008, 2015.

[13]   Scully, J. C., "Corrosion Protection, Fundamental principles", Editor: Masson, Materials Science Collection, 208p., Released July 1995.

[14]   Monsempès. T., "Corrosion of steel by oils containing naphthenic acids: search for a method to measure the instantaneous rate of corrosion", Materials Doctoral School of Lyon, Doctoral thesis, France, 2000.

[15]   Ntienoue, J., "Study, characterization and electrochemical monitoring of the surface of 254 SMO stainless steel in natural Amazonian aqueous media", Doctoral thesis, University of the Antilles and Guyana, 2013.

[16]   Gabrielli, C., "Electrochemical methods Impedance measurements", Edition, Techniques of Engineering, Paris, France, 1994.

[17]   Pergue, D., "Application of power lasers. Obtaining out of equilibrium states by surface reflections of metal surfaces", Thesis, INPG, Grenoble, 1987.

[18]   Laribi, M., Mesrati, N., Laracine, M., Vannes, A. B., Thereux, D., "Experimental determination of residual stresses within structures developed by thermal spraying", *Materials & Techniques*, N°9-10, pp. 15-21, 2001.

[19] De Mello, J. D. B., et al., "Abrasion mechanisms of white cast iron I : Influence of the metallurgical structure of molybdenum white cast irons", *Materials Sciences and Engineering*, Vol. 73, pp. 203-213, 1985.

[20] Olson, D., "Prediction of austenitic weld metal microstructure and properties", *Materials Science*, pp. 281-295, 1985.

[21] Pacquentin, W., "Contribution to the study of the physico-chemical properties of surfaces modified by laser treatment. Application to improving the resistance to localized corrosion of stainless steels", *Materials*, University of Bourgogne, pp. 64-84, 2011.

[22] Anoune, I., "Corrosion resistance of nickel-alumina composite coatings on different substrates", Thesis, University of Batna, pp. 55-64, 2014.

Acta Universitatis Sapientiae

Acta Universitatis Sapientiae
Electrical and Mechanical Engineering

Sapientia University

Scientia Publishing House

Information for authors

Acta Universitatis Sapientiae, Electrical and Mechanical Engineering publishes only original papers and surveys in various fields of Electrical and Mechanical Engineering. All papers are peer-reviewed.

Papers published in current and previous volumes can be found in Portable Document Format (PDF) form at the address: `http://www.acta.sapientia.ro`.

The submitted papers must not be considered to be published by other journals. The corresponding author is responsible to obtain the permission for publication of co-authors and of the authorities of institutes, if needed. The Editorial Board is disclaiming any responsibility.

The paper must be submitted both in MSWord document and PDF format. The submitted PDF document is used as reference. The camera-ready journal is prepared in PDF format by the editors. In order to reduce subsequent changes of aspect to minimum, an accurate formatting is required. The paper should be prepared on A4 paper (210 × 297 mm) and it must contain an abstract of 200-250 words.

The language of the journal is English. The paper must be prepared in single-column format, not exceeding 12 pages including figures, tables and references.

The template file from http://www.acta.sapientia.ro/acta-emeng/emeng-main.htm may be used for details.

Submission must be made only by e-mail (`acta-emeng@acta.sapientia.ro`).

One issue is offered to each author free of charge. No reprints are available.